Fast Numerical Algorithms for 3-D Scattering from PEC and Dielectric Random Rough Surfaces in Microwave Remote Sensing

by

Lisha Zhang

A Dissertation Presented in Partial Fulfillment
of the Requirements for the Degree
Doctor of Philosophy

Approved April 2016 by the
Graduate Supervisory Committee:

George Pan, Chair
Rodolfo Diaz
James Aberle
Hongbin Yu

ARIZONA STATE UNIVERSITY

May 2016

ABSTRACT

We present fast and robust numerical algorithms for 3-D scattering from perfectly electrical conducting (PEC) and dielectric random rough surfaces in microwave remote sensing. The Coifman wavelets or Coiflets are employed to implement Galerkin's procedure in the method of moments (MoM). Due to the high-precision one-point quadrature, the Coiflets yield fast evaluations of the most off-diagonal entries, reducing the matrix fill effort from $O(N^2)$ to $O(N)$. The orthogonality and Riesz basis of the Coiflets generate well conditioned impedance matrix, with rapid convergence for the conjugate gradient solver. The resulting impedance matrix is further sparsified by the matrix-formed standard fast wavelet transform (SFWT). By properly selecting multiresolution levels of the total transformation matrix, the solution precision can be enhanced while matrix sparsity and memory consumption have not been noticeably sacrificed. The unified fast scattering algorithm for dielectric random rough surfaces can asymptotically reduce to the PEC case when the loss tangent grows extremely large. Numerical results demonstrate that the reduced PEC model does not suffer from ill-posed problems. Compared with previous publications and laboratory measurements, good agreement is observed.

To My Parents Cunxiu Zhang and Xiufang Guo

ACKNOWLEDGMENTS

I would like to express my gratitude to my advisor and committee chair, Prof. George Pan, without whom my research and this dissertation would not have been possible. Dr. Pan gave me this opportunity to come to ASU to pursuit my Ph.D. in EE department. I am very grateful for his advising, encouragement, inspiration, and enduring patience.

I would like to give special appreciation to Prof. James Aberle, Prof. Rodolfo Diaz, Prof. Hongbin Yu and Prof. Hongyu Yu for serving as my committee members. I benefit a lot from courses by Dr. Aberle and Dr. Hongyu Yu. And I also gain from joining the summer meeting in Dr. Diaz's group. Dr. Hongbin Yu has also given me very valuable suggestions on my dissertation.

I would also like to thank Dr. Abbas Abbaspour-Tamijani for his guidance in the Intel project and microwave course and Prof. Constantine Balanis for electromagnetic courses. And I appreciate Dr. Ming Jin, Dr. Le Wang, Dr. Ke Wang, Dr. Jiruo Ye, Dr. Zhenyu Huang, Dr. Zhonghai Guo, for their help and support.

TABLE OF CONTENTS

Page

LIST OF TABLES . . . vi

LIST OF FIGURES . . . vii

CHAPTER

1 INTRODUCTION . . . 1

2 COIFMAN WAVELETS . . . 5

2.1 Basic Principles . . . 5

2.1.1 Scalets and Wavelets . . . 5

2.1.2 Orthogonal Properties . . . 7

2.2 Coifman Wavelets . . . 8

3 FAST COIFLET MFIE FOR SCATTERING FROM OPEN ROUGH SURFACES . . . 13

3.1 Formulation . . . 16

3.1.1 Coiflets based Scalar MFIE . . . 16

3.1.2 Matrix Sparsification Using SFWT . . . 23

3.1.3 SFWT Implementation with Matrix Form . . . 26

3.2 Computational Complexity . . . 31

3.2.1 Circular Cylinder . . . 31

3.2.2 Sphere . . . 31

3.3 Accuracy . . . 36

3.3.1 Circular Cylinder . . . 38

3.3.2 Sphere . . . 38

3.3.3 Almond . . . 41

3.3.4 Ogive . . . 48

3.4 Random Rough Surfaces . . . 48

3.4.1 Surface with Intermediate Roughness 51
3.4.2 Very Rough Surface 51
4 ON UNIFIED NUMERICAL ALGORITHM FOR 3-D SCATTERING FROM PEC AND DIELECTRIC RANDOM ROUGH SURFACES 53
4.1 Formulation 55
4.1.1 Vector and Scalar Integral Equations 55
4.2 Expansion and Test with Coifman Scalets 57
4.3 Scattering 62
4.4 Incident Power 63
4.5 Numerical Results 67
4.5.1 Validations 68
4.5.2 Examples 74
5 CONCLUSION 85
REFERENCES 86

APPENDIX

A ITERATIVE SOLUTION OF TAPERED INCIDENT POWER 91
B GENERATION OF RANDOM SURFACES BY SPECTRAL DOMAIN METHOD 95

LIST OF TABLES

Table Page

2.1 Moment Integrals for Coifman Scalets of Order $L = 4$ 10

3.1 RMS Errors for Elements of $U = S^t S$ in 1-D SFWT ($j_h = 6$) 30

3.2 Fixed Frequency 33

3.3 Fixed Discretization 35

3.4 Fixed Discretization: Non-Zero Entry Memory 36

4.1 Incident Power of the Tapered Wave ($\tau = 2.4\lambda$) 68

4.2 Parameter Comparisons between PEC Code (MFIE) and Dielectric Code (Our Normalized Surface IE) 69

A.1 Incident power of the tapered wave ($\tau = 2.4\lambda$) 93

LIST OF FIGURES

Figure Page

2.1 Coifman Scalet and Wavelet of $L = 4$ and $j_0 = 0$. 8

2.2 A Perfectly Conducting Circular Cylinder with a Plane Wave Incident (300MHz, TE Case). The Cylinder Is Assumed to Be Infinity along Z-Axis, Which Is Perpendicular to the Cross Section of the Cylinder. . . 10

2.3 The Excited Current Density Comparisons among Pulse, Coiflet and Analytical Methods, for the Problem of a Conducting Circular Cylinder Illuminated by a Plane Wave (TE Case). The Normalized Current Magnitude and the Relative Error to the Analytical Solutions Are Included. The 64 Sampling Points Are for Both Pulse Case and Coiflet Case. 11

2.4 The Scattered Field Pattern Comparisons among Pulse, Coiflet and Analytical Methods, for the Problem of a Conducting Circular Cylinder Illuminated by a Plane Wave (TE Case). The Normalized RCS and the Relative Error to the Analytical Solutions Are Included. The 64 Sampling Points Are for Both Pulse Case and Coiflet Case. 12

3.1 Nonstandard Form Representation of a Decomposed Matrix. 24

3.2 Standard Form Representation of a Decomposed Matrix. 25

3.3 Impedance Matrix of the Standard FWT (Threshold $= 1 \times 10^{-3}$) for a PEC Circular Cylinder Illuminated by a Plane Wave (300MHz, TE Case). The Cylinder Length Is Infinity and There Are 1024 Sampling Points along the Entire Circle. 26

3.4 The Orthogonality Comparison between $j_l = 0$ and $j_l = 3$ for 1-D Total Transformation Matrix S. Diagonal and Off-Diagonal Elements of $U = S^t S$ Are Compared Separately. The Finest Level $j_h = 6$. 29

Figure Page

3.5 Transformation Matrix on j-th Level in 2-D SFWT. 30

3.6 Memory Scaling of MFIE after SFWT (Threshold = 1×10^{-3}) for a PEC Circular Cylinder with Infinity Length. The Plane Wave Is Employed as the Incident (TE Case). Two Experiments Are Performed: (1) Fixed Discretization and Increasing Frequency; (2) Fixed Frequency and Decreasing Discretization. 33

3.7 Complexity of MFIE with SFWT for a PEC Sphere: (a) Matrix Filling Time with MFIE, (b) Memory of Non-Zero Entries in SFWT Matrix (Threshold = 1×10^{-3}). Two Experiments Are Performed: (1) Fixed Discretization and Increasing Frequency; (2) Fixed Frequency and Decreasing Discretization. 34

3.8 Memory Scaling of MFIE after SFWT (Threshold = 1×10^{-3}) in a PEC Sphere Scattering Problem for the Fixed Discretization Case with the Increasing Frequency. 37

3.9 Relative Errors with Respect to FEKO Data for the Bistatic Scattering from a PEC Sphere at 600MHz ($\phi = 0°$ Cut). The Coarsest Levels of $j_l = 0$ and $j_l = 3$ Are Compared in Creating SFWT Transformation Matrix. The x-Axis Denotes the Indices of Sorted Observation Angles in θ. 37

3.10 The Normalized Surface Current Density and the Normalized Scattering Coefficients for the Problem of a PEC Circular Cylinder Illuminated by a Plane Wave (300MHz, TE Case). There Are 64 Sampling Points along the Entire Circle. Simulation Results of SFWT, Standard Coiflets and Analytical Method Are Compared. 39

3.11 The Normalized Surface Current Density and the Normalized Scattering Coefficients for the Problem of a PEC Circular Cylinder Illuminated by a Plane Wave (300MHz, TE Case). There Are 1024 Sampling Points along the Entire Circle. Simulation Results of SFWT, Standard Coiflets and Analytical Method Are Compared. 40
3.12 Sphere Configuration 41
3.13 Impedance Matrix of SFWT (Threshold = 1×10^{-3}) for a PEC Sphere at 600MHz. 42
3.14 Bistatic Scattering of a PEC Sphere at 600MHz ($\phi = 0°$ Cut). The Incident Plane Wave Is into the North Pole with the E-Field Parallel to x-Axis. Simulation Results of SFWT (Threshold = 1×10^{-3}), Standard Coiflets Method and FEKO Are Compared. 42
3.15 Impedance Matrix of SFWT (Threshold = 1×10^{-3}) for a PEC Sphere at 300MHz. 43
3.16 Bistatic Scattering of a PEC Sphere at 300MHz ($\phi = 0°$ Cut). The Incident Plane Wave Is into the North Pole with the E-Field Parallel to x-Axis. Simulation Results of SFWT (Threshold = 1×10^{-3}), Standard Coiflets and FEKO Are Compared. 43
3.17 Almond Configuration 44
3.18 Monostatic Scattering from the NASA Almond at 1.19GHz. Simulation Results of SFWT, Standard Coiflets and FEKO Are Compared. ... 45
3.19 Monostatic Scattering from the NASA Almond at 7GHz. Simulation Results of SFWT, Standard Coiflets and FEKO Are Compared. 46

3.20 Monostatic Scattering from the NASA Almond at 7GHz. Simulation Results with Similar Dense Sampling Points Are Compared among SFWT, Standard Coiflets and FEKO. Measured Data in Literature Is Also Provided. 47

3.21 Ogive Configuration 47

3.22 Monostatic Scattering from the Metallic Ogive at 1.18GHz. Simulation Results of SFWT, Standard Coiflets and FEKO Are Compared. 49

3.23 Configuration of 3-D Scattering from an Example Rough Surface Profile. 50

3.24 Bistatic Scattering Coefficients from One Realization of the $8\lambda \times 8\lambda$ PEC Rough Surface ($\sigma = 0.2\lambda, l_x = l_y = 0.6\lambda$). The Incident Tapered Wave Is at $\theta_i = -40°$ and $\phi_i = 90°$ (Horizontal Polarization). Simulation Results of SFWT and Standard Coiflets Method Are Compared. . . 50

3.25 Bistatic Scattering Coefficients from One Realization of the $16\lambda \times 16\lambda$ PEC Rough Surface ($\sigma = 1.0\lambda, l_x = l_y = 2.0\lambda$). The Incident Tapered Wave Is at $\theta_i = -20°$ and $\phi_i = 90°$ (Horizontal Polarization). Simulation Results of SFWT and Standard Coiflets Method Are Compared. . . 52

3.26 Average Bistatic Co-Polarized and Cross-Polarized RCS from 576 Realizations of the $16\lambda\times16\lambda$ PEC Rough Surface ($\sigma = 1.0\lambda, l_x = l_y = 2.0\lambda$). The Incident Tapered Wave Is at $\theta_i = -20°$ and $\phi_i = 90°$ (Horizontal Polarization). 52

4.1 Configuration of 3-D Scattering from Random Rough Surface (Horizontal Incident Case). 56

4.2 Incident Field ${H_y}^i$ of the Tapered Wave ($\tau = 2.0\lambda$) at: (a) $\theta_i = 0°, \phi_i = 90°$; (b) $\theta_i = -40°, \phi_i = 90°$; (c) $\theta_i = -60°, \phi_i = 90°$. 65

Figure Page

4.3 Sparsity Pattern of the Matrix for a Single $8\lambda \times 8\lambda$ Dielectric Surface ($h = 0.2\lambda, l_x = l_y = 1.0\lambda, \varepsilon_{r2} = 1 - 20000j$). Blue color represents nonzeros while white color represents zeros. 70

4.4 The Magnitude of Surface Currents and Field Normal Components at the Cross Section of $y = 6.25\lambda$ for a Single $8\lambda \times 8\lambda$ Dielectric Surface ($h = 0.2\lambda, l_x = l_y = 1.0\lambda, \varepsilon_{r2} = 1 - 20000j$), Compared to PEC Case. (Horizontal Incidence with $\theta_i = -40°$ and $\phi_i = 90°$) 71

4.5 Bistatic RCS of a Single $8\lambda \times 8\lambda$ Dielectric Surface ($h = 0.2\lambda, l_x = l_y = 1.0\lambda, \varepsilon_{r2} = 1 - 20000j$), Compared to PEC Case. Both Coherent and Incoherent Components Are Included in the Comparison Above. (Horizontal Incidence with $\theta_i = -40°$ and $\phi_i = 90°$) 72

4.6 Bistatic RCS of a Single $16\lambda \times 16\lambda$ Dielectric Surface ($h = 0.2\lambda, l_x = l_y = 1.0\lambda, \varepsilon_{r2} = 1 - 20000j$), Compared to PEC Case. Both Coherent and Incoherent Components Are Included in the Comparison Above. (Horizontal Incidence with $\theta_i = -40°$ and $\phi_i = 90°$) 72

4.7 Average Bistatic RCS Comparisons between Horizontal Incidence and Vertical Incidence, Resulting from 20 Realizations of $8\lambda \times 8\lambda$ Random Gaussian Surfaces ($h = 0.2\lambda, l_x = l_y = 1.0\lambda, \varepsilon_{r2} = 6.5 - 1.0j$). Both Coherent and Incoherent Components Are Included ($\theta_i = -20°$ and $\phi_i = 90°$). 73

4.8 Average Bistatic RCS Comparisons between Horizontal Incidence and Vertical Incidence, Resulting from 40 Realizations of $16\lambda\times16\lambda$ Random Gaussian Surfaces ($h = 0.2\lambda, l_x = l_y = 1.0\lambda, \varepsilon_{r2} = 6.5 - 1.0j$). Both Coherent and Incoherent Components Are Included ($\theta_i = -20^\circ$ and $\phi_i = 90^\circ$). 73

4.9 Average Backscattering RCS Comparisons among Methods of Coiflet, PT, KA and First Order Wiener-Hermite, for 20 Realizations of $8\lambda\times8\lambda$ Conducting Gaussian Surfaces ($\varepsilon_{r2} = 1 - 2000j$): (a) $kh = 0.1$ and $kl = 3.0$; (b) $kh = 0.66$ and $kl = 7.0$. Only the Incoherent Components of Co-Polarization Are Considered. 75

4.10 Average Backscattering RCS Comparisons among Methods of Coiflet, PT, KA and First Order Wiener-Hermite, for 20 Realizations of $8\lambda\times8\lambda$ Dielectric Gaussian Surfaces ($\varepsilon_{r2} = 20 - 20j$): (a) $kh = 0.1$ and $kl = 3.0$; (b) $kh = 0.66$ and $kl = 7.0$. Only the Incoherent Components of Co-Polarization Are Considered. 76

4.11 Average Backscattering RCS Comparisons among Methods of Coiflet, PT, KA and First Order Wiener-Hermite, for 20 Realizations of $16\lambda\times16\lambda$ Conducting Gaussian Surfaces ($\varepsilon_{r2} = 1-2000j$): (a) $kh = 0.1$ and $kl = 3.0$; (b) $kh = 0.66$ and $kl = 7.0$. Only the Incoherent Components of Co-Polarization Are Considered. 77

4.12 Average Backscattering RCS Comparisons among Methods of Coiflet, PT, KA and First Order Wiener-Hermite, for 20 Realizations of $16\lambda \times 16\lambda$ Dielectric Gaussian Surfaces ($\varepsilon_{r2} = 20 - 20j$): (a) $kh = 0.1$ and $kl = 3.0$; (b) $kh = 0.66$ and $kl = 7.0$. Only the Incoherent Components of Co-Polarization Are Considered. 78

4.13 The Magnitude of Surface Currents and Field Normal Components for a Single $8\lambda \times 8\lambda$ Gaussian Surface ($h = 0.2\lambda, l_x = l_y = 0.6\lambda, \varepsilon_{r2} = 6.5 - 1.0j$) : (a) J_x; (b) J_y; (c) M_x; (d) M_y; (e) H_n; (f) E_n. (Horizontal Incidence with $\theta_i = -10^\circ$ and $\phi_i = 90^\circ$) 80

4.14 The Bistatic RCS from a Single $8\lambda \times 8\lambda$ Surface Realization with $h = 0.2\lambda$, $l_x = l_y = 0.6\lambda$ and $\varepsilon_{r2} = 6.5 - 1.0j$ (Horizontal Incidence with $\theta_i = -10^\circ$ and $\phi_i = 90^\circ$). 81

4.15 Average Bistatic Co-Polarized RCS Compared with SMCG Method over 300 Realizations of $8\lambda \times 8\lambda$ Random Gaussian Surfaces ($h = 0.2\lambda$, $l_x = l_y = 0.6\lambda$, $\varepsilon_{r2} = 6.5 - 1.0j$). Both Coherent and Incoherent Components Are Included. 81

4.16 Average Bistatic Co-Polarized and Cross-Polarized RCS with Coherent and Incoherent Components Respectively ($8\lambda \times 8\lambda$ Surfaces). 82

4.17 Average Bistatic Co-Polarized RCS Compared with SMCG Method over 300 Realizations of $16\lambda \times 16\lambda$ Random Gaussian Surfaces ($h = 0.2\lambda$, $l_x = l_y = 0.6\lambda$, $\varepsilon_{r2} = 6.5 - 1.0j$). Both Coherent and Incoherent Components Are Included. 82

4.18 Average Bistatic Co-Polarized and Cross-Polarized RCS with Coherent and Incoherent Components Respectively ($16\lambda \times 16\lambda$). 83

4.19 Average Bistatic Co-Polarized and Cross-Polarized RCS Compared with Experiment over 300 Realizations of $16\lambda \times 16\lambda$ Random Gaussian Surfaces ($h = 1\lambda$, $l_x = l_y = 2\lambda$, $\varepsilon_{r2} = 7 - 13j$). 83

Chapter 1

INTRODUCTION

Electromagnetic scattering problems from random rough surfaces have drawn great attentions due to the broad applications in microwave remote sensing. Both analytical and numerical methods have been extensively established in a couple of decades.

Two classical analytical methods, Kirchhoff approximation (KA) and small perturbation method (SPM), are commonly used with certain restrictions in their domains of validity. Specifically, KA requires the tangent plane approximation in the local region, which means a large radius of curvature relative to the incident wavelength is a must at each point on the surface. In SPM, the surface variations are assumed to be much smaller than the incident wavelength and the slopes of the rough surface are relatively small (Kong, 1986).

Compared to analytical methods, numerical methods on random rough surface scattering have higher flexibility in checking model accuracy and providing valuable predictions. And Monte Carlo simulations have been generally involved to produce the converged average scattering coefficient from up to several hundreds of realizations, depending on the accuracy and the efficiency of the numerical solution. The most popular numerical method is the method of moments (MoM) employed to the surface integral equations. There are two basic integral equation formulations, namely, electric field integral equation (EFIE) and magnetic field integral equation (MFIE) (Yl-Oijala *et al.*, 2012). Contrary to the EFIE, the MFIE is well-posed and renders good condition numbers of the corresponding impedance matrix, since the K operator is compact and all the eigenvalues are clustered around a non-zero value. As a result, the iterative solvers converge rapidly under the MFIE formulation (Chew *et al.*, 2008). Despite the advantages of the MFIE, in engineering RCS societies the EFIE has been dominant while MFIE is recognized as very inaccurate in handling geometrical singularity. The inaccuracy and slow convergence of the MFIE-RWG were reported in (Gurel and Ergul, 2005; Ubeda and Rius, 2006, 2005; Warnick and Peterson, 2007). A novel mixed discretization scheme for the MFIE has been recently proved a possible solution to the above problems Cools *et al.* (2011).

Maxwell's equations and the surface boundary conditions can be reduced to a single equivalent surface integral equation when the surface is a perfect conductor, while in the case of a dielectric interface the coupled pair of surface integral equations need to be employed (Warnick and Chew, 2001). In the later case, the normal components of Maxwell's equations on the surface, as the original unknowns, yield relationships with the surface derivatives of the surface currents and thus can be replaced. Though the number of unknowns is reduced, the price has to be paid for involving the surface derivatives of the surface currents in the integrand. However, rough surface scattering problems are electrically large, and thus the discretization of the corresponding surface integral equations can result in a large dense matrix whose filling time dominants the computational cost. Specifically, traditional MoM requires the computation time of $O(N^2)$ for matrix fill and $O(N^3)$ for matrix inversion, where N is the total number of unknowns. Accordingly, fast algorithms have been developed to solve this issue and boost the computation efficiency through e.g. manipulating impedance matrix, accelerating matrix solving procedure, compressing the number of unknowns, and so on. Several methods have been listed in this literature. Based on the AIM (Bleszynski *et al.*, 1993, 1996), the sparse matrix/canonical grid (SM/CG) method (Pak *et al.*, 1997) has employed the planar RWG basis with the series Taylor expansion and accelerated matrix-vector multiplications with fast Fourier transforms

(FFT) in the iterative solver. And to further cut down the number of unknowns and efficiently increase the flexibility, the curvilinear RWG basis and the Chebyshev interpolating Green's function have been applied instead (Huang *et al.*, 2009; Huang and Tsang, 2012). The forward-backward (FB) method (Holliday *et al.*, 1996; Iodice, 2002) has been employed for 1-D surfaces with a modified fast multipole method (FMM) (Torrungrueng *et al.*, 1998) or spectral acceleration (SA) (Liu *et al.*, 2011; Brennan *et al.*, 2013).

Wavelets have been successfully used to efficiently solve integral equations related to 3-D scattering and emissivity problems (Pan *et al.*, 2014; Wang and Pan, 2013; Jin *et al.*, 2016). Particularly, wavelets has been applied together with the iterative technique, e.g. bi-conjugate gradient stabilized method (Bi-CGSTAB) (Vorst, 1992; Huang *et al.*, 2014) for random rough surface (Tretiakov *et al.*, 2004; Pan *et al.*, 2004). Tapered waves (Braunisch *et al.*, 2000) are used in rough surface scattering to truncate the computational domain. In (Pan *et al.*, 2004), the tapered wave was imposed as the incident beam to emulate certain problems in which the footprint of the beam is smaller than the target, preventing the edge diffraction. Owing to concentrated energy in spatial/spectral domain and vanishing moments, the implementation of wavelets as the basis and testing functions produces a sparse impedance matrix and exhibits fast convergence. Further, the Dirac-δ like property of Coiflets (Pan, 2003) permits fast calculation of the most off-diagonal entries in the impedance matrix, imposing the one-point quadrature formula and dramatically reducing the computational efforts in filling matrix from $O(N^2)$ to $O(N)$.

The fast wavelet transform (FWT) can be selected to further sparsify the resulting Coiflet impedance matrix (Tretiakov *et al.*, 2004). In recent years, wavelet transforms have been extensively applied to areas of wave propagation, data compression and processing (Li *et al.*, 2013; Tang *et al.*, 2015; Guan *et al.*, 2000; Tong *et al.*, 2011). The FWT converts a dense matrix produced by MoM to an extremely sparse one, of which the sparsity (percentage of the nonzero entries) can be 0.01 or less. The non-zero entries represent both singularity contributions from self-terms and non-singularity contributions from the interactions between large scale bases in the original kernel. The FWT can be classified into the standard form (SFWT) with the complexity $O(N \log N)$ and non-standard form (NSFWT) of $O(N)$ (Beylkin *et al.*, 1991; Beylkin, 1993). Nonetheless, the NSFWT is closely related to the LU matrix solver, which has no direct connection to the iterative algorithms. Therefore, we shall not discuss it further. Conversely, the SFWT is easier to implement by general matrix multiplications (Sarkar and Kim, 1999; Hesham and Hassanein, 2010; Duff *et al.*, 1986), and the solutions of the integral equations can be reconstructed by Mallats decomposition and reconstruction algorithms (Mallat, 1989) in a matrix manner. Furthermore, the SFWT can be easily programmed for parallel computing.

This dissertation is organized as follows: Chapter 2 introduces the fundamentals and properties of Coiflets. Chapter 3 discusses the fast Coiflet MFIE for scattering from open rough surfaces. Chapter 4 provides the unified numerical algorithm for 3-D scattering from dielectric and PEC random rough surfaces. Chapter 5 draws the conclusion.

Chapter 2

COIFMAN WAVELETS

Wavelets have great potentials in solving electromagnetic problems. Especially for problems that have discontinuous fields across boundaries, nonlinear wavelet based methods exhibit fast convergence. Basic wavelet theory and applications can be found in many excellent books (Daubechies, 1992; Pan, 2003).

In this chapter, we briefly introduce fundamentals and properties of Coifman wavelets.

2.1 Basic Principles

2.1.1 Scalets and Wavelets

A multi-resolution analysis (MRA) of $L^2(R)$ is defined as a sequence of closed subspaces $\{V_j\}_{j \in Z}$ of $L^2(R)$. A scaling function (or father wavelet) $\varphi \in V_0$, with a non-vanishing integral, exists such that $\varphi(t-n)$ forms a Riesz basis of V_0.

Since $\varphi \in V0 \subset V1$, a sequence $\{h_k\} \in l^2$ exists that the scaling function satisfies

$$\varphi(t) = \sum_k h_k \sqrt{2} \varphi(2t-k) \tag{2.1}$$

Equation (2.1) is called the dilation equation, where $\{h_k\}$ are coefficients of the low-pass filter and satisfies $\sum h_k = 1$. The MRA allows us to expand a function in terms of basis functions, consisting of the scalets and wavelets. And according to MRA properties, a function can be approximated with any precision by increasing the resolution in MRA.

The collection of functions $\{\varphi_{m,n}|n \in Z\}$ with

$$\varphi_{m,n}(t) = 2^{m/2}\varphi(2^m t - n) \tag{2.2}$$

forms a Riesz basis of V_m, where m denotes the scale or level and n is the translation or shift. $\varphi(t)$ is usually normalized in the following way

$$\int \varphi(t)dt = 1 \tag{2.3}$$

We use W_m to denote a space complementing V_m in V_{m+1}, that is, a space that satisfies

$$\begin{aligned} V_{m+1} &= W_m \oplus V_m \\ \bigoplus_m W_m &= L^2(R) \end{aligned} \tag{2.4}$$

A mother wavelet function (or wavelet) psi exists if the collection of functions $\{\psi(t-n)|n \in Z\}$ forms a Riesz basis of W_0. The definition of $\psi_{m,n}$ is similar to that of $\varphi_{m,n}$. Since $\varphi \in V0 \subset V1$

$$\begin{aligned} \psi(t) &= \sum_k g_k \sqrt{2}\varphi(2t-k) \\ \psi_{m,n}(t) &= 2^{m/2}\psi(2^m t - n) \end{aligned} \tag{2.5}$$

In the previous equation, the band-pass filter for the orthogonal wavelets can be represented by the low-pass filter as

$$g_k = (-1)^{k-1}h_{-(k-1)} \tag{2.6}$$

We should mention here that has also L vanishing moments

$$\int t^l \psi(t)dt = 0, \quad l = 0, 1, 2, \ldots, L-1. \tag{2.7}$$

2.1.2 *Orthogonal Properties*

From the previous discussion, it appears that for any scalet $\varphi_{m,n}(t) \in V_m$ and wavelet $\psi_{m,n}(t) \in W_m$ we have

$$\begin{aligned} V_m &= W_{m-1} \oplus V_{m-1} \\ &= W_{m-1} \oplus W_{m-2} \oplus V_{m-2} \\ &= W_{m-1} \oplus W_{m-2} \cdots \oplus W_0 \oplus V_0 \end{aligned} \tag{2.8}$$

where $\oplus$ denotes the direct sum.

The above property is the subspace decomposition and result in the following properties:

a. Scalets on the same level

$$\int \varphi_{j_0,m}(t)\varphi_{j_0,n}(t)dt = \delta_{m,n} = \begin{cases} 0 & m \neq n \\ 1 & m = n \end{cases} \tag{2.9}$$

b. Wavelets on the same level

$$\int \psi_{j_0,m}(t)\psi_{j_0,n}(t)dt = \delta_{m,n} = \begin{cases} 0 & m \neq n \\ 1 & m = n \end{cases} \tag{2.10}$$

c. Scalets are orthogonal to wavelets of the same or higher levels, regardless of the translations.

$$\int \varphi_{j_0,m}(t)\psi_{i_0,n}(t)dt = 0, j_0 \leq i_0 \tag{2.11}$$

d. Wavelets on different levels are orthogonal regardless of the translations.

$$\int \psi_{j_0,m}(t)\psi_{i_0,n}(t)dt = 0, j_0 \neq i_0 \tag{2.12}$$

2.2 Coifman Wavelets

The Coifman scaling function $\varphi(x)$ of order L is supported on $[-L, 2L-1]$ and the mother wavelet $\psi(x)$ of order L is compactly supported on $[1-1.5L, 1.5L]$. Because of the particular shape of the Coiflets we truncate the support in [-4, 4] when $L = 4$. It can be seen from Fig. 2.1 that both the scalet and wavelet are essentially zero beyond this truncated interval.

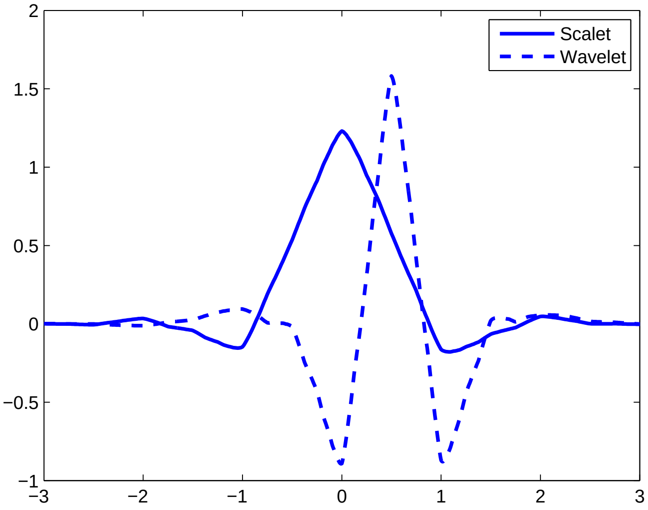

Figure 2.1: Coifman Scalet and Wavelet of $L = 4$ and $j_0 = 0$.

The Coifman wavelets of order L have the vanishing moment properties in both scaling functions and mother wavelets, as shown in equation (2.13), while the Daubechies wavelets have only vanishing moments for mother wavelets.

$$\begin{aligned} &\int \varphi(x)dx = 1 \\ &\int x^l \varphi(x)dx = 0, \quad l = 1, 2, \ldots, L-1 \\ &\int x^l \psi(x)dx = 0, \quad l = 0, 1, 2, \ldots, L-1 \end{aligned} \tag{2.13}$$

Scalets under the L^2 norm exhibit Dirac-δ like sampling property for smooth functions. Namely, if $\varphi(x)$ is supported in $[p, q]$ and $f(x)$ is expanded at a point x_0

within $[p,q]$, we can obtain

$$\begin{aligned}
&\int\limits_p^q f(x)\varphi(x-x_0)dx \\
&= \int\limits_p^q \left(f(x_0) + f'(x_0)(x-x_0) + \cdots + \tfrac{f^{L-1}(x_0)(x-x_0)^{L-1}}{(L-1)!} + \cdots \right) \varphi(x-x_0)dx \\
&= f(x_0) + O(h^L)
\end{aligned} \tag{2.14}$$

where h is the step size, and $|x-x_0| \le h$.

The property of equation (2.14) in a simple sense is similar to the Dirac-δ function property

$$\int f(x)\delta(x-x_0)dx = f(x_0) \tag{2.15}$$

The Dirac-δ like nature of the Coiflets can simplify quadrature computation into a single point value in certain cases, and thus greatly expedite the matrix element evaluations.

To explicitly explain the zero moment property (2.13), the first seven moment integrals for Coifman scalets of order $L = 4$ are presented in Table 2.1. The scalets have three exactly zero moments, according to (2.13). And the addition (approximate) zero moment in Table 2.1 results in the error of $O(h^5)$ in (2.14) for $L = 4$. Though the pulse based MoM matrix can also be evaluated with the one point quadrature formula, the difference is that in the pulse scheme the one point quadrature rule is $O(h)$ approximation Pan *et al.* (2004).

As shown in Fig. 2.2, a typical example of a perfectly conducting circular cylinder excited by a plane wave is discussed here, for the comparison between Coiflets based MoM and pulse method. The analytical solution to this problem is also included as a reference (Harrington, 2001). The cylinder is assumed to be infinity along z-axis, resulting in a 2-D problem at present. Only TE case is considered with 64 sampling points along the entire circle, since the sampling direction in TM case is transverse to the direction of the excited current which results in the non-sensitive current density and far fields. Fig. 2.3 depicts the normalized magnitude of the current on the cylinder, and Fig. 2.4 illustrates the scattering cross section. The relative errors to the analytical solutions are also displayed. Here it can be seen that the superiority of Coiflets are highlighted in TE cases, in which Coiflets achieve higher accuracy with, e.g. the relative error within 1%, than pulse under the same sampling points.

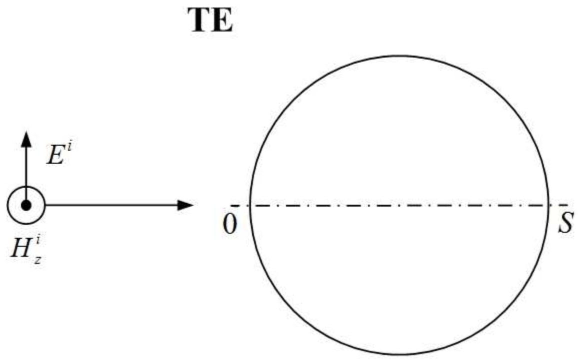

Figure 2.2: A Perfectly Conducting Circular Cylinder with a Plane Wave Incident (300MHz, TE Case). The Cylinder Is Assumed to Be Infinity along Z-Axis, Which Is Perpendicular to the Cross Section of the Cylinder.

Table 2.1: Moment Integrals for Coifman Scalets of Order $L = 4$

n	moment integral value
0	1.0000000
1	0.0000000
2	0.0000000
3	0.0000000
4	4.9333e-11
5	-0.1348373
6	3.5308e-10

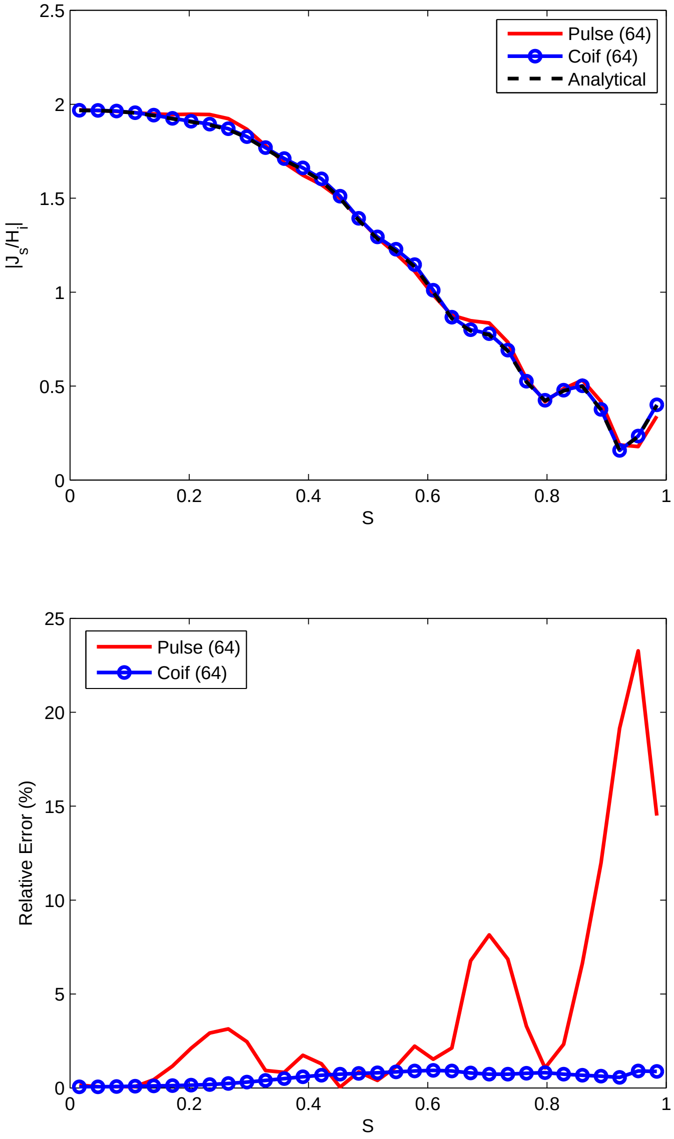

Figure 2.3: The Excited Current Density Comparisons among Pulse, Coiflet and Analytical Methods, for the Problem of a Conducting Circular Cylinder Illuminated by a Plane Wave (TE Case). The Normalized Current Magnitude and the Relative Error to the Analytical Solutions Are Included. The 64 Sampling Points Are for Both Pulse Case and Coiflet Case.

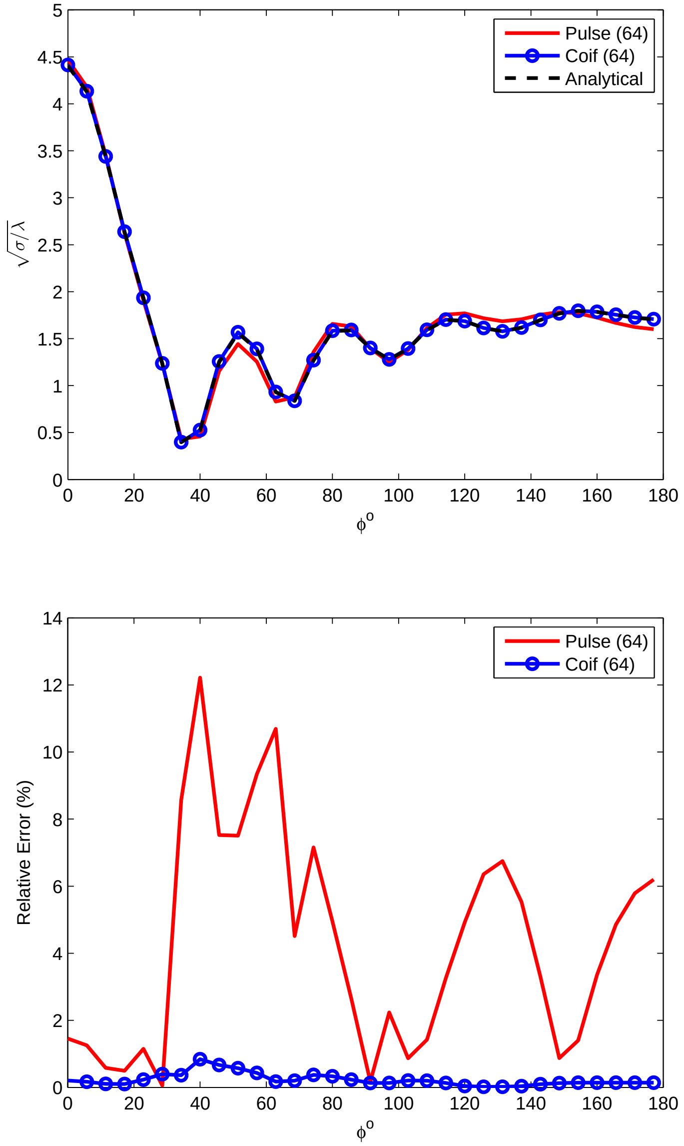

Figure 2.4: The Scattered Field Pattern Comparisons among Pulse, Coiflet and Analytical Methods, for the Problem of a Conducting Circular Cylinder Illuminated by a Plane Wave (TE Case). The Normalized RCS and the Relative Error to the Analytical Solutions Are Included. The 64 Sampling Points Are for Both Pulse Case and Coiflet Case.

Chapter 3

FAST COIFLET MFIE FOR SCATTERING FROM OPEN ROUGH SURFACES

Scattering of electromagnetic waves from rough surfaces has great applications in microwave remote sensing. Both analytical approaches and numerical methods have been extensively researched. One of the most popular numerical solutions is the integral equation method discretized by the method of moments (MoM). The electric field integral equation (EFIE) and magnetic field integral equation (MFIE) are two important integral equations (Yl-Oijala *et al.*, 2012). Contrary to the EFIE, the MFIE is well-posed and renders good condition numbers of the corresponding impedance matrix, since the K operator is compact and all the eigenvalues are clustered around a non-zero value. As a result, the iterative solvers converge rapidly under the MFIE formulation (Chew *et al.*, 2008). Despite the advantages of the MFIE, in engineering RCS societies the EFIE has been dominant while MFIE is recognized as very inaccurate in handling geometrical singularity. The inaccuracy and slow convergence of the MFIE-RWG were reported in (Gurel and Ergul, 2005; Ubeda and Rius, 2006, 2005; Warnick and Peterson, 2007). A novel mixed discretization scheme for the MFIE has been recently proved a possible solution to the above problems Cools *et al.* (2011).

The Coiflets based MFIE has been applied to 3-D scattering problems in the previous studies that do not rely on the RWG discretization Pan *et al.* (2004); Wang and Pan (2013); Pan *et al.* (2014). Due to their high concentration in both the spatial and spectral domains, wavelets allow significant reduction of the sampling rate from 10 points per wavelength to 4 or 5, dramatically reducing the size of the matrix Daubechies (1992); Pan (2003). Additionally, the vanishing moments of the Coiflets of order $L = 4$ provide one-point quadrature of precision $O(h^5)$, reducing the computational effort in filling matrix entries from $O(N^2)$ to $O(N)$.

In (Wang and Pan, 2013) the Coiflet based MFIE was used to solve scattering from infinite arrays of sharp conducting cones, under uniform plane wave illumination and the Floquet condition. In handling geometrical singularity on the closed structure, it was shown to be very accurate with fast convergence. In (Pan *et al.*, 2004), this method was applied to truncated rough surfaces, where a tapered wave (Braunisch *et al.*, 2000) was applied as the incident to resemble the plane wave near the scattering center. The tapered wave decays rapidly to negligibly weak before reaching surface edges and it extends the range of MFIE to open surfaces. The aforementioned Coiflet based MFIE method on open surfaces may remarkably save computational resources and achieve fast convergence. In (Pan *et al.*, 2014) our main interest was the radiometer calibration target, a finite sized array of sharp cones. Working toward this goal, we paid attention to singularity removal, geometric non-smooth treatment, and deployment of both scalets and wavelets, namely, the multiresolution analysis (MRA). Without sufficient details, the SFWT was briefly introduced in (Pan *et al.*, 2014) to calculate algorithm complexity for the sphere.

On the contrary, here we focus on the SFWT, the tradeoff between matrix sparsity and solution precision. Instead of a specialized, problem-dependent basis for solving the MFIE, the current manuscript assesses the SFWT algorithm with a more general problem of closed surface objects of the almond and the ogive, and extends the application to an open structure of the random rough surface. The aforementioned closed surface examples are designated for accuracy validation of the algorithm because no high-precision remote sensing examples of open surfaces are available to compare with. The sphere is smooth and it has closed form expressions. Contrarily, the almond or the ogive possesses a sharp vertex with geometric discontinuity, and it has been studied in many publications with well-known numerical and measurement data (Woo *et al.*, 93), from which we selected one data set below the 1st resonance. For surfaces described by numerical data, e.g. rough surfaces, the method also works.

In recent years, wavelet transforms have been extensively applied to areas of wave propagation, data compression and processing (Li *et al.*, 2013; Tang *et al.*, 2015; Guan *et al.*, 2000; Tong *et al.*, 2011). The FWT converts a dense matrix produced by MoM to an extremely sparse one, of which the sparsity (percentage of the nonzero entries) can be 0.01 or less. The non-zero entries represent both singularity contributions from self-terms and non-singularity contributions from the interactions between large scale bases in the original kernel. The FWT can be classified into the standard form (SFWT) with the complexity $O(N \log N)$ and non-standard form (NSFWT) of $O(N)$ (Beylkin *et al.*, 1991; Beylkin, 1993). Nonetheless, the NSFWT is closely related to the LU matrix solver, which has no direct connection to the iterative algorithms. Therefore, we shall not discuss it further in this paper. Conversely, the SFWT is easier to implement by general matrix multiplications (Sarkar and Kim, 1999; Hesham and Hassanein, 2010; Duff *et al.*, 1986), and the solutions of the integral equations can be reconstructed by Mallats decomposition and reconstruction algorithms (Mallat, 1989) in a matrix manner. Furthermore, the SFWT can be easily programmed for parallel computing.

Two types of complexity analysis were conducted in (Pan *et al.*, 2014), specifically, fixed frequency with decreasing discretization size and fixed discretization with increasing frequency. At the beginning, matrix assembling time for both types steadily increased in $O(N)$ due to one-point quadrature. It gradually rose in $O(N \log N)$ when the number of unknowns got very large because the number of off-diagonal elements grew in the squared fashion. In addition, the memory consumption for non-zero entries after SFWT sparsification was scaled as $O(N^{1/10} \log N)$ and $O(N^{6/5} \log N)$ for the fixed frequency and fixed discretization, respectively. In generating the total transformation matrix, the lowest level was naturally chosen as $j_l = 0$ in the SFWT. In such a configuration, the MRA was implemented on all distinctive levels, to achieve the maximum sparsification. However, the low level factor matrices underwent heavy truncation that produced relatively large errors. Based upon the discussion above and numerical computations, we change the lowest level to be $j_l = 3$ in the current paper to balance the accuracy and sparsity. Comparing the results in (Pan *et al.*, 2014), the RMS error of the RCS has been reduced from 0.1 to 0.03, while the sparsity only degraded by 0.85%.

Using FEKO (FEKO, 2015), RWG-MLFMA based commercial software, numerical results are compared with good agreement. Such comparisons are aimed to validate the accuracy of the algorithm. Commercial codes are optimized with effective user friendly interfaces and are more efficient in terms of the CPU time. From the provided numerical results, the new algorithm may achieve similar precision as FEKO does, yet use less unknowns and require fewer iterations.

In this chapter, we provide formulation and implementation of the SFWT under scalar discretization of the MFIE. Computational complexity and accuracy of the algorithm are discussed, followed by the example of random rough surface scattering.

3.1 Formulation

3.1.1 Coiflets based Scalar MFIE

The general vector form of 3-D MFIE for a perfect electric conductor is

$$\vec{J}(\vec{r}) = 2\hat{n} \times \vec{H}_i(\vec{r}) + 2\hat{n} \times \int\limits_S \vec{J}(\vec{r}') \times \nabla' g(\vec{r}, \vec{r}') ds' \qquad (3.1)$$

where

$$g(\vec{r}, \vec{r}') = \frac{e^{-jkR}}{4\pi R}$$
$$\nabla' g(\vec{r}, \vec{r}') = \frac{(1 + jkR)e^{-jkR}}{4\pi R^3}\vec{R} = -G(R)\vec{R}$$

$\vec{R} = \vec{r} - \vec{r}'$ represents the distance from the source to field point.

2-D MFIE is a special case of 3-D one, as

$$\vec{J}(\vec{\rho}) = 2\hat{n} \times \vec{H}_i(\vec{\rho}) + 2\hat{n} \times \int\limits_C \vec{J}(\vec{\rho}') \times \nabla' g(\vec{\rho}, \vec{\rho}')dl' \tag{3.2}$$

where

$$g(\vec{\rho}, \vec{\rho}') = \frac{j}{4}H_0^{(2)}(k|\vec{\rho} - \vec{\rho}'|)$$
$$\nabla g'(\vec{\rho}, \vec{\rho}') = -\frac{jk}{4}H_1^{(2)}(k|\vec{\rho} - \vec{\rho}'|)\hat{R}$$

The 3-D scattering problem is formulated by recasting the vector MFIE into coupled two scalar equations in terms of only two surface current components. The Coiflets of order $L = 4$ are discussed here. Both Coifman scalets and wavelets have the vanishing moments, namely

$$\begin{aligned} &\int \varphi(x)\mathrm{d}x = 1 \\ &\int x^\ell \varphi(x)\mathrm{d}x = 0\ , \quad \ell = 1, 2, \ldots, L-1 \\ &\int x^\ell \psi(x)\mathrm{d}x = 0\ , \quad \ell = 0, 1, 2, \ldots, L-1 \end{aligned} \tag{3.3}$$

In (3.3), the scalets exhibit a Dirac-δ like nature, allowing us to reduce the quadrature computation of most matrix entries into a single point value and thus greatly cut down the matrix filling calculations from $O(N^2)$ to $O(N)$.

Specifically, in 3-D rough surface scattering, we define

$$R = \sqrt{(x - x')^2 + (y - y')^2 + [f(x, y) - f(x', y')]^2} \tag{3.4}$$

where f is the profile of the rough surface.

Since

$$\hat{n} = \vec{n}\cos\chi = \begin{pmatrix} -\frac{\partial f(x,y)}{\partial x} \\ -\frac{\partial f(x,y)}{\partial y} \\ 1 \end{pmatrix} \cos\chi \tag{3.5}$$

where

$$\cos\chi = \left\{ \left[\frac{\partial f(x,y)}{\partial x} \right]^2 + \left[\frac{\partial f(x,y)}{\partial y} \right]^2 + 1 \right\}^{-\frac{1}{2}}$$

Let

$$\vec{F}(\vec{r}) = \frac{\vec{J}(\vec{r})}{\cos\chi} = \vec{J}(\vec{r}) \left\{ \left[\frac{\partial f(x,y)}{\partial x} \right]^2 + \left[\frac{\partial f(x,y)}{\partial y} \right]^2 + 1 \right\}^{\frac{1}{2}} \tag{3.6}$$

Thus, (3.1) can be reformulated into

$$\frac{\vec{F}(\vec{r})}{2} + \int \vec{n} \times [\vec{F}(\vec{r}') \times \vec{R}G(R)] dx'dy' = \vec{n} \times \vec{H}_i(\vec{r}) \tag{3.7}$$

For the right side of (3.7),

$$\begin{aligned} \vec{n} \times \vec{H}_i(\vec{r}) &= \begin{pmatrix} -\frac{\partial f(x,y)}{\partial x} \\ -\frac{\partial f(x,y)}{\partial y} \\ 1 \end{pmatrix} \times \begin{pmatrix} H_{ix} \\ H_{iy} \\ H_{iz} \end{pmatrix} \\ &= (-\frac{\partial f(x,y)}{\partial y} H_{iz} - H_{iy})\hat{x} + (\frac{\partial f(x,y)}{\partial x} H_{iz} + H_{ix})\hat{y} \\ &\qquad + (-\frac{\partial f(x,y)}{\partial x} H_{iy} + \frac{\partial f(x,y)}{\partial y} H_{ix})\hat{z} \end{aligned} \tag{3.8}$$

For the second term on the left side of (3.7),

$$\vec{n} \times [\vec{F}(\vec{r}') \times \vec{R}G(R)] = \vec{F}(\vec{r}')[\vec{n} \cdot \vec{R}G(R)] - \vec{R}G(R)[\vec{n} \cdot \vec{F}(\vec{r}')] \tag{3.9}$$

X component: $F_x(\vec{r}')(\vec{n} \cdot \vec{R})G(R) - G(R)(\vec{R} \cdot \hat{x})[\vec{n} \cdot \vec{F}(\vec{r}')]$

Y component: $F_y(\vec{r}')(\vec{n} \cdot \vec{R})G(R) - G(R)(\vec{R} \cdot \hat{y})[\vec{n} \cdot \vec{F}(\vec{r}')]$

Given $\vec{n} \cdot \vec{J} = 0$, we can get

$$F_z = \frac{\partial f(x,y)}{\partial x} F_x + \frac{\partial f(x,y)}{\partial y} F_y \tag{3.10}$$

The vector form of MFIE in (3.1) can be recast into the scalar form in terms of x and y components, as

$$\begin{aligned}&\frac{F_x(\vec{r})}{2}+\frac{\partial f(x,y)}{\partial y}\int dx'dy'G(R)[(x-x')F_y(\vec{r}')-(y-y')F_x(\vec{r}')]\\&\quad+\int dx'dy'G(R)\left\{[-(x-x')\frac{\partial f(x',y')}{\partial x'}+f(x,y)-f(x',y')]F_x(\vec{r}')\right.\\&\quad\left.-(x-x')\frac{\partial f(x',y')}{\partial y'}F_y(\vec{r}')\right\}\\&\quad=-\frac{\partial f(x,y)}{\partial y}H_{iz}(\vec{r})-H_{iy}(\vec{r})\end{aligned}\tag{3.11}$$

and

$$\begin{aligned}&\frac{F_y(\vec{r})}{2}-\frac{\partial f(x,y)}{\partial x}\int dx'dy'G(R)[(x-x')F_y(\vec{r}')-(y-y')F_x(\vec{r}')]\\&\quad+\int dx'dy'G(R)\left\{[-(y-y')\frac{\partial f(x',y')}{\partial y'}+f(x,y)-f(x',y')]F_y(\vec{r}')\right.\\&\quad\left.-(y-y')\frac{\partial f(x',y')}{\partial x'}F_x(\vec{r}')\right\}\\&\quad=\frac{\partial f(x,y)}{\partial x}H_{iz}(\vec{r})+H_{ix}(\vec{r})\end{aligned}\tag{3.12}$$

where

$$\begin{aligned}G(R)&=\frac{(-1-jkR)e^{-jkR}}{4\pi R^3}\\F_x(\vec{r})&=\left\{\left[\frac{\partial f(x,y)}{\partial x}\right]^2+\left[\frac{\partial f(x,y)}{\partial y}\right]^2+1\right\}^{\frac{1}{2}}\vec{J}(\vec{r})\cdot\hat{x}\\F_y(\vec{r})&=\left\{\left[\frac{\partial f(x,y)}{\partial x}\right]^2+\left[\frac{\partial f(x,y)}{\partial y}\right]^2+1\right\}^{\frac{1}{2}}\vec{J}(\vec{r})\cdot\hat{y}\end{aligned}\tag{3.13}$$

We apply the Galerkin based MoM to solve the coupled integral equations (3.11) and (3.12). Specifically, we use Coifman wavelets as basis and testing functions. First we expand the unknowns in terms of Coiflets

$$\begin{aligned}F_x(\vec{r})&=\sum_i\sum_j\alpha_{ij}\varphi_{j_0,i}(x)\varphi_{j_0,j}(y)\\F_y(\vec{r})&=\sum_i\sum_j\beta_{ij}\varphi_{j_0,i}(x)\varphi_{j_0,j}(y)\end{aligned}\tag{3.14}$$

We substitute the above expansions into (3.11) and multiply $\varphi_{j_0,m}(x)\varphi_{j_0,n}(y)$ to both sides

$$\begin{aligned}
&\sum_{ij}\frac{\alpha_{ij}}{2}\int \varphi_{j_0,i}(x)\varphi_{j_0,j}(y)\varphi_{j_0,m}(x)\varphi_{j_0,n}(y)dxdy \\
&+\frac{\partial f(x,y)}{\partial y}\int dx'dy'\int dxdy\varphi_{j_0,m}(x)\varphi_{j_0,n}(y)G(R)\Bigg[(x-x')\sum_{ij}\beta_{ij}\varphi_{j_0,i}(x')\varphi_{j_0,j}(y') \\
&-(y-y')\sum_{ij}\alpha_{ij}\varphi_{j_0,i}(x')\varphi_{j_0,j}(y')\Bigg]+\int dx'dy'\int dxdy\varphi_{j_0,m}(x)\varphi_{j_0,n}(y)G(R) \\
&\times\Bigg\{\left[-(x-x')\frac{\partial f(x',y')}{\partial x'}+f(x,y)-f(x',y')\right]\sum_{ij}\alpha_{ij}\varphi_{j_0,i}(x')\varphi_{j_0,j}(y') \\
&-(x-x')\frac{\partial f(x',y')}{\partial y'}\sum_{ij}\beta_{ij}\varphi_{j_0,i}(x')\varphi_{j_0,j}(y')\Bigg\} \\
&=\int dxdy\varphi_{j_0,m}(x)\varphi_{j_0,n}(y)\left[-\frac{\partial f(x,y)}{\partial y}H_{iz}(\vec{r})-H_{iy}(\vec{r})\right]
\end{aligned} \tag{3.15}$$

Since

$$\begin{aligned}
\phi_{j_0,m}(x)&=2^{j_0/2}\phi(2^{j_0}x-m) \\
\phi_{j_0,n}(y)&=2^{j_0/2}\phi(2^{j_0}y-n)
\end{aligned} \tag{3.16}$$

Imposing orthogonality and one point quadrature, we arrive at

$$\begin{aligned}
&\frac{\alpha_{mn}}{2}+\sum_{ij}\alpha_{ij}\left(\frac{1}{2^{j_0/2}}\right)^4 G(x_i,y_j;x_m,y_n) \\
&\times\left\{-(y_n-y_j)\frac{\partial f(x_m,y_n)}{\partial y}-(x_m-x_i)\frac{\partial f(x_i,y_j)}{\partial x}+[f(x_m,y_n)-f(x_i,y_j)]\right\} \\
&+\sum_{ij}\beta_{ij}\left(\frac{1}{2^{j_0/2}}\right)^4 G(x_i,y_j;x_m,y_n)\left\{(x_m-x_i)\left[\frac{\partial f(x_m,y_n)}{\partial y}-\frac{\partial f(x_i,y_j)}{\partial y}\right]\right\} \\
&=-\left(\frac{1}{2^{j_0/2}}\right)^2\left[\frac{\partial f(x_m,y_n)}{\partial y}H_{iz}(x_m,y_n)+H_{iy}(x_m,y_n)\right]
\end{aligned} \tag{3.17}$$

In the same manner, (3.12) can be discretized as

$$\frac{\beta_{mn}}{2} + \sum_{ij} \alpha_{ij} \left(\frac{1}{2^{j_0/2}}\right)^4 G(x_i, y_j; x_m, y_n) \left\{ (y_n - y_j) \left[\frac{\partial f(x_m, y_n)}{\partial x} - \frac{\partial f(x_i, y_j)}{\partial x} \right] \right\}$$
$$+ \sum_{ij} \beta_{ij} \left(\frac{1}{2^{j_0/2}}\right)^4 G(x_i, y_j; x_m, y_n)$$
$$\times \left\{ -(x_m - x_i) \frac{\partial f(x_m, y_n)}{\partial x} - (y_n - y_j) \frac{\partial f(x_i, y_j)}{\partial y} + [f(x_m, y_n) - f(x_i, y_j)] \right\}$$
$$= \left(\frac{1}{2^{j_0/2}}\right)^2 \left[\frac{\partial f(x_m, y_n)}{\partial x} H_{iz}(x_m, y_n) + H_{ix}(x_m, y_n) \right] \tag{3.18}$$

The matrix form of the discretized MFIE is

$$\left(\frac{\gamma^2}{2}\mathbf{I} + \mathrm{Z}\right) \mathrm{X} = \mathbf{b} \tag{3.19}$$

I is the identity matrix, and

$$\mathrm{Z} = \begin{bmatrix} Q & R \\ S & T \end{bmatrix} \tag{3.20}$$

$$\mathrm{X} = \begin{bmatrix} \alpha_{mn} \\ \beta_{mn} \end{bmatrix} \tag{3.21}$$

$$\mathbf{b} = \begin{bmatrix} h_{mn} \\ k_{mn} \end{bmatrix} \tag{3.22}$$

where

$$\begin{aligned} \gamma &= 2^{j_0} \\ h_{mn} &= \gamma \left[-\frac{\partial f(x_m, y_n)}{\partial y} H_{iz}(x_m, y_n) - H_{iy}(x_m, y_n) \right] \\ k_{mn} &= \gamma \left[\frac{\partial f(x_m, y_n)}{\partial x} H_{iz}(x_m, y_n) + H_{ix}(x_m, y_n) \right] \end{aligned} \tag{3.23}$$

$$
\begin{aligned}
Q &= G(x_i, y_j; x_m, y_n) \\
&\times \left\{ -(y_n - y_j)\frac{\partial f(x_m, y_n)}{\partial y} - (x_m - x_i)\frac{\partial f(x_i, y_j)}{\partial x} + [f(x_m, y_n) - f(x_i, y_j)] \right\} \\
R &= G(x_i, y_j; x_m, y_n) \\
&\times \left\{ (x_m - x_i)\left[\frac{\partial f(x_m, y_n)}{\partial y} - \frac{\partial f(x_i, y_j)}{\partial y}\right] \right\} \\
S &= G(x_i, y_j; x_m, y_n) \\
&\times \left\{ (y_n - y_j)\left[\frac{\partial f(x_m, y_n)}{\partial x} - \frac{\partial f(x_i, y_j)}{\partial x}\right] \right\} \\
T &= G(x_i, y_j; x_m, y_n) \\
&\times \left\{ -(x_m - x_i)\frac{\partial f(x_m, y_n)}{\partial x} - (y_n - y_j)\frac{\partial f(x_i, y_j)}{\partial y} + [f(x_m, y_n) - f(x_i, y_j)] \right\}
\end{aligned}
$$

For the incident wave with horizontal polarization, the bistatic scattering coefficient in Region 1 is defined as

$$
\sigma_\alpha = \gamma_{\alpha h} = 4\pi \frac{|E_\alpha^s|^2}{2\eta P_{inc}} \qquad (\alpha = h, v) \tag{3.24}
$$

P_{inc} is the real incident power, and

$$
\begin{aligned}
E_h^s &= -\frac{jk\eta}{4\pi} \int dx' dy' e^{jkr' \cos\psi} \\
&\quad \times [-F_x(x', y') \sin\phi_s + F_y(x', y') \cos\phi_s] \\
E_v^s &= -\frac{jk\eta}{4\pi} \int dx' dy' e^{jkr' \cos\psi} \\
&\quad \times \left\{ F_x(x', y') \left[\cos\theta_s \cos\phi_s - \frac{\partial f(x', y')}{\partial x'} \sin\theta_s\right] \right. \\
&\quad \left. + F_y(x', y') \left[\cos\theta_s \sin\phi_s - \frac{\partial f(x', y')}{\partial y'} \sin\theta_s\right] \right\}
\end{aligned} \tag{3.25}
$$

where

$$
r' \cos\psi = x' \sin\theta_s \cos\phi_s + y' \sin\theta_s \sin\phi_s + f(x', y') \cos\theta_s \tag{3.26}
$$

3.1.2 Matrix Sparsification Using SFWT

Using Galerkin's procedure and wavelet basis functions, an operator equation

$$(Tf)(x) = g(x) \tag{3.27}$$

can be discretized into a matrix equation at level j as

$$[T^j]|c^j\rangle = |g^j\rangle \tag{3.28}$$

The continuous operator and discrete operator are related by

$$T = \lim_{j\to\infty}(P_j T P_j) = \lim_{j\to\infty}(T^j) \tag{3.29}$$

where T^j is the projection of T onto V_j and tested in V_j. The FWT has been generally classified into non-standard form and standard form towards the sparsification of an existing impedance matrix (Pan, 2003).

Non-standard form:

Since

$$V_{j+1} = V_j \bigoplus W_j, \quad \varphi \in V \text{ and } \psi \in W$$

$$T^{j+1} = \begin{bmatrix} A^{jj} & B^{jj} \\ C^{jj} & T^j \end{bmatrix} \tag{3.30}$$

where

$$\begin{aligned}
A^{jj}_{kk'} &= \langle \psi_{j,k}, T(\psi_{j,k'})\rangle = \sum_n \sum_m g_{n-2k} g_{m-2k'} T^{j+1}_{n,m} \\
B^{jj}_{kk'} &= \langle \psi_{j,k}, T(\varphi_{j,k'})\rangle = \sum_n \sum_m g_{n-2k} h_{m-2k'} T^{j+1}_{n,m} \\
C^{jj}_{kk'} &= \langle \varphi_{j,k}, T(\psi_{j,k'})\rangle = \sum_n \sum_m h_{n-2k} g_{m-2k'} T^{j+1}_{n,m} \\
T^{j}_{kk'} &= \langle \varphi_{j,k}, T(\varphi_{j,k'})\rangle = \sum_n \sum_m h_{n-2k} h_{m-2k'} T^{j+1}_{n,m}
\end{aligned} \tag{3.31}$$

h and g are the lowpass and bandpass filter banks, respectively, and are well tabulated in wavelet books Pan (2003).

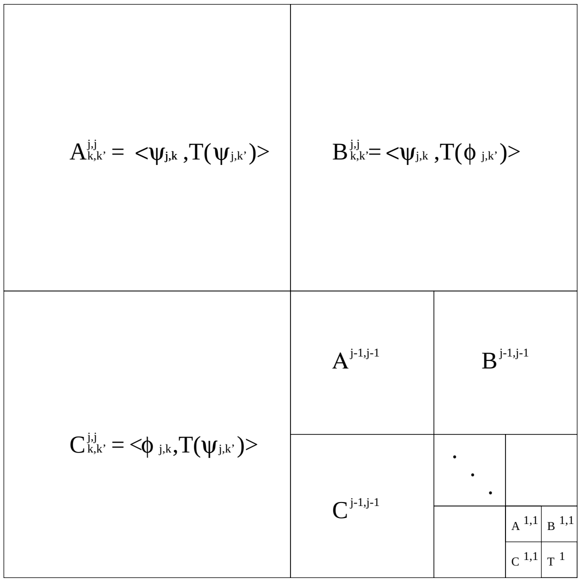

Figure 3.1: Nonstandard Form Representation of a Decomposed Matrix.

In (3.30), submatrix A^{jj} is very sparse since both of the expansion and testing functions are wavelets ψ, while submatrix T^j is dense because both of the expansion and testing functions are scalets φ. Repeating the previous procedures to the submatrices $T^j, T^{j-1}, \ldots$, we may decompose the matrix T^{j+1} into a telescopic structure known as the nonstandard form, as illustrated in Fig. 3.1.

Standard form:

In the nonstandard-form decomposition, one only manipulates the diagonal submatrices. If we also work on the off-diagonal submatrices B^{jj} and C^{jj}, which are composed of a mix of scalets and wavelets, we then decomposed the matrix T^{j+1} into the standard form. The lower-left quarter C^{jj} can be decomposed as

$$C^{\ell,j} = \begin{bmatrix} A^{\ell-1,j} \\ C^{\ell-1,j} \end{bmatrix}, \quad \ell = j,\ j-1,\ \cdots,\ 1 \tag{3.32}$$

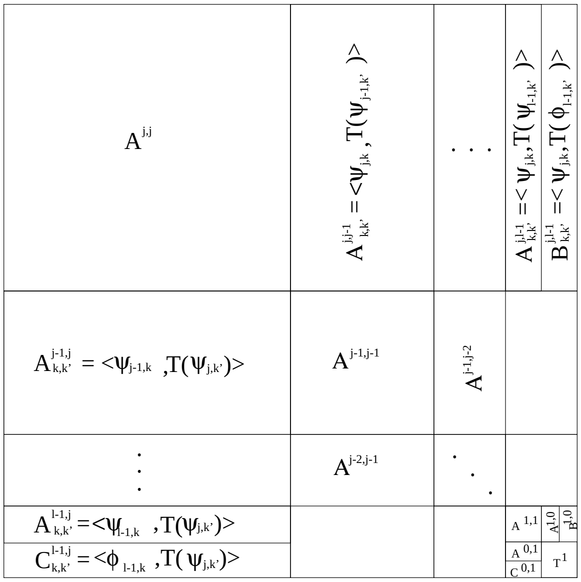

Figure 3.2: Standard Form Representation of a Decomposed Matrix.

where

$$\begin{aligned} A^{\ell-1,j}_{k,k'} &= \sum_n g_{n-2k} C^{\ell,j}_{n,k'} \\ C^{\ell-1,j}_{k,k'} &= \sum_n h_{n-2k} C^{\ell,j}_{n,k'} \end{aligned} \tag{3.33}$$

In the same manner, the upper-right quarter

$$B^{j,\ell} = \left[A^{j,\ell-1} B^{j,\ell-1} \right], \ell = j, j-1, \cdots, 1 \tag{3.34}$$

where

$$\begin{aligned} A^{j,l-1}_{k,k'} &= \sum_n g_{n-2k'} B^{j,l}_{k,n} \\ B^{j,l-1}_{k,k'} &= \sum_n h_{n-2k'} B^{j,l}_{k,n} \end{aligned} \tag{3.35}$$

The overview of the resulting matrix is shown in Fig. 3.2. And Fig. 3.3 displays an example impedance matrix resulting from a perfectly electrically conducting (PEC) circular cylinder (infinity length) illustrated by a plane wave. There are 1024 sampling points along the entire circle and the non-zero entries after SFWT count only 0.35% of the original impedance matrix.

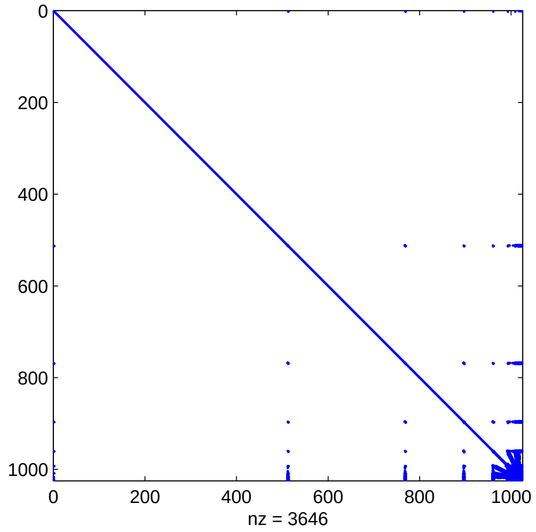

Figure 3.3: Impedance Matrix of the Standard FWT (Threshold = 1×10^{-3}) for a PEC Circular Cylinder Illuminated by a Plane Wave (300MHz, TE Case). The Cylinder Length Is Infinity and There Are 1024 Sampling Points along the Entire Circle.

3.1.3 SFWT Implementation with Matrix Form

We begin with a 1-D transformation matrix of dimension $N \times N$, where N is chosen to be an integer of power 2 to match the dilation equations. Assume $N = 2^{j_h}$, where j_h is the finest (highest) level of the impedance matrix as the input of SFWT. When the level shifts from j_h to j_l, the coarsest (lowest) level, the transformation matrices of different size are generated. The choice of level j_l depends on the size of the non-zero filter bank coefficients of the individual wavelets and it affects the solution accuracy and matrix sparsity.

The conventional SFWT introduced above can be reorganized in terms of the matrix form, e.g. (3.36) is a 1-D transformation matrix on $(j_h - 1)$ level (Pan *et al.*, 2014). Both the lowpass filter coefficients h and bandpass filter coefficients g are of Coiflets of order $L = 4$. The subsampling by factor 2 is accomplished by the shift between the elements of each row in this transformation matrix.

$$P_{j_h-1} = [P]_{2^{j_h}\times 2^{j_h}} = \left[\begin{array}{l}
g_0 \; g_1 \; g_2 \; g_3 \; g_4 \; g_5 \; 0 \cdots \\
g_{-2} \; g_{-1} \; g_0 \; g_1 \; g_2 \; g_3 \; g_4 \; g_5 \; 0 \cdots \\
g_{-4} \; g_{-3} \; g_{-2} \; g_{-1} \; g_0 \; g_1 \; g_2 \; g_3 \; g_4 \; g_5 \; 0 \cdots \\
g_{-6} \; g_{-5} \; g_{-4} \; g_{-3} \; g_{-2} \; g_{-1} \; g_0 \; g_1 \; g_2 \; g_3 \; g_4 \; g_5 \; 0 \; \cdots \\
\qquad\qquad\qquad\qquad\qquad\qquad\qquad\qquad \ddots \\
\qquad\qquad\qquad\qquad\qquad\qquad\qquad\qquad \cdots \; 0 \; g_{-6} \; g_{-5} \; g_{-4} \; g_{-3} \; g_{-2} \; g_{-1} \; g_0 \; g_1 \; g_2 \; g_3 \\
\qquad\qquad\qquad\qquad\qquad\qquad\qquad\qquad\qquad\quad \cdots \; 0 \; g_{-6} \; g_{-5} \; g_{-4} \; g_{-3} \; g_{-2} \; g_{-1} \; g_0 \; g_1 \\
\hline \\
h_0 \; h_1 \; h_2 \; h_3 \; h_4 \; h_5 \; h_6 \; h_7 \; 0 \cdots \\
h_{-2} \; h_{-1} \; h_0 \; h_1 \; h_2 \; h_3 \; h_4 \; h_5 \; h_6 \; h_7 \; 0 \cdots \\
h_{-4} \; h_{-3} \; h_{-2} \; h_{-1} \; h_0 \; h_1 \; h_2 \; h_3 \; h_4 \; h_5 \; h_6 \; h_7 \; 0 \; \cdots \\
\qquad\quad h_{-4} \; h_{-3} \; h_{-2} \; h_{-1} \; h_0 \; h_1 \; h_2 \; h_3 \; h_4 \; h_5 \; h_6 \; h_7 \; 0 \; \cdots \\
\qquad\qquad\qquad\qquad\qquad\qquad\qquad\qquad \ddots \\
\qquad\qquad\qquad\qquad\qquad\qquad\qquad\qquad\qquad\quad \cdots \; 0 \; h_{-4} \; h_{-3} \; h_{-2} \; h_{-1} \; h_0 \; h_1 \; h_2 \; h_3 \\
\qquad\qquad\qquad\qquad\qquad\qquad\qquad\qquad\qquad\qquad\qquad \cdots \; 0 \; h_{-4} \; h_{-3} \; h_{-2} \; h_{-1} \; h_0 \; h_1
\end{array}\right]_{N\times N} \tag{3.36}$$

A diagonal unity matrix is added to the original transformation matrix on j-th level, to realize the equal matrix size of P_j. Then the total transformation matrix S in 1-D case can be obtained as a product of the matrices P_j, namely

$$S_{1D} = P_{j_l} P_{j_l+1} \ldots P_{j_h-1} \tag{3.37}$$

where

$$P_j = \begin{bmatrix} I_{(2^{j_h}-2^{j+1})\times(2^{j_h}-2^{j+1})} & 0 \\ 0 & [P]_{2^{j+1}\times 2^{j+1}} \end{bmatrix} \tag{3.38}$$

$$j = j_h - 1, \ldots, j_l + 1, j_l.$$

Assume the system equation before the SFWT is $TX = g$, where X is the unknown. Apply the SFWT using the total transformation matrix S, the new system equation becomes (Pan *et al.*, 2014)

$$T'X' = g' \tag{3.39}$$

where

$$T' = STS^t, g' = Sg \tag{3.40}$$

upon the solution of X', the original unknown is obtained by

$$X = S^t X' \tag{3.41}$$

It has to be specified that the original transformation matrices are not perfectly orthonormal, since in the conventional SFWT the truncations of filter banks are inevitably involved beginning with $(j_h - 1)$ level and getting heavier in the rest levels. More specifically here, for Coiflets of order $L = 4$, both lowpass and bandpass filter banks consist of 12 nonzero elements respectively, e.g. the lowpass bank has nonzeros of $h_{-4}, h_{-3}, h_{-2}, \ldots h_7$. Starting from the lowest resolution level 0 in the conventional SFWT, the original transformation matrices are

$$\begin{aligned}
&j = 0, \quad [P]_{2\times 2} = \begin{bmatrix} g_0 & g_1 \\ h_0 & h_1 \end{bmatrix}; \\
&j = 1, \quad [P]_{4\times 4} = \begin{bmatrix} g_0 & g_1 & g_2 & g_3 \\ g_{-2} & g_{-1} & g_0 & g_1 \\ h_0 & h_1 & h_2 & h_3 \\ h_{-2} & h_{-1} & h_0 & h_1 \end{bmatrix}; \\
&\quad \ldots \\
&j = j, \quad [P]_{2^{j+1}\times 2^{j+1}}; \\
&\quad \ldots
\end{aligned} \tag{3.42}$$

The cumulative impact of the truncation error on accuracy is noticeable especially for electrically large problems. Heavy truncations produce relatively large errors in constructing the total transformation matrix S. In other words, S is not a perfectly orthonormal matrix. Considering the tradeoff between accuracy and sparsity, numerical trials reveal that the choice of $j_l = 3$ provides the best results. In other words, the lowest factor matrix must contain all lowpass and bandpass filters in order to keep the precision.

Fig. 3.4 depicts the orthogonality of S by the matrix elements in $U = S^t S$, for $j_l = 0$ and $j_l = 3$ respectively (the highest level is fixed at $j_h = 6$). Ideally, U will be an identity matrix. And it is clearly observed that in the case of $j_l = 3$ the diagonal and off-diagonal elements cluster closer to 1 and 0, respectively, compared with the $j_l = 0$ case in the conventional SFWT. Data support can be found in Table 3.1 for RMS errors of U matrix elements in these two cases.

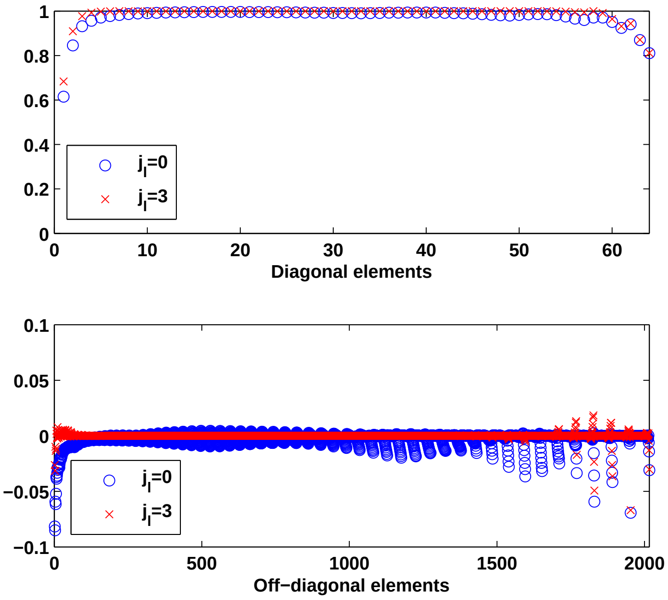

Figure 3.4: The Orthogonality Comparison between $j_l = 0$ and $j_l = 3$ for 1-D Total Transformation Matrix S. Diagonal and Off-Diagonal Elements of $U = S^t S$ Are Compared Separately. The Finest Level $j_h = 6$.

2-D case has a similar scheme while only one dimension is considered at each time. Assume a matrix with the size of $(M \times N)^2$, where the sampling points of N for the 1st dimension and the ones of M for the 2nd dimension should be integer powers of

Table 3.1: RMS Errors for Elements of $U = S^t S$ in 1-D SFWT ($j_h = 6$)

	RMS error $j_l = 0$ /%	RMS error $j_l = 3$ /%
Diagonal	6.305	5.163
Off-diagonal	0.8442	0.4248

2. The whole matrix can be divided into $N \times N$ submatrices with each submatrix containing $M \times M$ elements. Accordingly, the complete 2-D transformation matrix on j-th resolution level should follow the same submatrix profile. To be specific, each original element in (3.36) should be augmented to a $M \times M$ submatrix as the 1st dimension. Then the $M \times M$ 1-D transformation matrix of the 2nd dimension are lined up diagonally. The resulting 2-D transformation matrix on j-th resolution level is shown in Fig. 3.5. And the total 2-D transformation matrix can be derived from (3.37). Here j_h is chosen as $\min(\log_2 M, \log_2 N)$. In this matrix manner, the parallel computation can be easily implemented on the multiplication of a matrix and a vector.

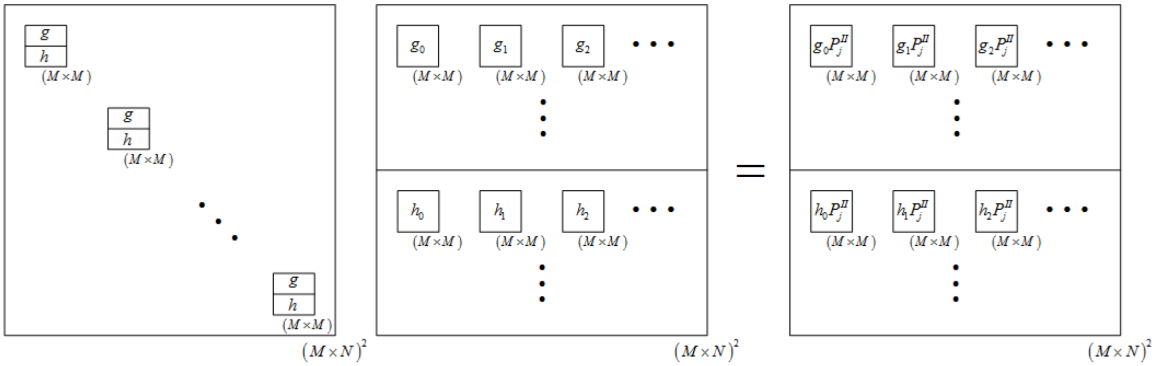

Figure 3.5: Transformation Matrix on j-th Level in 2-D SFWT.

3.2 Computational Complexity

The matrix generated from MFIE equations with finest scaling functions is converted to a sparse one by the SFWT under a certain threshold. Two typical examples, a circular cylinder with infinity length and a sphere, are discussed here for computational complexity of 1-D and 2-D SFWT, respectively. The iterative solver, e.g., conjugate gradient (Vorst, 1992), is employed in the sphere case to solve the resulting sparse matrix with the accuracy of 1×10^{-3}. And two types of computational complexity, fixed frequency and fixed discretization, are reported below.

3.2.1 Circular Cylinder

Fixed Frequency: The frequency is fixed at 300MHz and the discretization size is varying from $\lambda/20$ to $\lambda/163$. The memory consumption for non-zero entries after SFWT is $O(N^{1/5}\log N)$ in Fig. 3.6.

Fixed Discretization: The discretization of $\lambda/20$ is kept and the frequency is increasing from 300MHz to 2.4GHz. The memory is scaled as $O(N^{6/5}\log N)$ as ka goes up, as shown in Fig. 3.6.

3.2.2 Sphere

The PEC sphere with the diameter $D = 2$m is excited by a plane wave. The incident is into the North Pole with the E-field parallel to x-axis. And the scattered fields are collected on $\phi = 0^\circ$ plane. Originally, the coarsest level, j_l, in generating the total transformation matrix is selected to be 0 in (Pan *et al.*, 2014).

Fixed Frequency: The frequency is fixed at 300MHz and the discretization size is varying from $\lambda/5$ to $\lambda/82$. The number of unknowns is increasing subsequently with the matrix assembling time maintaining the complexity of $O(N)$, as shown in

Fig. 3.7(a). Here the matrix assembling time includes both matrix filling and solving time (see Table 3.2). Since this situation is analogous to electrical small problems and ka is constant, the memory consumption for non-zero entries after SFWT is $O(N^{1/10} \log N)$ in Fig. 3.7(b).

Fixed Discretization: The discretization of $\lambda/5$ is kept and the frequency is increasing from 300MHz to 4.8GHz. The memory requirement is scaled as $O(N^{6/5} \log N)$ as ka goes up. The reason is that SFWT, like other acceleration method, e.g., ACA, H2, etc., can only work for moderate sized problems. Hence the memory complexity could be as poor as $O(N^2)$ at the high frequency. Meanwhile, the matrix assembling time can still follow $O(N)$, since the One-Point property of the father wavelet is applied to all the off-diagonal elements. All the above is suggested in Fig. 3.7. But one should notice that the number of the off-diagonal elements scales as $O(N^2)$, which means they will have increasing effect on the calculation time. Hence, the matrix assembling time may gradually grow as $N \log N$. The detailed performance parameters, such as electric size, number of unknowns, matrix filling and solving time, number of iterations, sparsity indices, etc. are tabulated in Tables 3.2 and 3.3 below. The 4th row of Table II, $D = 16\lambda$, corresponds to the largest electric size solved by ACA (Zhao *et al.*, 2005). The last two rows are for $D = 24\lambda, 32\lambda$, respectively. While these two cases are solved by the Coiflet algorithm without any difficulties, we cannot perform the SFWT for matrix sparsification due to computer memory limitation. The 'NA' in the tables should read 'not available'.

Next, for better accuracy, the coarsest level j_l is selected to be 3 instead of 0, which may increase the non-zero entry memory after the sparsification (threshold $= 1 \times 10^{-3}$).

In order to quantitatively measure the additional memory consumption resulting from the accuracy improvement, the complexity of non-zero entry memory is numeri-

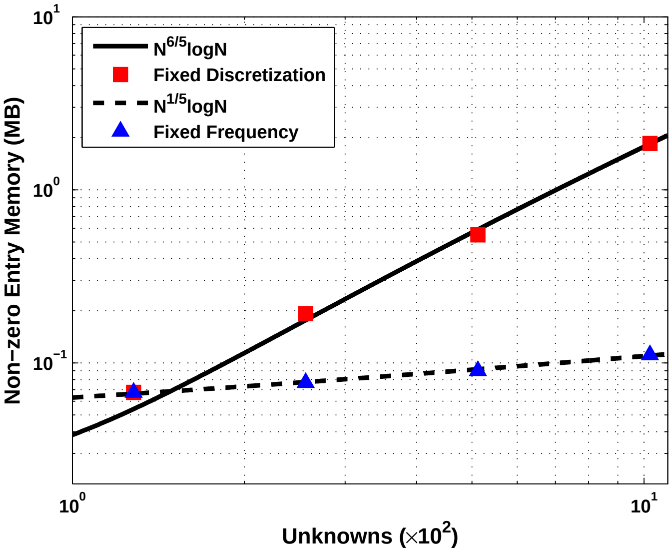

Figure 3.6: Memory Scaling of MFIE after SFWT (Threshold $= 1 \times 10^{-3}$) for a PEC Circular Cylinder with Infinity Length. The Plane Wave Is Employed as the Incident (TE Case). Two Experiments Are Performed: (1) Fixed Discretization and Increasing Frequency; (2) Fixed Frequency and Decreasing Discretization.

Table 3.2: Fixed Frequency

N	D	Matrix-Filling	Matrix-Solving		Nonzero-Entry
	/λ	/sec	/sec	Iter.	/GB
1024	2	2132	<1	12	0.008350581
4096	2	5748	1	12	0.012485981
16384	2	18979	3	12	0.016895831
65536	2	73752	92	12	0.022155613
147456	2	171278	434	12	NA
262144	2	387722	273	12	NA

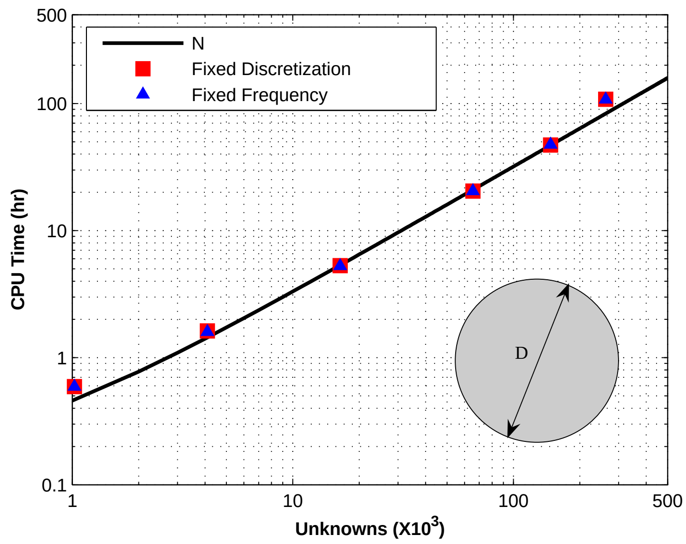

(a)

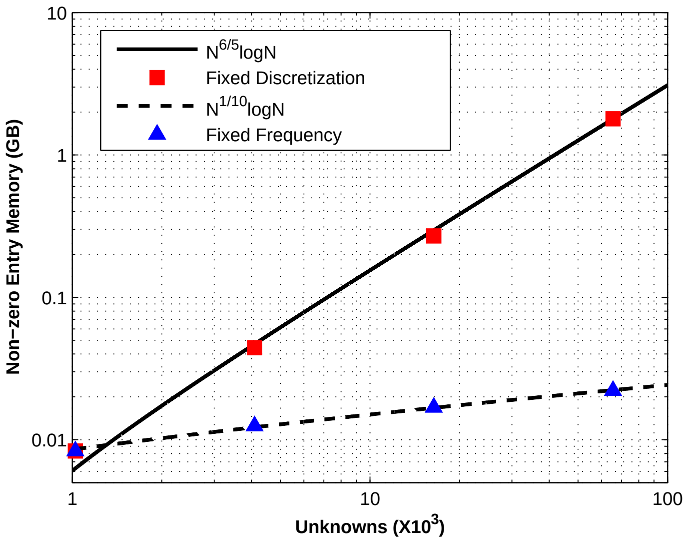

(b)

Figure 3.7: Complexity of MFIE with SFWT for a PEC Sphere: (a) Matrix Filling Time with MFIE, (b) Memory of Non-Zero Entries in SFWT Matrix (Threshold = 1×10^{-3}). Two Experiments Are Performed: (1) Fixed Discretization and Increasing Frequency; (2) Fixed Frequency and Decreasing Discretization.

Table 3.3: Fixed Discretization

N	D	Matrix-Filling	Matrix-Solving		Nonzero-Entry
	/λ	/sec	/sec	Iter.	/GB
1024	2	2132	<1	12	0.008350581
4096	4	5841	1	25	0.044291437
16384	8	19059	8	38	0.269784003
65536	16	73741	982	142	1.79526937
147456	24	169767	4880	140	NA
262144	32	388535	3672	166	NA

cally studied. We employ fixed discretization here to better explore the quantification. The fixed discretization case works on the electrically increasing large problem while the frequency goes up. In addition, based on the previous work (Pan *et al.*, 2014), the Coiflet based method is relatively stable in the fixed frequency case of the sphere example, since the electrical size is constant and better accuracy can be obtained by the employment of smaller discretization.

Table 3.4 lists non-zero entry memory data for $j_l = 3$ together with data for $j_l = 0$ in the previous work (Pan *et al.*, 2014). The discretization is fixed to $\lambda/5$ and the frequency is increasing from 300MHz to 2.4GHz. Numerical data indicates inconspicuous increase in memory consumption, leading to that the memory requirement can still be scaled as $O(N^{6/5}\log N)$ as shown in Fig. 3.8.

Fig. 3.9 compares relative errors of bistatic scattering coefficients between $j_l = 0$ and $j_l = 3$ cases. The sphere is discretized by 32 and 64 Coiflets in θ and ϕ directions respectively, rendering 4096 unknowns. Both Coiflet based results are with respect to FEKO data at 600MHz. It can be observed that, in the case of $j_l = 3$ relative errors cluster much closer to 0 than those in $j_l = 0$ case. In addition, the RMS of the above relative errors is 3.320×10^{-2} for $j_l = 3$, compared to 1.014×10^{-1} for $j_l = 0$. In other words, $j_l = 3$ can achieve higher accuracy than $j_l = 0$. Such improvement on accuracy can also be represented through RMS error comparisons for U matrix elements. Specifically, in $j_l = 3$ case the RMS errors for diagonal and off-diagonal elements are 7.579×10^{-2} and 9.103×10^{-4} respectively, while in $j_l = 0$ case the errors are 1.127×10^{-1} for the diagonal and 2.118×10^{-3} for the off-diagonal. Moreover, in Table 3.4, the memory consumption for non-zero entries in $j_l = 3$ case only increases by 0.85% of the total unknowns.

Table 3.4: Fixed Discretization: Non-Zero Entry Memory

N	D /λ	Non-zero $j_l = 0$ /GB (%)	Non-zero $j_l = 3$ /GB (%)
1024	2	0.0084 (26.72)	0.0093 (29.78)
4096	4	0.0443 (8.86)	0.0485 (9.71)
16384	8	0.2698 (3.37)	0.2794 (3.49)
65536	16	1.7953 (1.40)	1.8038 (1.41)

3.3 Accuracy

In this section, scattering coefficients resulting from four classic metallic models of circular cylinder, sphere, almond and ogive are selected to validate algorithm accuracy. The circular cylinder has infinity length and can be treated as a 2-D object. The rest examples are closed surfaces and they may introduce interior resonance. As is known, both EFIE and MFIE suffer from inner resonance problems. The combined field integral equation (CFIE), which is a combination of EFIE and MFIE with a certain combined coefficient, can overcome the inner resonance problem and reduce

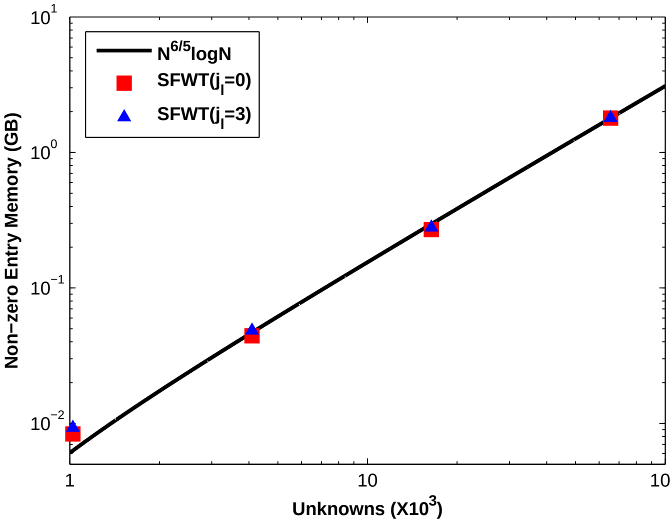

Figure 3.8: Memory Scaling of MFIE after SFWT (Threshold $= 1 \times 10^{-3}$) in a PEC Sphere Scattering Problem for the Fixed Discretization Case with the Increasing Frequency.

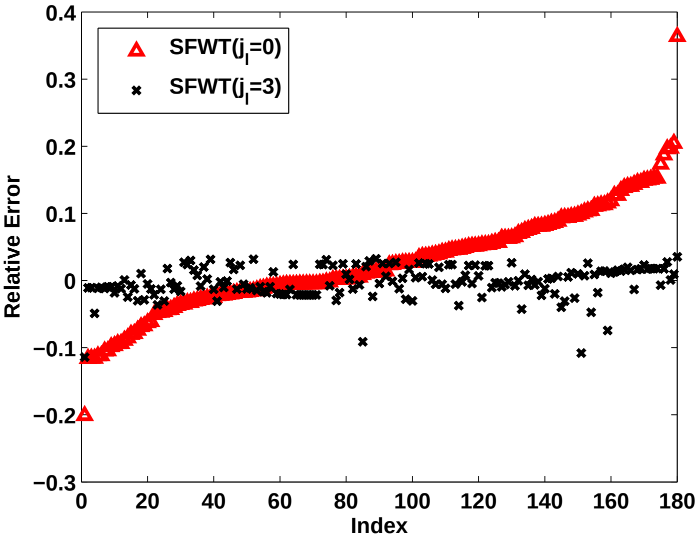

Figure 3.9: Relative Errors with Respect to FEKO Data for the Bistatic Scattering from a PEC Sphere at 600MHz ($\phi = 0°$ Cut). The Coarsest Levels of $j_l = 0$ and $j_l = 3$ Are Compared in Creating SFWT Transformation Matrix. The x-Axis Denotes the Indices of Sorted Observation Angles in θ.

the matrix condition number, improving the accuracy and accelerating the iteration speed. Fortunately, for the three closed-surface examples here, each operates below its 1st resonance point.

All matrices generated from MFIE equations with finest scaling functions are converted to sparse ones by SFWT with $j_l = 3$ maintained and a threshold. The iterative solver, e.g., bi-conjugate gradient (Vorst, 1992), is employed to solve the resulting sparse matrices. The accuracy performance is reported through the comparisons with analytical solutions for the cylinder and FEKO simulation results for the rest.

3.3.1 Circular Cylinder

The conducting circular cylinder is discretized only along the circle direction by the Coiflets with the discretization of $\Delta = \lambda/10$ (totally 64 sampling points), since the length is infinity. In Fig. 3.10, the excited surface current and bistatic scattering coefficients display good agreement with the analytical results, respectively. In the example mentioned in Fig. 3.3, the non-zero entries after SFWT count only 0.35% of the original impedance matrix, while the accuracy of the excited surface current and the bistatic scattering coefficients can still be well matched with the analytical results in Fig. 3.11, respectively.

3.3.2 Sphere

The PEC sphere, as shown in Fig.3.12, is discretized in the spherical coordinates by the Coiflets in both θ and ϕ directions with the discretization of $\Delta = \lambda/5$ and the number of 4096 unknowns. To accommodate the non-periodic nature, the intervallic scalets are employed in θ direction (Pan, 2003; Pan *et al.*, 1999). Since only Coifman scaling function is used, the original matrix is quite dense. Hence SFWT is applied

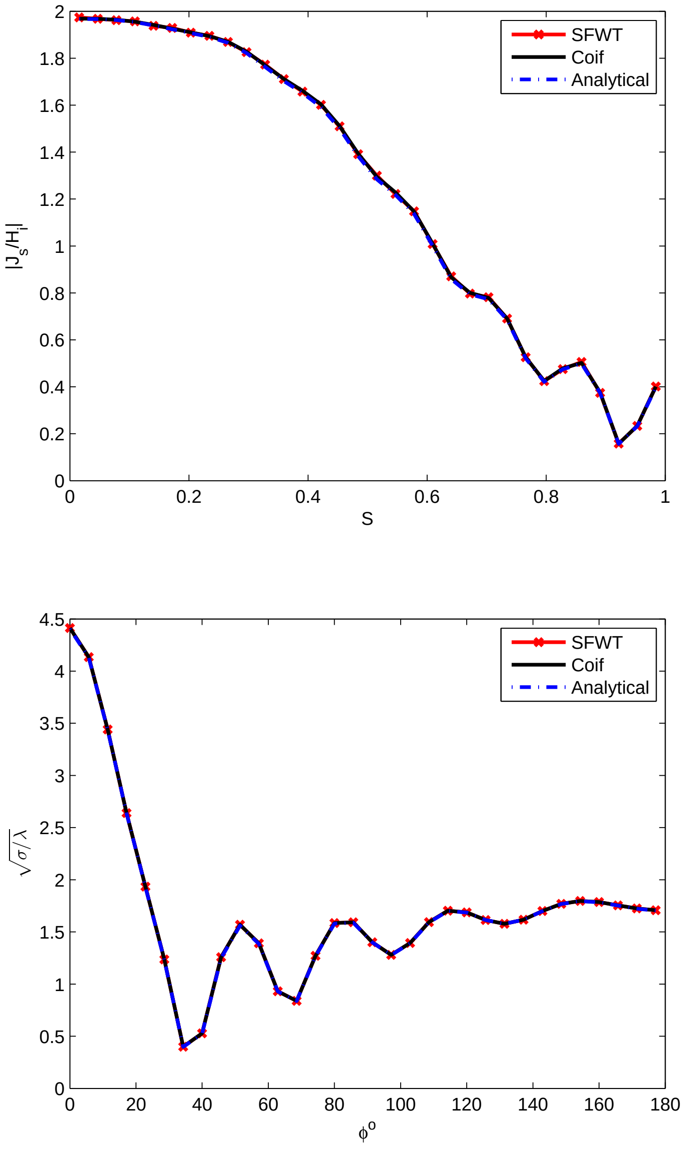

Figure 3.10: The Normalized Surface Current Density and the Normalized Scattering Coefficients for the Problem of a PEC Circular Cylinder Illuminated by a Plane Wave (300MHz, TE Case). There Are 64 Sampling Points along the Entire Circle. Simulation Results of SFWT, Standard Coiflets and Analytical Method Are Compared.

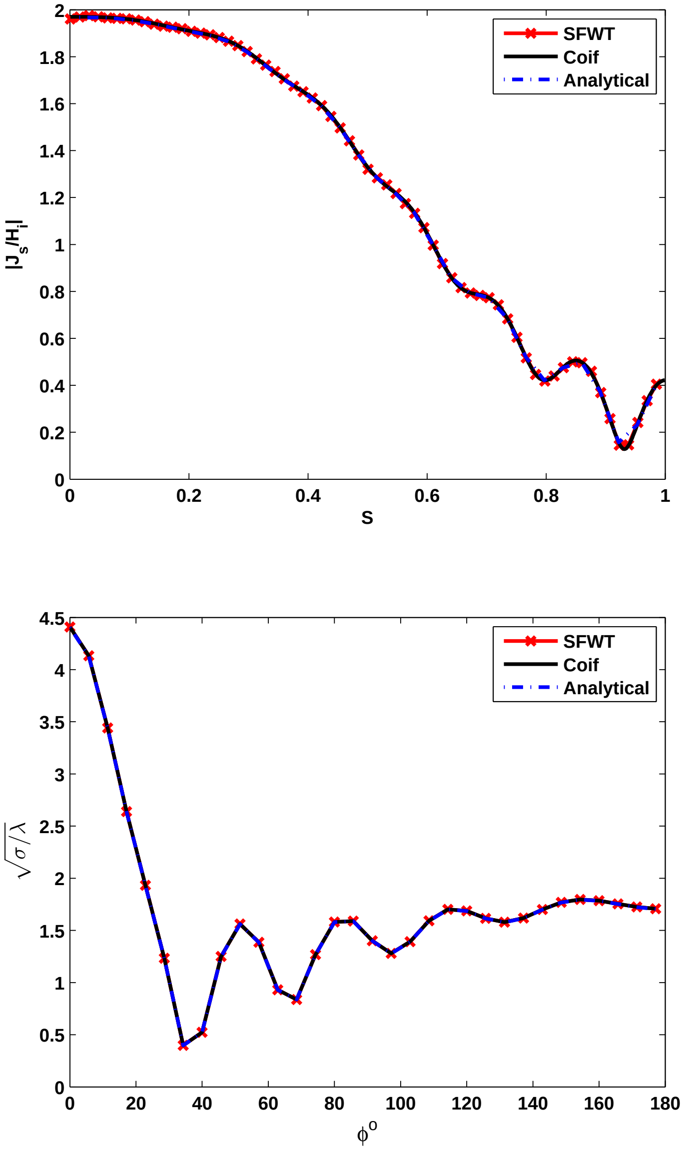

Figure 3.11: The Normalized Surface Current Density and the Normalized Scattering Coefficients for the Problem of a PEC Circular Cylinder Illuminated by a Plane Wave (300MHz, TE Case). There Are 1024 Sampling Points along the Entire Circle. Simulation Results of SFWT, Standard Coiflets and Analytical Method Are Compared.

to compress the storage and improve the efficiency.

In Fig. 3.14, the bistatic scattering coefficients of the sphere at 600MHz. The MFIE result can match that of FEKO, while FEKO needs 15015 unknowns (10010 triangle meshes) with the suggested mesh triangle edge length of $\lambda/8$. And it can still fit the precision with only 9.71% matrix elements left after SFWT of threshold $= 1 \times 10^{-3}$ involved. The resulting impedance matrix is shown in Fig 3.13.

Similarly, Fig. 3.16 depicts the bistatic scattering from the sphere at 300MHz with 2.5% matrix elements left in Fig. 3.15 after SFWT sparsification. Based on the study in the previous section, the matrix can be dramatically compressed by involving SFWT, e.g. 1.41% of the original matrix elements for the smooth surface of $800\lambda^2$, while the precision can still be preserved.

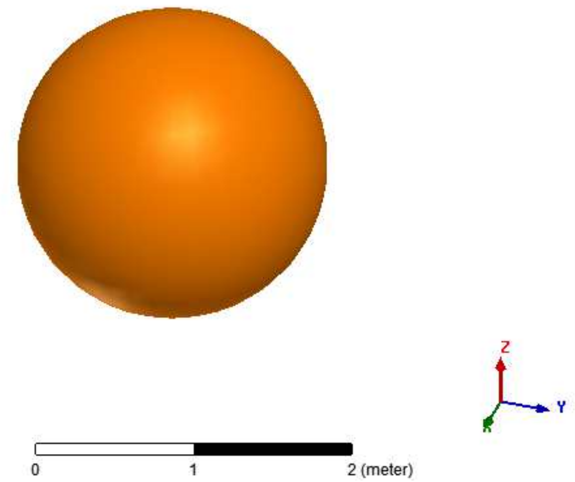

Figure 3.12: Sphere Configuration

3.3.3 Almond

The almond (Woo *et al.*, 93), as shown in Fig.3.17, is employed as the benchmark for algorithm verification. Fig.3.18 and 3.19 depict the monostatic scattering from

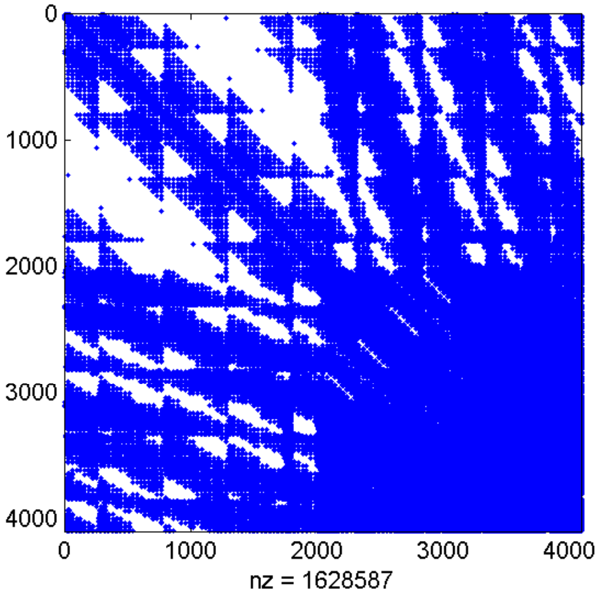

Figure 3.13: Impedance Matrix of SFWT (Threshold $= 1 \times 10^{-3}$) for a PEC Sphere at 600MHz.

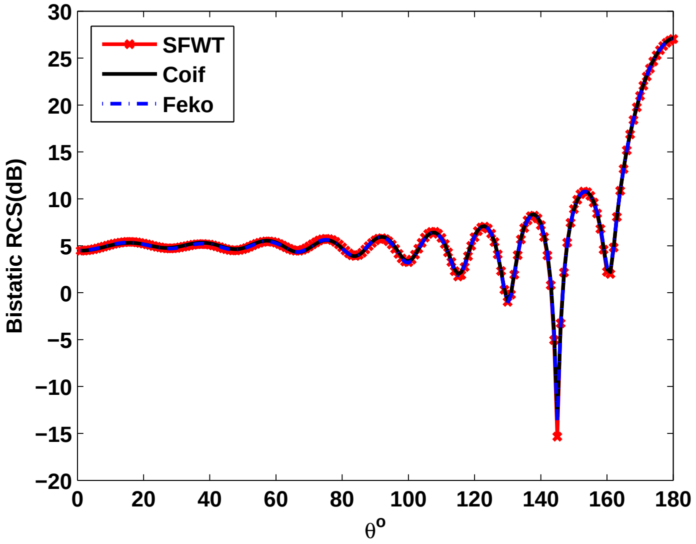

Figure 3.14: Bistatic Scattering of a PEC Sphere at 600MHz ($\phi = 0°$ Cut). The Incident Plane Wave Is into the North Pole with the E-Field Parallel to x-Axis. Simulation Results of SFWT (Threshold $= 1 \times 10^{-3}$), Standard Coiflets Method and FEKO Are Compared.

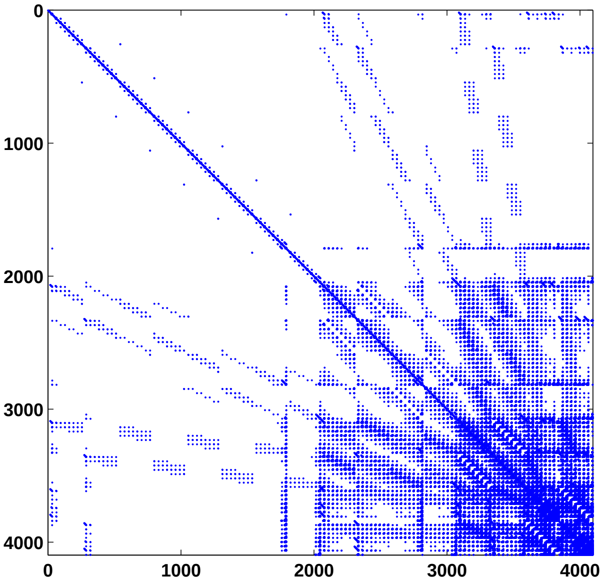

Figure 3.15: Impedance Matrix of SFWT (Threshold = 1×10^{-3}) for a PEC Sphere at 300MHz.

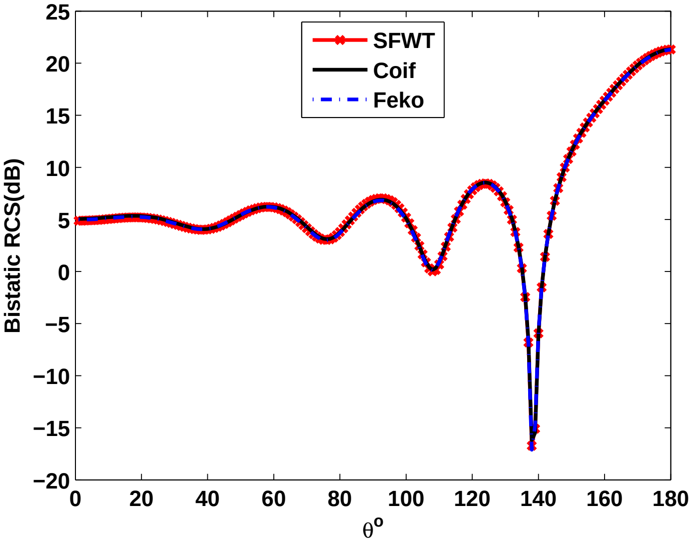

Figure 3.16: Bistatic Scattering of a PEC Sphere at 300MHz ($\phi = 0°$ Cut). The Incident Plane Wave Is into the North Pole with the E-Field Parallel to x-Axis. Simulation Results of SFWT (Threshold = 1×10^{-3}), Standard Coiflets and FEKO Are Compared.

the metallic almond at 1.19GHz and 7GHz, respectively. 'HH' and 'VV' are labeled for backscattering from horizontal and vertical polarization, respectively.

Especially for the case of horizontal polarization, the surface currents on the high curvature 'edges' are extremely sensitive. In the 7GHz case, the bi-conjugate method converges at 51st iteration by 9.911×10^{-4} (criterion $= 1 \times 10^{-3}$). It is shown that numerical results of SFWT with 8192 unknowns (threshold $= 1 \times 10^{-4}$) display agreement with those of standard Coiflets method and FEKO simulation with 11568 unknowns (7712 triangle meshes), while the non-zero matrix entries are 5.11% of the standard method. Fig.3.20 compares simulation results of similar dense sampling points among SFWT, standard Coiflets and FEKO. Specifically, both SFWT and standard Coiflet methods have 32768 unknowns, while FEKO has 32775 unknowns (21850 triangle meshes). Measured data in literature is also provided.

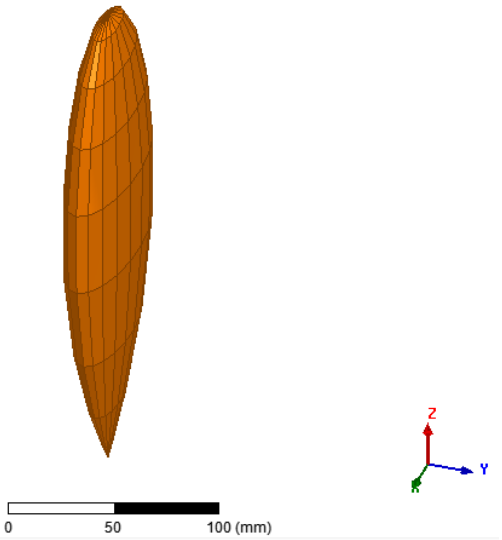

Figure 3.17: Almond Configuration

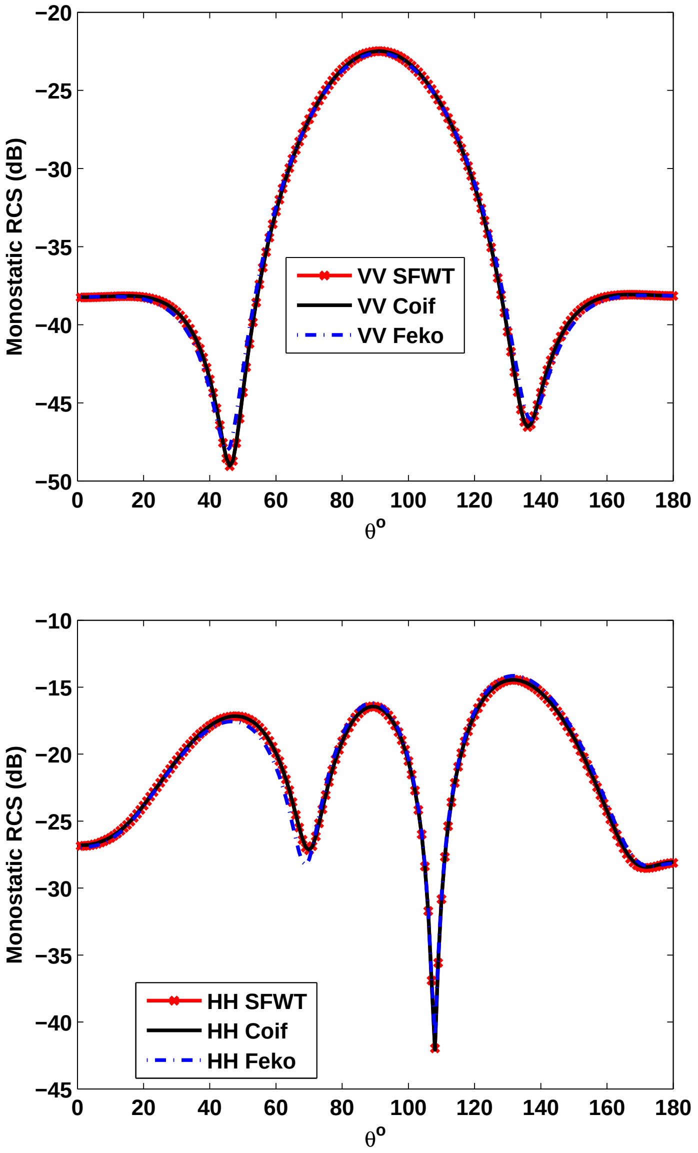

Figure 3.18: Monostatic Scattering from the NASA Almond at 1.19GHz. Simulation Results of SFWT, Standard Coiflets and FEKO Are Compared.

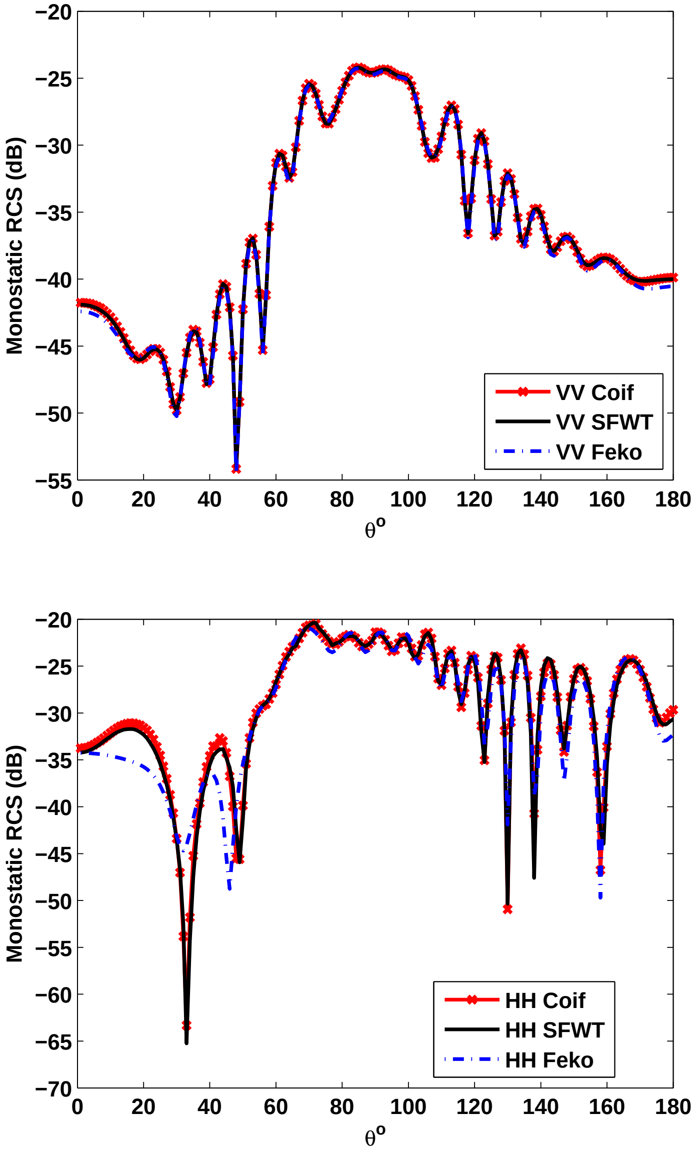

Figure 3.19: Monostatic Scattering from the NASA Almond at 7GHz. Simulation Results of SFWT, Standard Coiflets and FEKO Are Compared.

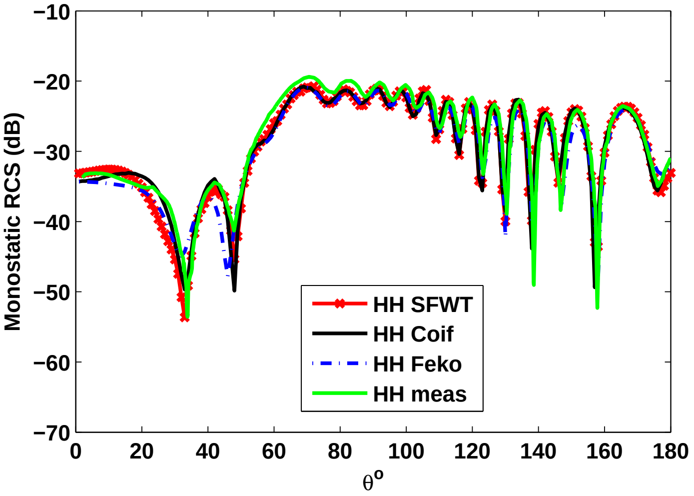

Figure 3.20: Monostatic Scattering from the NASA Almond at 7GHz. Simulation Results with Similar Dense Sampling Points Are Compared among SFWT, Standard Coiflets and FEKO. Measured Data in Literature Is Also Provided.

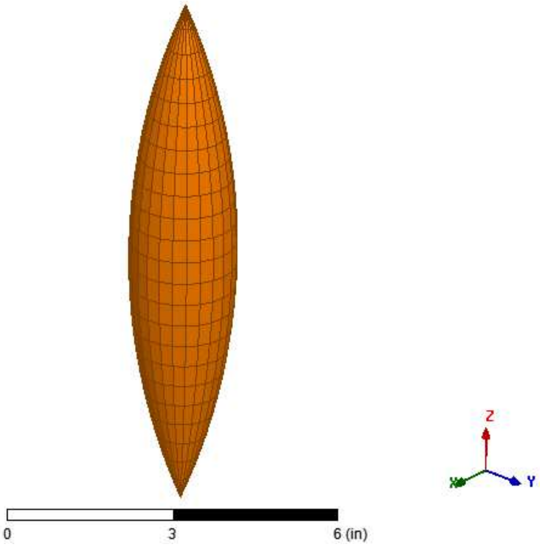

Figure 3.21: Ogive Configuration

3.3.4 Ogive

The ogival body (Woo *et al.*, 93), as shown in Fig.3.21, is a classical RCS test case. In Fig.3.22, the monostatic scattering from the metallic ogive at 1.18GHz is displayed for both horizontal and vertical co-polarizations. Similar to the almond case, simulation results of SFWT, standard Coiflets (2048 unknowns) and FEKO (2067 unknowns or 1378 triangle meshes) are compared. The bi-conjugate method in SFWT converges at 11st iteration by 9.932×10^{-4} (criterion $= 1 \times 10^{-3}$).

The problems above have explicit geometric expressions. For more complex structures, readers are referred to a more general algorithm, which uses arbitrary 3-D meshes under the EFIE with triangular cells in conjunction with hierarchical bases for the preconditioning (Vipianaa *et al.*, 2009).

3.4 Random Rough Surfaces

The PEC rough surface under investigation here has a profile defined by Gaussian probability density function and Gaussian correlation function. The tapered wave (Braunisch *et al.*, 2000) is applied to the truncated surface as the horizontal incidence, to resemble the plane wave near the scattering center and decay rapidly to negligibly weak before reaching the surface edge. The scattering configuration and an example rough surface profile can be seen in Fig. 3.23. Since it has been proved that the discretization $\Delta = \lambda/4$ is sufficient for the scattering problems of random PEC rough surface (Pan *et al.*, 2004), we will use this rule of thumb for all problems in this section.

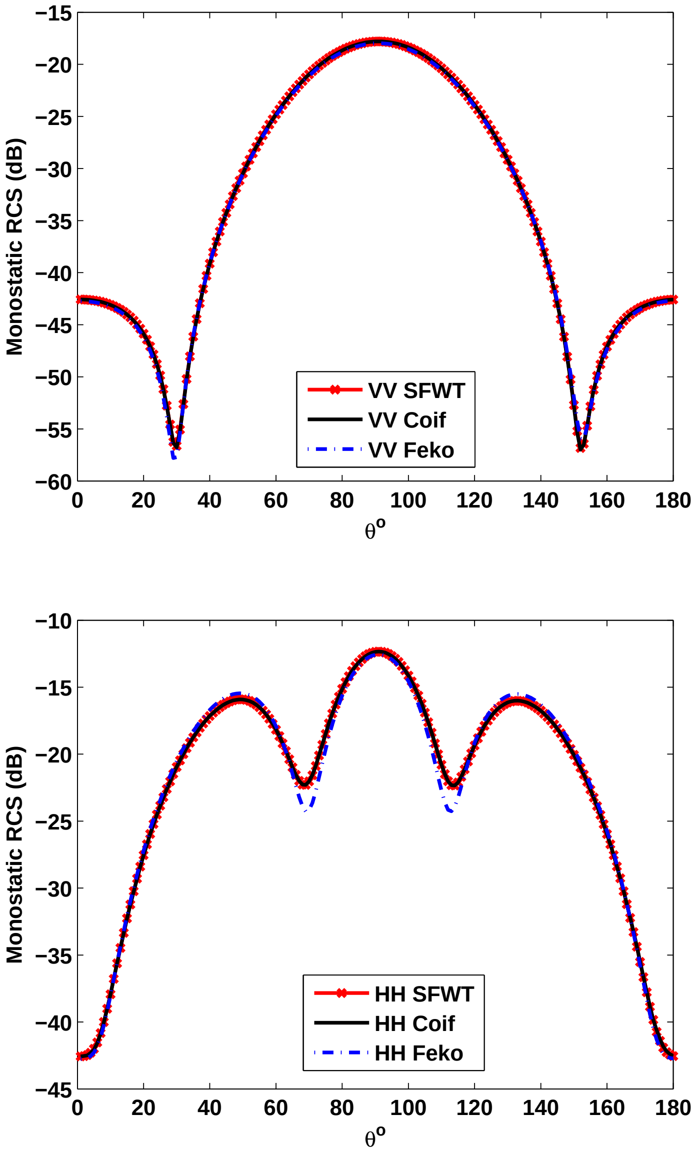

Figure 3.22: Monostatic Scattering from the Metallic Ogive at 1.18GHz. Simulation Results of SFWT, Standard Coiflets and FEKO Are Compared.

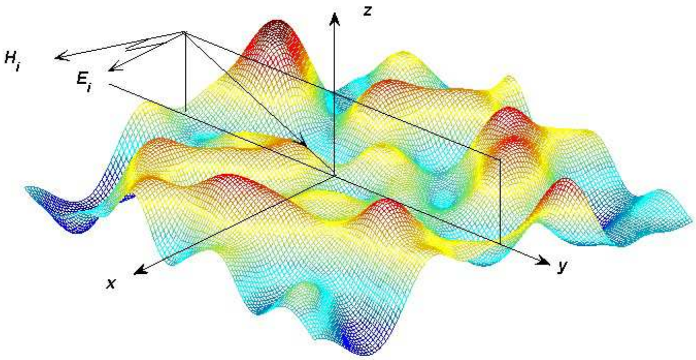

Figure 3.23: Configuration of 3-D Scattering from an Example Rough Surface Profile.

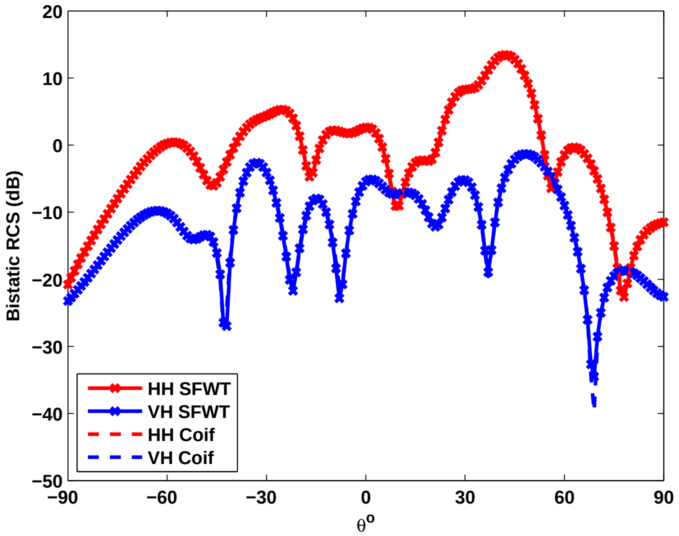

Figure 3.24: Bistatic Scattering Coefficients from One Realization of the $8\lambda \times 8\lambda$ PEC Rough Surface ($\sigma = 0.2\lambda, l_x = l_y = 0.6\lambda$). The Incident Tapered Wave Is at $\theta_i = -40^\circ$ and $\phi_i = 90^\circ$ (Horizontal Polarization). Simulation Results of SFWT and Standard Coiflets Method Are Compared.

3.4.1 Surface with Intermediate Roughness

Fig. 3.24 depicts the bistatic scattering coefficients from one surface realization with intermediate roughness (standard deviation $\sigma = 0.2\lambda$ and correlation length $l_x = l_y = 0.6\lambda$ on the truncated size of $8\lambda \times 8\lambda$). And horizontal incidence is selected as $\theta_i = -40^\circ$ and $\phi_i = 90^\circ$. Here, horizontal incident and horizontal scattering are referred to as the HH polarization, while VH is for horizontal incident and vertical scattering. A SFWT threshold of 1×10^{-3} is applied and the convergence of the bi-conjugate method has been achieved within 7 iterations at 9.617×10^{-4} (criterion $= 1 \times 10^{-3}$). It can be observed that the far field results have good agreement between the standard Coiflets method and the one sparsified by SFWT.

3.4.2 Very Rough Surface

Fig. 3.25 illustrates the bistatic scattering coefficients from one realization of the very rough surface with the following parameters: standard deviation $\sigma = 1.0\lambda$, correlation length $l_x = l_y = 2.0\lambda$, the truncated surface size $16\lambda \times 16\lambda$. The tapered incident is specified as $\theta_i = -20^\circ$ and $\phi_i = 90^\circ$.

The averaged scattering coefficients generated from the original Coiflets based numerical method, as shown in Fig. 3.26, have been demonstrated to have good agreement versus experimental data (Pan *et al.*, 2004). Fig. 3.25 shows that for a single realization, Coiflets based numerical results after SFWT can still well preserve the accuracy, compared with the original results of the Coiflets method.

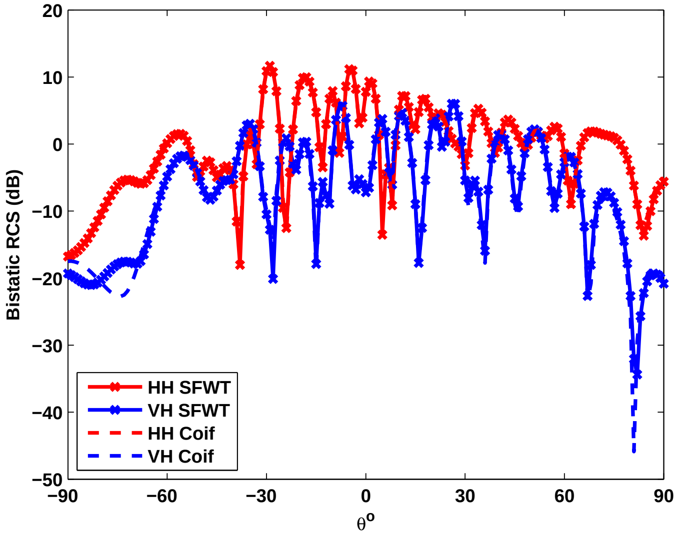

Figure 3.25: Bistatic Scattering Coefficients from One Realization of the $16\lambda \times 16\lambda$ PEC Rough Surface ($\sigma = 1.0\lambda, l_x = l_y = 2.0\lambda$). The Incident Tapered Wave Is at $\theta_i = -20°$ and $\phi_i = 90°$ (Horizontal Polarization). Simulation Results of SFWT and Standard Coiflets Method Are Compared.

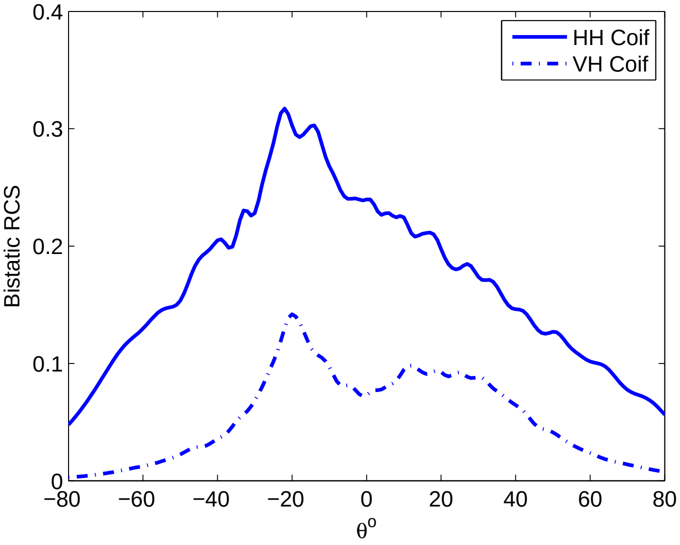

Figure 3.26: Average Bistatic Co-Polarized and Cross-Polarized RCS from 576 Realizations of the $16\lambda \times 16\lambda$ PEC Rough Surface ($\sigma = 1.0\lambda, l_x = l_y = 2.0\lambda$). The Incident Tapered Wave Is at $\theta_i = -20°$ and $\phi_i = 90°$ (Horizontal Polarization).

Chapter 4

ON UNIFIED NUMERICAL ALGORITHM FOR 3-D SCATTERING FROM PEC AND DIELECTRIC RANDOM ROUGH SURFACES

Scattering of electromagnetic waves from rough surfaces has been applied to microwave remote sensing. Both analytical models and numerical methods have been extensively studied during the past decades. The highly robust analytical models of Kirchhoff approximation (KA) and small perturbation method (SPM) are generally used within their limited domains of validity (Fung, 1994). Attempts were made to combine the two analytical models, resulting the two-scale model (Ulaby *et al.*, 1982). Extending the two-scale to multi-scale, the iterated Kirchhoff of PEC (Fung and Pan, 1987) was derived, which reduces to the KA solution in the high-frequency region and SPM solution in the low-frequency region, respectively. Using the same approach and assumptions of (Fung and Pan, 1987), a model of iterated Kirchhoff for dielectric surfaces was developed (Fung *et al.*, 1992), and has been widely used in remote sensing. Other extended analytical models include Kirchhoff with shadowing (Ishimaru *et al.*, 1996) and Wiener-Hermite (WH) expansion (Eftimiu, 1988; Eftimiu and Pan, 1990; Eftimiu, 1989), among others.

Compared to analytical methods, numerical algorithms have higher flexibility for the real-world applications. The most common numerical approach is the integral equation (IE) method discretized by the MoM. From mathematical point of view, there are two basic integral equation formulations, namely, the Fredholm IE of 1st kind, or electric field integral equation (EFIE) and the Fredholm IE of 2nd kind, or magnetic field integral equation (MFIE). Maxwell's equations and the surface boundary conditions can be reduced to a single equivalent surface integral equation when the surface is a perfect conductor, while in the case of a dielectric interface the coupled pair of surface integral equations need to be employed (Warnick and Chew, 2001). In the later case, the normal components of Maxwell's equations on the surface, as the original unknowns, yield relationships with the surface derivatives of the surface currents and thus can be replaced. Though the number of unknowns is reduced, the price has to be paid for involving the surface derivatives of the surface currents in the integrand. However, rough surface scattering problems are electrically large, and thus the discretization of the corresponding surface integral equations can result in a large dense matrix whose filling time dominants the computational cost. Specifically, traditional MoM requires the computation time of $O(N^2)$ for matrix fill and $O(N^3)$ for matrix inversion, where N is the total number of unknowns. Consequently, several advanced algorithms have been proposed in combination with iterative solvers and fast methods. Based on the AIM (Bleszynski *et al.*, 1993, 1996), the sparse matrix/canonical grid (SM/CG) method (Pak *et al.*, 1997) has employed the planar RWG basis with the series Taylor expansion and accelerated matrix-vector multiplications with fast Fourier transforms (FFT) in the iterative solver. And to further cut down the number of unknowns and efficiently increase the flexibility, the curvilinear RWG basis and the Chebyshev interpolating Green's function have been applied instead (Huang *et al.*, 2009; Huang and Tsang, 2012). The forward-backward (FB) method (Holliday *et al.*, 1996; Iodice, 2002) has been employed for 1-D surfaces with a modified fast multipole method (FMM) (Torrungrueng *et al.*, 1998) or spectral acceleration (SA) (Liu *et al.*, 2011; Brennan *et al.*, 2013).

Wavelets have been successfully used to efficiently solve integral equations related to 3-D scattering and emissivity problems (Pan *et al.*, 2014; Wang and Pan, 2013; Jin *et al.*, 2016). Particularly, wavelets has been applied together with the iterative technique, e.g. bi-conjugate gradient stabilized method (Bi-CGSTAB) (Vorst, 1992;

Huang *et al.*, 2014) for random rough surface (Tretiakov *et al.*, 2004; Pan *et al.*, 2004). Tapered waves (Braunisch *et al.*, 2000) are used in rough surface scattering to truncate the computational domain. In (Pan *et al.*, 2004), the tapered wave was imposed as the incident beam to emulate certain problems in which the footprint of the beam is smaller than the target, preventing the edge diffraction. Owing to concentrated energy in spatial/spectral domain and vanishing moments, the implementation of wavelets as the basis and testing functions produces a sparse impedance matrix and exhibits fast convergence. Further, the Dirac-δ like property of Coiflets (Pan, 2003) permits fast calculation of the most off-diagonal entries in the impedance matrix, imposing the one-point quadrature formula and dramatically reducing the computational efforts in filling matrix from $O(N^2)$ to $O(N)$.

In this chapter, the coupled Fredholm integral equations of the 2nd kind are solved by the Coiflet based MoM for unknown tangential and normal components of surface fields on a 3-D dielectric interface. As a system of the Fredholm of the 2nd kind, it is well-posed. Numerical results are outlined, including method validation and modeling examples.

4.1 Formulation

4.1.1 Vector and Scalar Integral Equations

Fig. 4.1 sketches the configuration of 3-D scattering. The standard surface integral equations (Poggio and Miller, 1973; Li and Fung, 1991; Hsieh and Fung, 2003; Fung *et al.*, 1992) are defined in normalized field quantities with $\sqrt{\varepsilon}\vec{E} = \vec{e}$ and $\sqrt{\mu}\vec{H} = \vec{h}$

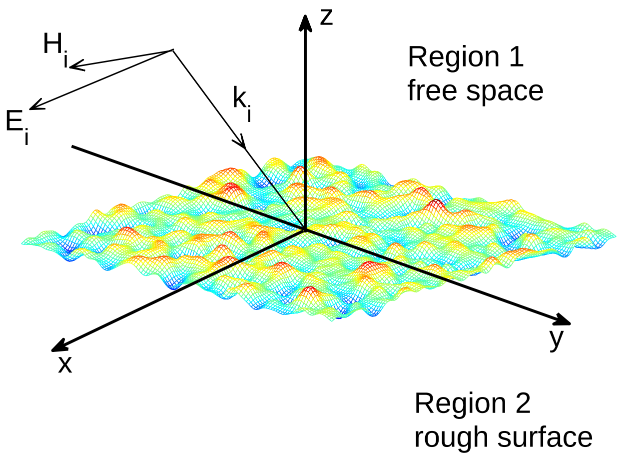

Figure 4.1: Configuration of 3-D Scattering from Random Rough Surface (Horizontal Incident Case).

(Ogurtsov and Pan, 2008)

$$
\begin{aligned}
\vec{n}_1 \times \vec{h}^i &= \frac{\vec{n}_1 \times \vec{h}_1}{2} - \vec{n}_1 \times \int \vec{\mathcal{H}}_1 ds' \\
0 &= \frac{\vec{n}_1 \cdot \vec{h}_1}{2} - \vec{n}_1 \cdot \int \vec{\mathcal{H}}_2 ds' \\
0 &= \frac{\vec{n}_1 \times \vec{e}_1}{2} + \vec{n}_1 \times \int \vec{\mathcal{E}}_2 ds' \\
\vec{n}_1 \cdot \vec{e}^i &= \frac{\vec{n}_1 \cdot \vec{e}_1}{2} + \vec{n}_1 \cdot \int \vec{\mathcal{E}}_1 ds'
\end{aligned}
\tag{4.1}
$$

where

$$
\begin{aligned}
\vec{\mathcal{E}}_1 &= jk_1(\hat{n}_1' \times \vec{h}_1)g_1 - (\hat{n}_1' \times \vec{e}_1) \times \nabla' g_1 - (\hat{n}_1' \cdot \vec{e}_1)\nabla' g_1 \\
\vec{\mathcal{H}}_1 &= jk_1(\hat{n}_1' \times \vec{e}_1)g_1 + (\hat{n}_1' \times \vec{h}_1) \times \nabla' g_1 + (\hat{n}_1' \cdot \vec{h}_1)\nabla' g_1 \\
\vec{\mathcal{E}}_2 &= -jk_1(\hat{n}_1' \times \vec{h}_1)g_2 + (\hat{n}_1' \times \vec{e}_1) \times \nabla' g_2 + \frac{\varepsilon_1}{\varepsilon_2}(\hat{n}_1' \cdot \vec{e}_1)\nabla' g_2 \\
\vec{\mathcal{H}}_2 &= -jk_1\frac{\varepsilon_2}{\varepsilon_1}(\hat{n}_1' \times \vec{e}_1)g_2 - (\hat{n}_1' \times \vec{h}_1) \times \nabla' g_2 - \frac{\mu_1}{\mu_2}(\hat{n}_1' \cdot \vec{h}_1)\nabla' g_2.
\end{aligned}
\tag{4.2}
$$

$\vec{n}_1$, $\vec{n}_1'$ are the surface normals in Region 1

$$
\begin{aligned}
\vec{n}_1 &= \sqrt{1 + f_x^2 + f_y^2}\,\hat{n}_1, \\
f_x &= \frac{\partial f(x,y)}{\partial x}, f_y = \frac{\partial f(x,y)}{\partial y}
\end{aligned}
\tag{4.3}
$$

$f(x, y)$ is the profile of rough surface.

g_1, g_2 are the Green's functions in Region 1 and Region 2, and $\nabla' g_1$, $\nabla' g_2$ represent the gradients of the Green's functions

$$\begin{aligned} & g_{1,2} = \frac{e^{-jk_{1,2}R}}{4\pi R}, \nabla g'_{1,2} = \frac{(1 + jk_{1,2}R)e^{-jk_{1,2}R}}{4\pi R^3}\vec{R}, \\ & R = \sqrt{(x - x')^2 + (y - y')^2 + (f - f')^2}. \end{aligned} \tag{4.4}$$

The scalar form of (4.1) can be derived in terms of x, y and n components, with the following six unknowns

$$\begin{cases} F_x(\vec{r}) = \vec{n}_1 \times \vec{h}(\vec{r}) \cdot \hat{x} \\ F_y(\vec{r}) = \vec{n}_1 \times \vec{h}(\vec{r}) \cdot \hat{y} \\ F_n(\vec{r}) = \vec{n}_1 \cdot \vec{h}(\vec{r}) \\ I_x(\vec{r}) = \vec{n}_1 \times \vec{e}(\vec{r}) \cdot \hat{x} \\ I_y(\vec{r}) = \vec{n}_1 \times \vec{e}(\vec{r}) \cdot \hat{y} \\ I_n(\vec{r}) = \vec{n}_1 \cdot \vec{e}(\vec{r}). \end{cases} \tag{4.5}$$

4.2 Expansion and Test with Coifman Scalets

The Galerkin procedure is conducted to discretize the scalar integral equations. We first expand (4.5) with Coifman scaling functions, and arrive at

$$\begin{cases} F_x(\vec{r}) = \sum_i \sum_j a_{ij} \varphi_{j_0,i}(x) \varphi_{j_0,j}(y) \\ F_y(\vec{r}) = \sum_i \sum_j b_{ij} \varphi_{j_0,i}(x) \varphi_{j_0,j}(y) \\ F_n(\vec{r}) = \sum_i \sum_j c_{ij} \varphi_{j_0,i}(x) \varphi_{j_0,j}(y) \\ I_x(\vec{r}) = \sum_i \sum_j d_{ij} \varphi_{j_0,i}(x) \varphi_{j_0,j}(y) \\ I_y(\vec{r}) = \sum_i \sum_j e_{ij} \varphi_{j_0,i}(x) \varphi_{j_0,j}(y) \\ I_n(\vec{r}) = \sum_i \sum_j f_{ij} \varphi_{j_0,i}(x) \varphi_{j_0,j}(y). \end{cases} \tag{4.6}$$

After substituting (4.6) into the scalar formulation, we conduct testing process by multiplying $\varphi_{j_0,m}(x)\varphi_{j_0,n}(y)$ to both sides of the integral functions and executing integration. Then the orthogonality and the one-point quadrature are taken to discretize the scalar integral equations as the matrix form (except diagonal entries), yielding

$$\left(\frac{\gamma^2}{2}\mathbf{I} + \mathrm{Z}\right)\mathrm{X} = \mathbf{b} \tag{4.7}$$

$$\mathrm{Z} = \begin{bmatrix} A_a & A_b & A_c & A_d & A_e & A_f \\ B_a & B_b & B_c & B_d & B_e & B_f \\ C_a & C_b & C_c & C_d & C_e & C_f \\ D_a & D_b & D_c & D_d & D_e & D_f \\ E_a & E_b & E_c & E_d & E_e & E_f \\ F_a & F_b & F_c & F_d & F_e & F_f \end{bmatrix} \tag{4.8}$$

$$\mathrm{X} = \begin{bmatrix} a_{mn} \\ b_{mn} \\ c_{mn} \\ d_{mn} \\ e_{mn} \\ f_{mn} \end{bmatrix} \mathbf{b} = \begin{bmatrix} h_{mn} \\ k_{mn} \\ 0 \\ 0 \\ 0 \\ l_{mn} \end{bmatrix} \tag{4.9}$$

where

$$\begin{aligned} &\gamma = 2^{j_0},\ G_{1,2} = \frac{(-1 - jk_{1,2}R)e^{-jk_{1,2}R}}{4\pi R^3}, \\ &R = \sqrt{(x_m - x_i)^2 + (y_n - y_j)^2 + (f_{mn} - f_{ij})^2}, \\ &f_{mn} = f(x_m, y_n),\ f_{ij} = f(x_i, y_j) \end{aligned} \tag{4.10}$$

and

$$
\begin{aligned}
h_{mn} &= \gamma \left[-\frac{\partial f_{mn}}{\partial y} h_{iz} - h_{iy} \right] \\
k_{mn} &= \gamma \left[\frac{\partial f_{mn}}{\partial x} h_{iz} + h_{ix} \right] \\
l_{mn} &= \gamma \left[-\frac{\partial f_{mn}}{\partial x} e_{ix} - \frac{\partial f_{mn}}{\partial y} e_{iy} + e_{iz} \right]
\end{aligned}
\tag{4.11}
$$

$$
\begin{cases}
A_a = G_1 \left[(y_n - y_j) \dfrac{\partial f_{mn}}{\partial y} + (x_m - x_i) \dfrac{\partial f_{ij}}{\partial x} \right. \\
\qquad\qquad\qquad\qquad\qquad\qquad \left. -(f_{mn} - f_{ij}) \right] \\
A_b = G_1 \left[\left(-\dfrac{\partial f_{mn}}{\partial y} + \dfrac{\partial f_{ij}}{\partial y} \right) (x_m - x_i) \right] \\
A_c = G_1 \left[\dfrac{\partial f_{mn}}{\partial y} (f_{mn} - f_{ij}) + (y_n - y_j) \right] \\
A_d = jk_1 g_1 \left[\dfrac{\partial f_{mn}}{\partial y} \dfrac{\partial f_{ij}}{\partial x} \right] \\
A_e = jk_1 g_1 \left[1 + \dfrac{\partial f_{mn}}{\partial y} \dfrac{\partial f_{ij}}{\partial y} \right] \\
A_f = 0
\end{cases}
\tag{4.12}
$$

$$
\begin{cases}
B_a = G_1 \left[\left(-\dfrac{\partial f_{mn}}{\partial x} + \dfrac{\partial f_{ij}}{\partial x} \right) (y_n - y_j) \right] \\
B_b = G_1 \left[(x_m - x_i) \dfrac{\partial f_{mn}}{\partial x} + (y_n - y_j) \dfrac{\partial f_{ij}}{\partial y} \right. \\
\qquad\qquad\qquad\qquad\qquad\qquad \left. -(f_{mn} - f_{ij}) \right] \\
B_c = G_1 \left[-\dfrac{\partial f_{mn}}{\partial x} (f_{mn} - f_{ij}) - (x_m - x_i) \right] \\
B_d = jk_1 g_1 \left[-1 - \dfrac{\partial f_{mn}}{\partial x} \dfrac{\partial f_{ij}}{\partial x} \right] \\
B_e = jk_1 g_1 \left[-\dfrac{\partial f_{mn}}{\partial x} \dfrac{\partial f_{ij}}{\partial y} \right] \\
B_f = 0
\end{cases}
\tag{4.13}
$$

$$\begin{cases} C_a = -G_2\left[\left(-1-\dfrac{\partial f_{mn}}{\partial x}\dfrac{\partial f_{ij}}{\partial x}\right)(y_n-y_j)\right. \\ \qquad \left. +\dfrac{\partial f_{mn}}{\partial y}(x_m-x_i)\dfrac{\partial f_{ij}}{\partial x}-\dfrac{\partial f_{mn}}{\partial y}(f_{mn}-f_{ij})\right] \\ C_b = -G_2\left[\left(1+\dfrac{\partial f_{mn}}{\partial y}\dfrac{\partial f_{ij}}{\partial y}\right)(x_m-x_i)\right. \\ \qquad \left. -(y_n-y_j)\dfrac{\partial f_{mn}}{\partial x}\dfrac{\partial f_{ij}}{\partial y}+\dfrac{\partial f_{mn}}{\partial x}(f_{mn}-f_{ij})\right] \\ C_c = -\dfrac{\mu_1}{\mu_2}G_2\left[\dfrac{\partial f_{mn}}{\partial x}(x_m-x_i)\right. \\ \qquad \left. +\dfrac{\partial f_{mn}}{\partial y}(y_n-y_j)-(f_{mn}-f_{ij})\right] \\ C_d = -jk_1\dfrac{\varepsilon_2}{\varepsilon_1}g_2\left[\dfrac{\partial f_{mn}}{\partial x}-\dfrac{\partial f_{ij}}{\partial x}\right] \\ C_e = -jk_1\dfrac{\varepsilon_2}{\varepsilon_1}g_2\left[\dfrac{\partial f_{mn}}{\partial y}-\dfrac{\partial f_{ij}}{\partial y}\right] \\ C_f = 0 \end{cases} \tag{4.14}$$

$$\begin{cases} D_a = -jk_1g_2\left[-\dfrac{\partial f_{mn}}{\partial y}\dfrac{\partial f_{ij}}{\partial x}\right] \\ D_b = -jk_1g_2\left[-1-\dfrac{\partial f_{mn}}{\partial y}\dfrac{\partial f_{ij}}{\partial y}\right] \\ D_c = 0 \\ D_d = G_2\left[-(y_n-y_j)\dfrac{\partial f_{mn}}{\partial y}\right. \\ \qquad\qquad \left. -(x_m-x_i)\dfrac{\partial f_{ij}}{\partial x}+(f_{mn}-f_{ij})\right] \\ D_e = G_2\left[\left(\dfrac{\partial f_{mn}}{\partial y}-\dfrac{\partial f_{ij}}{\partial y}\right)(x_m-x_i)\right] \\ D_f = \dfrac{\varepsilon_1}{\varepsilon_2}G_2\left[-\dfrac{\partial f_{mn}}{\partial y}(f_{mn}-f_{ij})\right. \\ \qquad\qquad -(y_n-y_j)] \end{cases} \tag{4.15}$$

$$\begin{cases} E_a = -jk_1 g_2 \left[1 + \dfrac{\partial f_{mn}}{\partial x}\dfrac{\partial f_{ij}}{\partial x}\right] \\ E_b = -jk_1 g_2 \left[\dfrac{\partial f_{mn}}{\partial x}\dfrac{\partial f_{ij}}{\partial y}\right] \\ E_c = 0 \\ E_d = -G_2 \left[\left(-\dfrac{\partial f_{mn}}{\partial x} + \dfrac{\partial f_{ij}}{\partial x}\right)(y_n - y_j)\right] \\ E_e = -G_2 \left[(x_m - x_i)\dfrac{\partial f_{mn}}{\partial x}\right. \\ \qquad\qquad \left. +(y_n - y_j)\dfrac{\partial f_{ij}}{\partial y} - (f_{mn} - f_{ij})\right] \\ E_f = -\dfrac{\varepsilon_1}{\varepsilon_2} G_2 \left[-\dfrac{\partial f_{mn}}{\partial x}(f_{mn} - f_{ij})\right. \\ \qquad\qquad -(x_m - x_i)] \end{cases} \tag{4.16}$$

$$\begin{cases} F_a = jk_1 g_1 \left[\dfrac{\partial f_{ij}}{\partial x} - \dfrac{\partial f_{mn}}{\partial x}\right] \\ F_b = jk_1 g_1 \left[\dfrac{\partial f_{ij}}{\partial y} - \dfrac{\partial f_{mn}}{\partial y}\right] \\ F_c = 0 \\ F_d = G_1 \left[\left(-1 - \dfrac{\partial f_{mn}}{\partial x}\dfrac{\partial f_{ij}}{\partial x}\right)(y_n - y_j)\right. \\ \qquad \left. +(x_m - x_i)\dfrac{\partial f_{ij}}{\partial x}\dfrac{\partial f_{mn}}{\partial y} - (f_{mn} - f_{ij})\dfrac{\partial f_{mn}}{\partial y}\right] \\ F_e = G_1 \left[\left(1 + \dfrac{\partial f_{mn}}{\partial y}\dfrac{\partial f_{ij}}{\partial y}\right)(x_m - x_i)\right. \\ \qquad \left. -(y_n - y_j)\dfrac{\partial f_{mn}}{\partial x}\dfrac{\partial f_{ij}}{\partial y} + \dfrac{\partial f_{mn}}{\partial x}(f_{mn} - f_{ij})\right] \\ F_f = G_1 \left[\dfrac{\partial f_{mn}}{\partial x}(x_m - x_i)\right. \\ \qquad \left. +\dfrac{\partial f_{mn}}{\partial y}(y_n - y_j) - (f_{mn} - f_{ij})\right]. \end{cases} \tag{4.17}$$

The evaluations of the diagonal matrix elements are performed by a two-dimensional quadrature formula numerically. The external integral is carried out by one-point quadrature while the internal one is calculated by generalized Gaussian quadrature. The system matrix is iteratively solved by the Bi-CGSTAB (Vorst, 1992).

4.3 Scattering

For the horizontal incident, the bistatic scattering coefficient in Region 1 is

$$\sigma_\alpha = 4\pi \frac{|E_\alpha^s|^2}{2\eta P_{\text{inc}}} \qquad (\alpha = h, v). \tag{4.18}$$

P_{inc} is the real incident power given in (4.36), and

$$\begin{aligned} E_h^s = &-\frac{jk}{4\pi}\frac{1}{\sqrt{\varepsilon_1}} \int dx'dy' e^{jkr'\cos\psi} \\ &\{[-F_x(\vec{r}')\sin\phi_s + F_y(\vec{r}')\cos\phi_s] \\ &+ [I_x(\vec{r}')\cos\theta_s\cos\phi_s + I_y(\vec{r}')\cos\theta_s\sin\phi_s \\ &- \ I_n(\vec{r}')\sin\theta_s]\} \end{aligned} \tag{4.19}$$

$$\begin{aligned} E_v^s = &-\frac{jk}{4\pi}\frac{1}{\sqrt{\varepsilon_1}} \int dx'dy' e^{jkr'\cos\psi} \\ &\{[I_x(\vec{r}')\sin\phi_s - I_y(\vec{r}')\cos\phi_s] \\ &+ [F_x(\vec{r}')\cos\theta_s\cos\phi_s + F_y(\vec{r}')\cos\theta_s\sin\phi_s \\ &- \ F_n(\vec{r}')\sin\theta_s]\} \end{aligned} \tag{4.20}$$

where

$$\begin{aligned} r'\cos\psi = {} & x'\sin\theta_s\cos\phi_s + y'\sin\theta_s\sin\phi_s \\ &+ f(x', y')\cos\theta_s. \end{aligned} \tag{4.21}$$

In general, the scattered intensities from a random rough surface can be decomposed into coherent and incoherent components as follows (Tsang and Kong, 2001)

$$\sigma_{\alpha\_\text{co}} = 4\pi \frac{|\langle E_\alpha^s\rangle|^2}{2\eta P_{\text{inc}}} \tag{4.22}$$

$$\sigma_{\alpha\_\text{inco}} = 4\pi \frac{\langle |E_\alpha^s|\rangle^2 - |\langle E_\alpha^s\rangle|^2}{2\eta P_{\text{inc}}}. \tag{4.23}$$

Coherent components only contribute to the specular reflected and transmitted directions, whereas incoherent components contribute to all directions. In the limiting case of a very rough surface, coherent components almost vanish and only incoherent components remain.

4.4 Incident Power

The tapered wave (Braunisch *et al.*, 2000) is applied to the truncated rough surface. The superposition of a 2-D spectrum of plane wave incident on the xoy plane from the positive z-axis can be represented as

$$\begin{aligned}\vec{E}_i(\vec{r}) &= \int_{-\infty}^{\infty} d\vec{\kappa}_\rho e^{i(\vec{\kappa}_\rho\cdot\vec{\rho}-k_z z)}\psi(\vec{\kappa}_\rho)\vec{e}(\vec{\kappa}_\rho)\\ \vec{H}_i(\vec{r}) &= \int_{-\infty}^{\infty} d\vec{\kappa}_\rho e^{i(\vec{\kappa}_\rho\cdot\vec{\rho}-k_z z)}\frac{\psi(\vec{\kappa}_\rho)}{\eta}\vec{h}(\vec{\kappa}_\rho)\end{aligned} \tag{4.24}$$

where

$$\begin{aligned}&\vec{r} = \vec{\rho} + \hat{z}z = \hat{x}x + \hat{y}y + \hat{z}z\\ &\vec{\kappa}_\rho = \hat{x}\kappa_x + \hat{y}\kappa_y\\ &k_z = \begin{cases}\sqrt{k^2-\kappa_\rho^2}, & 0 \le \kappa_\rho \le k\\ -i\sqrt{\kappa_\rho^2-k^2}, & \kappa_\rho > k\end{cases}\\ &\psi(\vec{\kappa}_\rho) = \frac{\tau^2}{4\pi}e^{-\frac{\tau^2}{4}\left|\vec{\kappa}_\rho-\vec{k}_{i\rho}\right|^2}\end{aligned} \tag{4.25}$$

The spectrum ψ carries the information on the shape of the footprint of the incident field and is assumed to be centered about

$$\vec{k}_{i\rho} = \hat{x}k_{ix} + \hat{y}k_{iy} = k\sin\theta_i(\hat{x}\cos\varphi_i + \hat{y}\sin\varphi_i) \tag{4.26}$$

The polarization vectors $\vec{e}$ and $\vec{h}$ are of the general forms as follows

$$\begin{aligned}\vec{e}(\vec{\kappa}_\rho) &= e_h(\vec{\kappa}_\rho)\hat{h}(\vec{\kappa}_\rho) + e_v(\vec{\kappa}_\rho)\hat{v}(\vec{\kappa}_\rho)\\ \vec{h}(\vec{\kappa}_\rho) &= e_v(\vec{\kappa}_\rho)\hat{h}(\vec{\kappa}_\rho) - e_h(\vec{\kappa}_\rho)\hat{v}(\vec{\kappa}_\rho)\end{aligned} \tag{4.27}$$

where

$$\begin{aligned}
\hat{h}(\vec{\kappa}_\rho) &= \begin{cases} \hat{x}\sin\varphi_i - \hat{y}\cos\varphi_i, & \kappa_\rho = 0 \\ \frac{1}{\kappa_\rho}(\hat{x}\kappa_y - \hat{y}\kappa_x), & \kappa_\rho > 0 \end{cases} \\
\hat{v}(\vec{\kappa}_\rho) &= \begin{cases} \hat{x}\cos\varphi_i + \hat{y}\sin\varphi_i, & \kappa_\rho = 0 \\ \frac{k_z}{k\kappa_\rho}(\hat{x}\kappa_y + \hat{y}\kappa_x) + \hat{z}\frac{\kappa_\rho}{k}, & \kappa_\rho > 0 \end{cases}
\end{aligned} \tag{4.28}$$

The incident fields produced by the tapered wave of different angles on the planar surface are sketched in Fig. 4.2. It can be clearly seen that, in the case of normal incidence, the footprints are perfect circles whose centers are fully overlapped with that of the planar surface. And the intensity on the edges decays to almost zero, which could avoid the edge effects in scattering problems. For the oblique incidence, the result is tolerable until $\theta_i = 60°$, at which the polar angle the object begins to act as a reflector that directs energy toward the edges. So there may be problems for the scattering calculation when the incident angle is larger than $\theta_i = 60°$.

The complex incident power of the tapered wave is

$$\begin{aligned}
Q =& \int\int_{-\infty}^{\infty} \mathrm{d}x\mathrm{d}y \frac{\vec{E}_i \times \vec{H}_i^*}{2} \cdot (-\hat{z}) \\
=& \frac{1}{2\eta} \int\int_{-\infty}^{\infty} \mathrm{d}\kappa_x \mathrm{d}\kappa_y \int\int_{-\infty}^{\infty} \mathrm{d}\Omega_x \mathrm{d}\Omega_y \int\int_{-\infty}^{\infty} \mathrm{d}x\mathrm{d}y \\
& \Big\{ e^{-j(\vec{\kappa}_\rho\cdot\vec{\rho} - k_z z) + j(\vec{\Omega}_\rho\cdot\vec{\rho} - k_z z)} \psi(\vec{\kappa}_\rho)\psi(\vec{\Omega}_\rho) \\
& \vec{e}(\vec{\kappa}_\rho) \times \vec{h}(\vec{\Omega}_\rho) \cdot (-\hat{z}) \Big\}
\end{aligned} \tag{4.29}$$

Since

$$\vec{e} \times \vec{h} = \hat{k} = \frac{1}{k}(k_x\hat{x} + k_y\hat{y} - k_z\hat{z}) \tag{4.30}$$

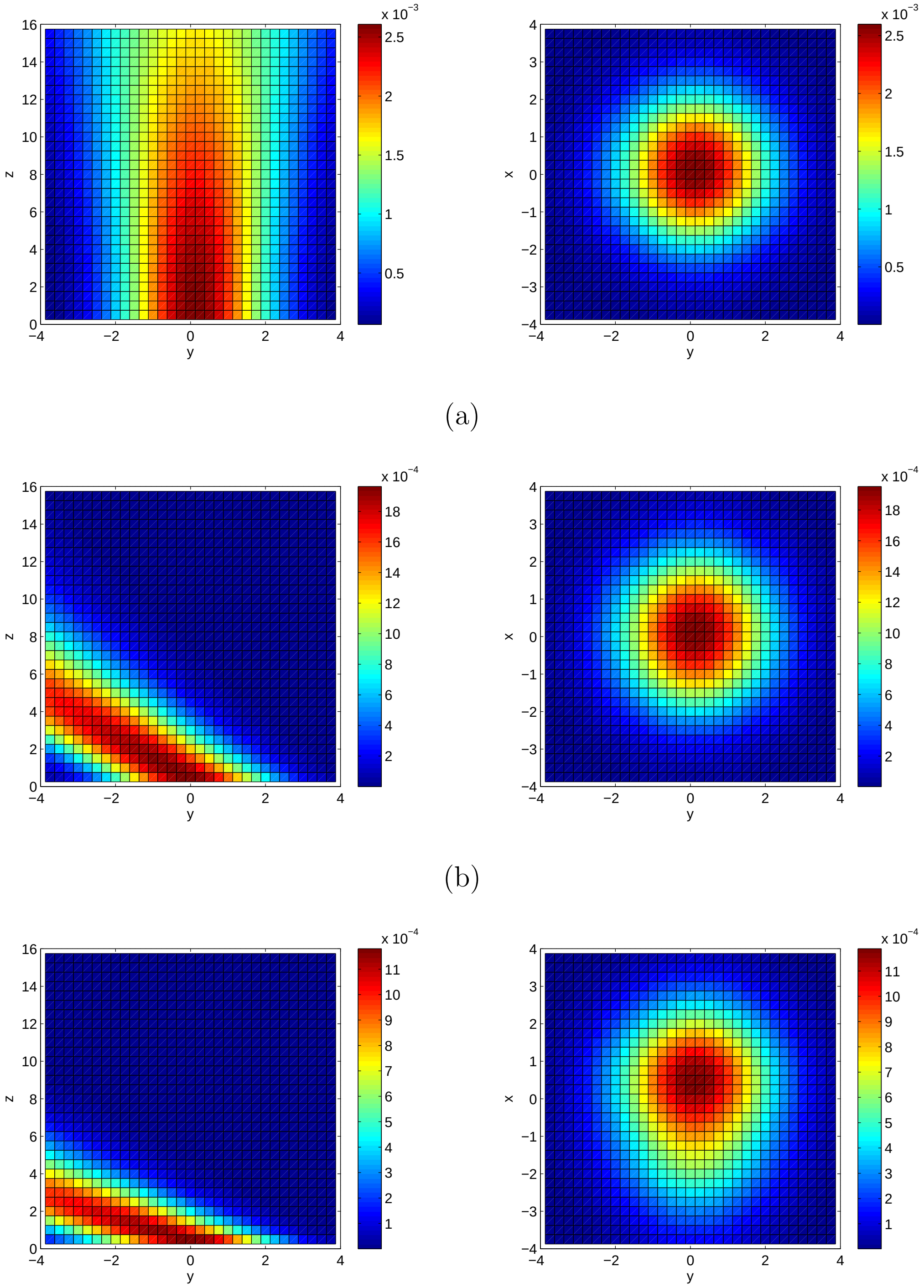

(a)

(b)

(c)

Figure 4.2: Incident Field ${H_y}^i$ of the Tapered Wave ($\tau = 2.0\lambda$) at: (a) $\theta_i = 0°, \phi_i = 90°$; (b) $\theta_i = -40°, \phi_i = 90°$; (c) $\theta_i = -60°, \phi_i = 90°$.

The internal integral in spatial domain can be simplified as

$$\begin{aligned}
&\int\int_{-\infty}^{\infty} \mathrm{d}x\mathrm{d}y e^{-j(\vec{\kappa}_\rho\cdot\vec{\rho}-k_z z)+j(\vec{\Omega}_\rho\cdot\vec{\rho}-k_z z)}\psi(\vec{\kappa}_\rho)\psi(\vec{\Omega}_\rho)\hat{k}\cdot(-\hat{z})\\
=&\int\int_{-\infty}^{\infty} \mathrm{d}x\mathrm{d}y\psi(\kappa_x,\kappa_y)\psi(\Omega_x,\Omega_y)\\
&\qquad\qquad\qquad\times\left\{e^{-j[(\kappa_x-\Omega_x)x+(\kappa_y-\Omega_y)y]}\frac{k_z}{k}\right\}\\
=&4\pi^2\psi(\kappa_x,\kappa_y)\psi(\Omega_x,\Omega_x)\delta(\kappa_x-\Omega_x)\delta(\kappa_y-\Omega_y)\frac{k_z}{k}
\end{aligned}\tag{4.31}$$

Substituting (4.31) into (4.29), we obtain

$$\begin{aligned}
Q=&\frac{2\pi^2}{\eta}\int\int_{-\infty}^{\infty}\mathrm{d}\Omega_x\mathrm{d}\Omega_y\psi(\Omega_x,\Omega_y)\frac{k_z}{k}\\
&\times\int\int_{-\infty}^{\infty}\mathrm{d}\kappa_x\mathrm{d}\kappa_y\psi(\kappa_x,\kappa_y)\delta(\kappa_x-\Omega_x)\delta(\kappa_y-\Omega_y)\\
=&\frac{2\pi^2}{\eta}\int\int_{-\infty}^{\infty}\mathrm{d}\Omega_x\mathrm{d}\Omega_y\psi(\Omega_x,\Omega_y)\psi(\Omega_x,\Omega_y)\frac{k_z}{k}\\
=&\frac{2\pi^2}{\eta}\int\int_{-\infty}^{\infty}\mathrm{d}\kappa_x\mathrm{d}\kappa_y\psi^2(\kappa_x,\kappa_y)\frac{k_z}{k}\\
=&\frac{\tau^4}{8\eta}\int\int_{-\infty}^{\infty}\mathrm{d}k_x\mathrm{d}k_y e^{-\frac{\tau^2}{2}|k_\rho-k_{i\rho}|^2}\frac{k_z}{k}
\end{aligned}\tag{4.32}$$

Consequently, the real incident power is

$$\begin{aligned}
P_{\mathrm{inc}}=&\operatorname{Re}(Q)\\
=&\frac{\tau^4}{8\eta}\int\int_{k_\rho\le k}\mathrm{d}k_x\mathrm{d}k_y e^{-\frac{\tau^2}{2}[(k_x-k_{ix})^2+(k_y-k_{iy})^2]}\\
&\qquad\qquad\times\sqrt{1-(k_x/k)^2-(k_y/k)^2}
\end{aligned}\tag{4.33}$$

Assume the general incident plane is yoz plane. Thus, $k_{ix}=0$ and $k_{iy}=k\sin\theta_i$.

$$\begin{aligned}
P_{\mathrm{inc}}=&\frac{\tau^4}{8\eta}\int\int_{k_\rho\le k}\mathrm{d}k_x\mathrm{d}k_y e^{-\frac{\tau^2}{2}[k_x^2+(k_y-k_{iy})^2]}\\
&\qquad\qquad\times\sqrt{1-(k_x/k)^2-(k_y/k)^2}\\
=&\frac{\tau^4k^2}{8\eta}\int\int_{k_\rho\le k}\mathrm{d}\left(\frac{k_x}{k}\right)\mathrm{d}\left(\frac{k_y}{k}\right)e^{-\frac{k^2\tau^2}{2}\left(\frac{k_x}{k}\right)^2}\\
&\times e^{-\frac{k^2\tau^2}{2}\left(\frac{k_y}{k}-\sin\theta_i\right)^2}\sqrt{1-(k_x/k)^2-(k_y/k)^2}
\end{aligned}\tag{4.34}$$

Defining $k_x/k = \rho\cos\chi, k_y/k = \rho\sin\chi$ and applying the integral relationship of exponent and Bessel functions (Jeffrey and Zwillinger, 2007) to the inner integral, we can derive

$$\begin{aligned} P_{\text{inc}} &= \frac{\tau^2(k\tau)^2}{8\eta}\int\limits_{\rho=0}^{1}\int\limits_{\chi=0}^{2\pi}\rho\mathrm{d}\rho\mathrm{d}\chi\sqrt{1-\rho^2} \\ &\qquad\qquad \times e^{-\frac{(k\tau)^2}{2}\left[\rho^2\cos^2\chi+(\rho\sin\chi-\sin\theta_i)^2\right]} \\ &= \frac{\pi\tau^2}{4\eta}e^{-\frac{(k\tau\sin\theta_i)^2}{2}}(k\tau)^2 \\ &\qquad \times\int\limits_{0}^{1} I_0\left[(k\tau)^2\rho\sin\theta_i\right]e^{-\frac{(k\tau)^2}{2}\rho^2}\rho\sqrt{1-\rho^2}\mathrm{d}\rho \end{aligned} \tag{4.35}$$

Let $\beta = (k\tau)^2\sin\theta_i/2, \alpha = (k\tau)^2/2$ and $u = \rho^2$. Equation (4.35) becomes

$$P_{inc} = \frac{\pi\tau^2}{4\eta}\frac{\alpha}{e^{\beta^2/\alpha}}\int\limits_{0}^{1} I_0\left(2\beta\sqrt{u}\right)e^{-\alpha u}\sqrt{1-u}du \tag{4.36}$$

Equation (4.36) is the semi-analytical solution to the incident power of the tapered wave. It only consists of a simple 1-D integral which can consequently speed up computations of the normalization factor in scattering coefficients. Table 4.1 compares these analytical solutions of the tapered incident power with numerical data collected from a $8\lambda \times 8\lambda$ plate, under incidents of multiple angles ($\phi_i = 90^\circ$ and $\tau = 2.4\lambda$). The relative error of analytical solutions to numerical data can be controlled under 1%. For the iterative expression of (4.36), please refer to Appendix A.

4.5 Numerical Results

Numerical validation and examples are presented in this section. All 2-D random rough surfaces are generated with pre-specified Gaussian statistics, and truncated due to the limitation of computational resources.

Table 4.1: Incident Power of the Tapered Wave ($\tau = 2.4\lambda$)

θ_i°	Numerical data	Analytical data	Error/%
0	0.01187180	0.01194648	0.629
30	0.01025520	0.01032015	0.633
60	0.00562885	0.00566999	0.731
80	0.00213183	0.00213691	0.238

4.5.1 Validations

To assess the accuracy of the solution, a $8\lambda \times 8\lambda$ conducting rough surface ($\varepsilon_{r2} = 1 - 20000j$) is generated with a Gaussian rms height $h = 0.2\lambda$ and a Gaussian correlation length $l_x = l_y = 1.0\lambda$. Four Coifman scalets per wavelength are employed over the rough surface. A horizontal tapered wave incident is specified as $\theta_i = -40°$ and $\phi_i = 90°$. The negative θ_i represents the incident wave is located in the 2nd quadrant of the incident plane yoz. In Fig. 4.3 the sparsity pattern of the resulting matrix indicates normal components of H-field and tangential components of E-field have vanished. However, the impedance matrix is not decoupled. In fact, the three patches are linked by the sub-diagonals. The excited surface currents and the normal components of surface fields are selected at a cross section of $y = 6.25\lambda$, as shown in Fig 4.4. The corresponding co-polarized (HH) and cross-polarized (VH) bistatic scattering coefficients from a single realization of the $8\lambda \times 8\lambda$ conducting random surface are displayed in Fig. 4.5. Good agreement can be observed with the MFIE results in the PEC case (Pan *et al.*, 2004). Similarly, Fig 4.6 displays bistatic scattering from a single $16\lambda \times 16\lambda$ surface with the aforementioned sampling rate and roughness. The detailed parameters, such as number of unknowns, matrix filling and solving time, number of iterations and condition numbers are tabulated in Table 4.2. Numerical results demonstrate that the reduced PEC model does not suffer from ill-posed problems, namely, matrix condition numbers are kept small and solutions are stable under extremely large loss-tangent, because the reduced system is still the Fredholm of the 2nd kind.

Fig. 4.7 shows the average bistatic scattering coefficients resulting from 20 realizations of $8\lambda \times 8\lambda$ dielectric rough surfaces with $h = 0.2\lambda, l_x = l_y = 1.0\lambda$ and $\varepsilon_{r2} = 6.5 - 1.0j$. The sampling rate is eight Coifman scalets per wavelength. Comparisons between cases of horizontal incidence and vertical incidence have been conducted with the incident angle of $\theta_i = -20°$ and $\phi_i = 90°$. It can be seen $\sigma_{HV} \approx \sigma_{VH}$, namely the reciprocity is satisfied. The average bistatic scattering coefficients from 40 realizations of $16\lambda \times 16\lambda$ dielectric rough surfaces with the above parameters are also provided in Fig. 4.8.

Table 4.2: Parameter Comparisons between PEC Code (MFIE) and Dielectric Code (Our Normalized Surface IE)

	Size $/\lambda^2$	Unknowns	Matrix-Filling Total/sec (diag./%)	Matrix-Solving /sec	Iter.	Condition No.
PEC	8×8	2048	4103 (100.00)	<1	4	5.71
	16×16	8192	15204 (99.09)	2	5	11.64
Dielectric	8×8	6144	4670 (99.96)	1	4	85.32
	16×16	24576	20123 (96.09)	39	5	259.42

Fig. 4.9 and Fig. 4.10 show the average backscattering results for a conducting surface ($\varepsilon_{r2} = 1 - 2000j$) and a lossy dielectric one ($\varepsilon_{r2} = 20 - 20j$), respectively, with two groups of random rough surfaces of different roughness. For each case, 20 realizations of $8\lambda \times 8\lambda$ surfaces are applied and a limited range of the incident angles is selected due to the necessary modifications required on the current Coiflet

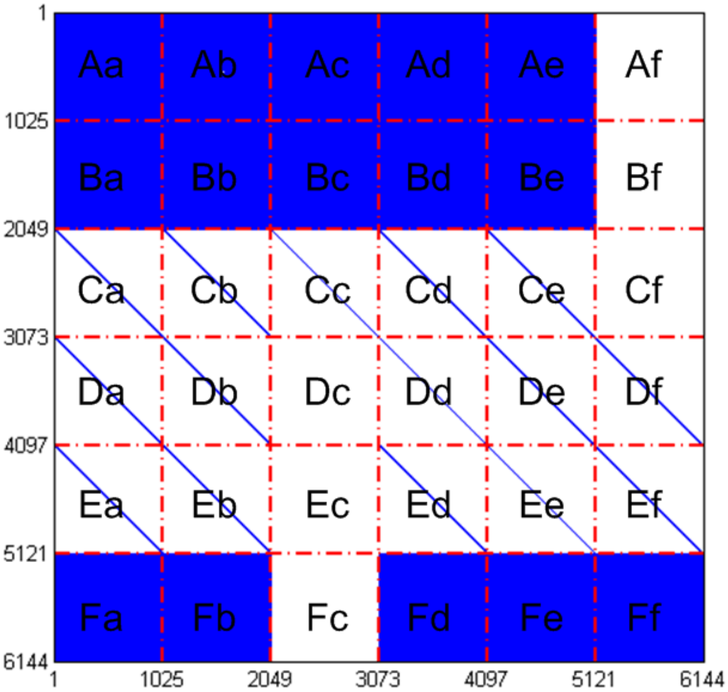

Figure 4.3: Sparsity Pattern of the Matrix for a Single $8\lambda \times 8\lambda$ Dielectric Surface ($h = 0.2\lambda, l_x = l_y = 1.0\lambda, \varepsilon_{r2} = 1 - 20000j$). Blue color represents nonzeros while white color represents zeros.

model for large incidence. The incoherent components of co-polarization from the numerical Coiflet method are compared with the results of first-order perturbation theory (PT), Kirchhoff approximation (KA) and first-order Wiener-Hermite (FWH) expansion (Eftimiu and Pan, 1990). The first group of the statistical surfaces has the roughness of $kh = 0.1$ and $kl = 3.0$ and thus the perturbation method needs to be used (Ulaby *et al.*, 1982), since

$$\begin{aligned} &kh < 0.3 \\ &\sqrt{2}h/l < 0.3 \end{aligned} \tag{4.37}$$

The second group of rough surfaces with $kh = 0.66$ and $kl = 7.0$ qualify the

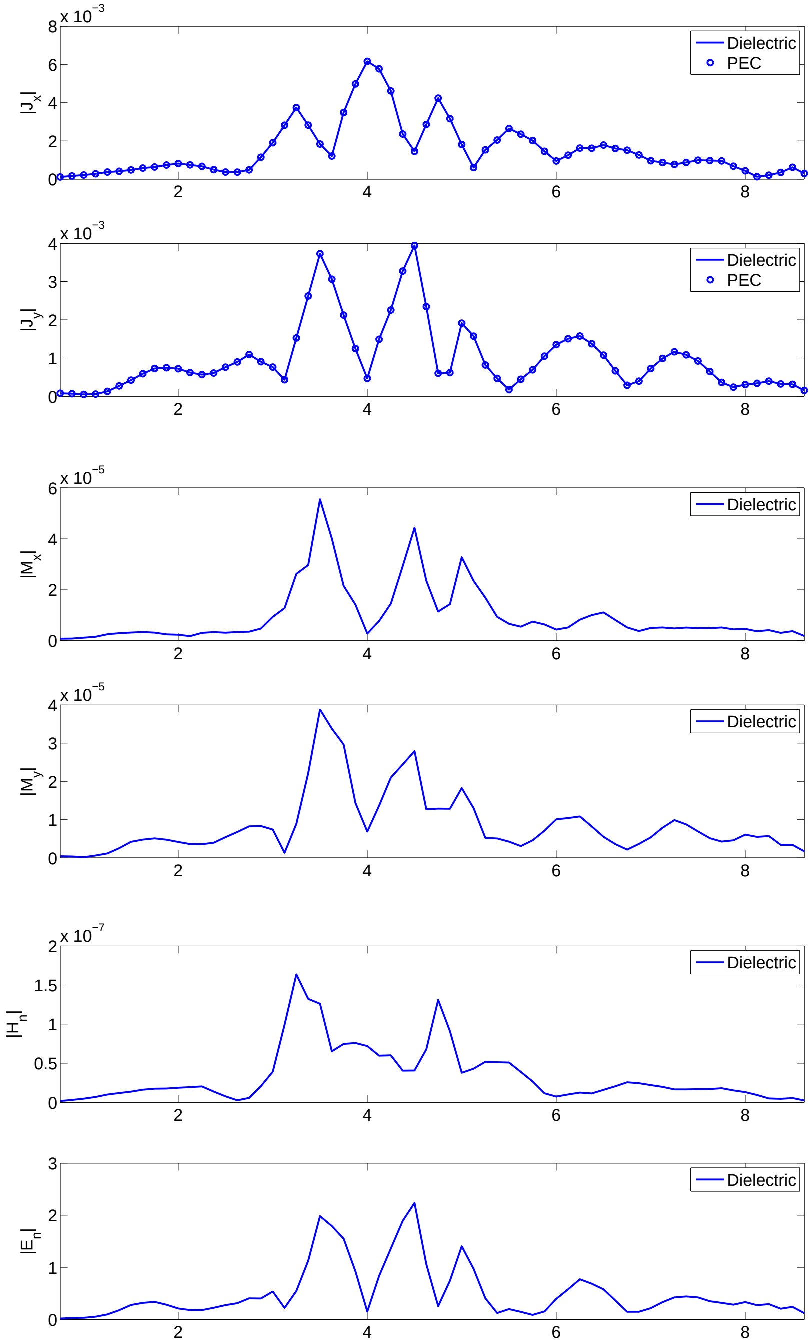

Figure 4.4: The Magnitude of Surface Currents and Field Normal Components at the Cross Section of $y = 6.25\lambda$ for a Single $8\lambda \times 8\lambda$ Dielectric Surface ($h = 0.2\lambda, l_x = l_y = 1.0\lambda, \varepsilon_{r2} = 1 - 20000j$), Compared to PEC Case. (Horizontal Incidence with $\theta_i = -40°$ and $\phi_i = 90°$)

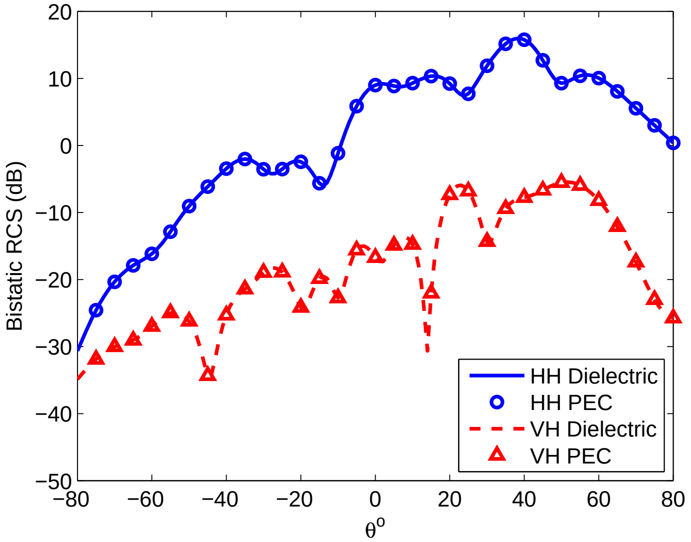

Figure 4.5: Bistatic RCS of a Single $8\lambda \times 8\lambda$ Dielectric Surface ($h = 0.2\lambda, l_x = l_y = 1.0\lambda, \varepsilon_{r2} = 1 - 20000j$), Compared to PEC Case. Both Coherent and Incoherent Components Are Included in the Comparison Above. (Horizontal Incidence with $\theta_i = -40°$ and $\phi_i = 90°$)

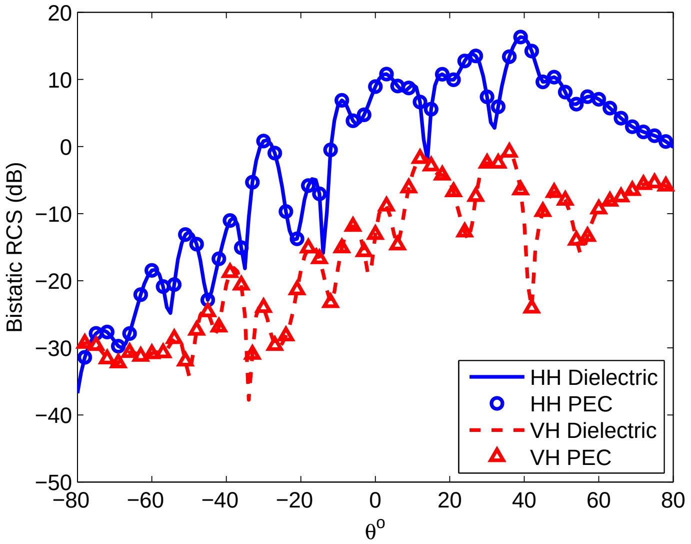

Figure 4.6: Bistatic RCS of a Single $16\lambda \times 16\lambda$ Dielectric Surface ($h = 0.2\lambda, l_x = l_y = 1.0\lambda, \varepsilon_{r2} = 1 - 20000j$), Compared to PEC Case. Both Coherent and Incoherent Components Are Included in the Comparison Above. (Horizontal Incidence with $\theta_i = -40°$ and $\phi_i = 90°$)

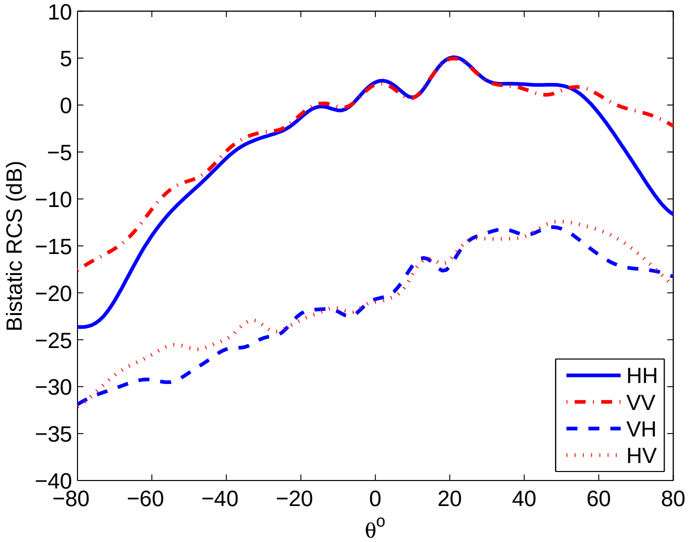

Figure 4.7: Average Bistatic RCS Comparisons between Horizontal Incidence and Vertical Incidence, Resulting from 20 Realizations of $8\lambda \times 8\lambda$ Random Gaussian Surfaces ($h = 0.2\lambda, l_x = l_y = 1.0\lambda, \varepsilon_{r2} = 6.5 - 1.0j$). Both Coherent and Incoherent Components Are Included ($\theta_i = -20^\circ$ and $\phi_i = 90^\circ$).

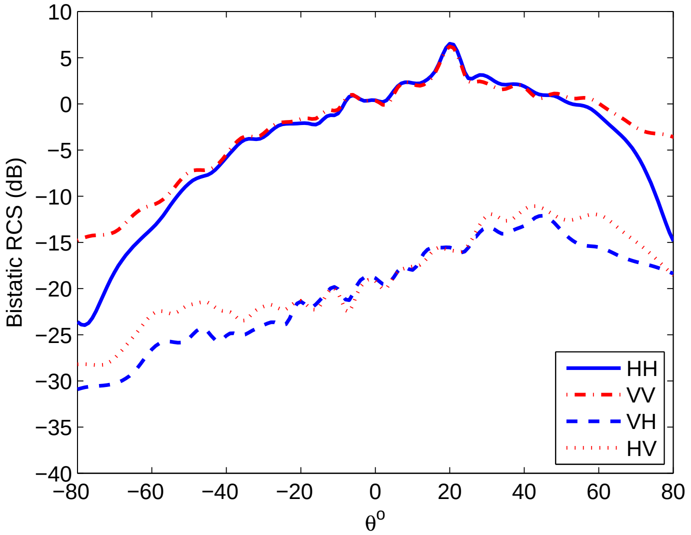

Figure 4.8: Average Bistatic RCS Comparisons between Horizontal Incidence and Vertical Incidence, Resulting from 40 Realizations of $16\lambda \times 16\lambda$ Random Gaussian Surfaces ($h = 0.2\lambda, l_x = l_y = 1.0\lambda, \varepsilon_{r2} = 6.5 - 1.0j$). Both Coherent and Incoherent Components Are Included ($\theta_i = -20^\circ$ and $\phi_i = 90^\circ$).

restrictions of the Kirchhoff scattering model, mathematically as (Ulaby *et al.*, 1982):

$$\begin{aligned} &kl > 6 \\ &l^2 > 2.76h\lambda \end{aligned} \tag{4.38}$$

Fig. 4.11 and Fig. 4.12 present similar backscattering from 40 realizations of $16\lambda \times 16\lambda$ surfaces. It can be seen that the Coiflet results can well match that of the SPM model for scattering from slightly rough surfaces ($kh = 0.1$ and $kl = 3.0$). Again, good agreement can also be observed between the Coiflet method and the KA model in intermediate surfaces ($kh = 0.66$ and $kl = 7.0$).

4.5.2 Examples

Surface with Intermediate Roughness

Here the truncated $8\lambda \times 8\lambda$ dielectric rough surface is modeled with the following parameters: Gaussian standard deviation $h = 0.2\lambda$, Gaussian correlation length $l_x = l_y = 0.6\lambda$, $\varepsilon_{r2} = 6.5 - 1.0j$. Horizontal incidence is at $\theta_i = -10^\circ$ and $\phi_i = 90^\circ$. Eight Coifman scalets per wavelength are employed, resulting in the number of unknowns $N = (8 \times 8)^2 \times 6 = 24576$ and the complex valued system matrix of N^2.

Fig. 4.13 depicts the surface induced electric currents and magnetic currents over one surface realization. The vanishing currents around the boundaries demonstrate in return the characteristics of the negligible near-edge power density of the incident tapered wave. The normal components of the induced fields are also included in Fig. 4.13. Accordingly, Fig. 4.14 presents the radar cross-section for the abovementioned realization. The total matrix fill time takes 18611 seconds, in which $(N^2 - N)$ off-diagonal entries from one-point quadrature consume 60 seconds (0.322%). Meanwhile, matrix solving time totals 156 seconds with 18 iterations at the accuracy of 6.42367×10^{-4} (convergence criterion is 1×10^{-3}).

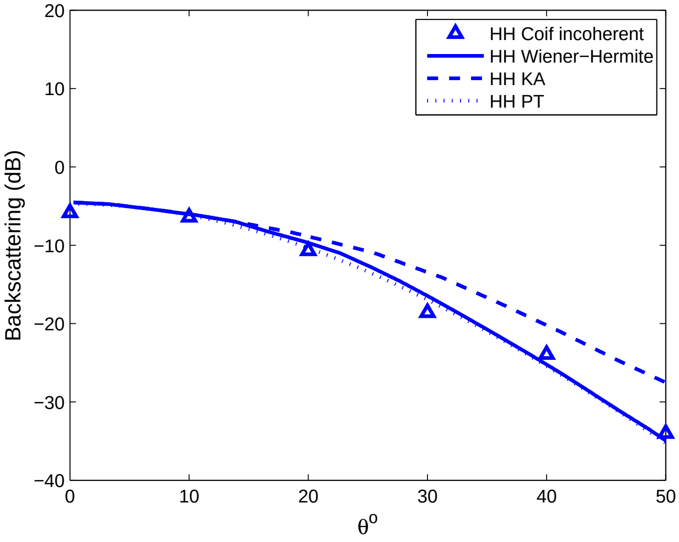

(a)

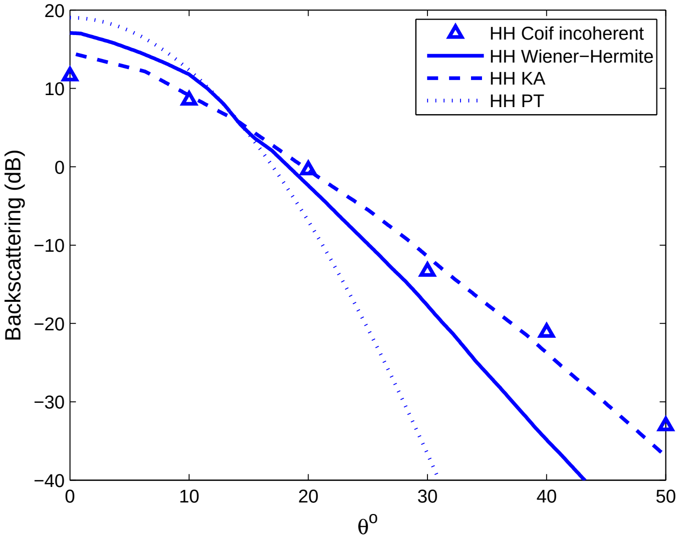

(b)

Figure 4.9: Average Backscattering RCS Comparisons among Methods of Coiflet, PT, KA and First Order Wiener-Hermite, for 20 Realizations of $8\lambda \times 8\lambda$ Conducting Gaussian Surfaces ($\varepsilon_{r2} = 1 - 2000j$): (a) $kh = 0.1$ and $kl = 3.0$; (b) $kh = 0.66$ and $kl = 7.0$. Only the Incoherent Components of Co-Polarization Are Considered.

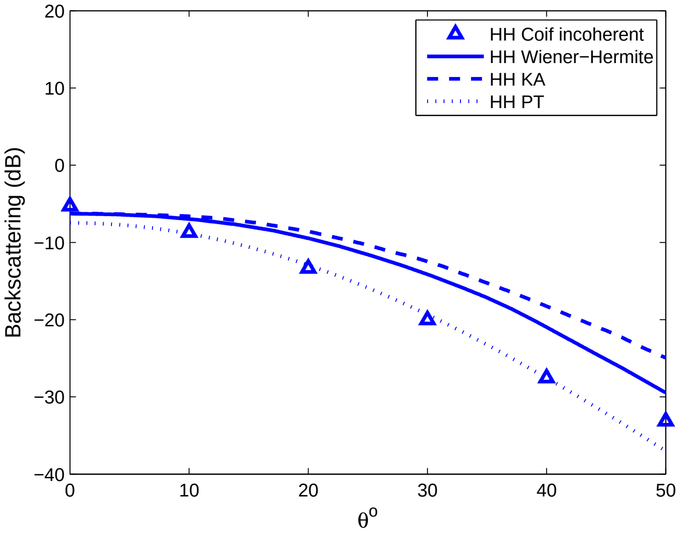

(a)

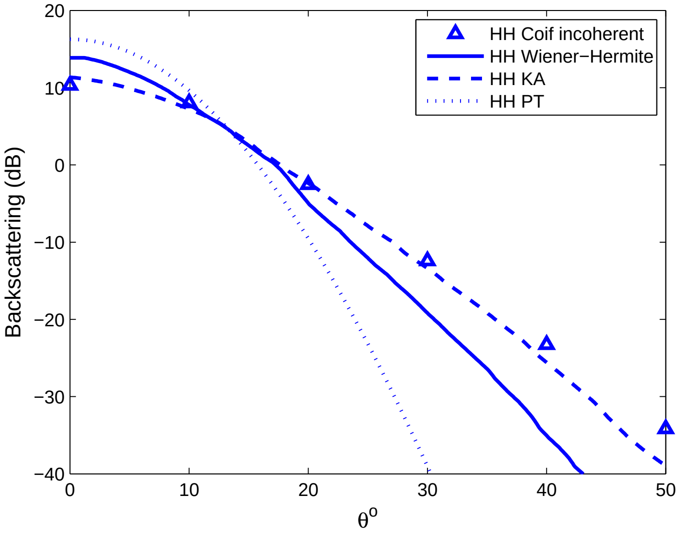

(b)

Figure 4.10: Average Backscattering RCS Comparisons among Methods of Coiflet, PT, KA and First Order Wiener-Hermite, for 20 Realizations of $8\lambda \times 8\lambda$ Dielectric Gaussian Surfaces ($\varepsilon_{r2} = 20 - 20j$): (a) $kh = 0.1$ and $kl = 3.0$; (b) $kh = 0.66$ and $kl = 7.0$. Only the Incoherent Components of Co-Polarization Are Considered.

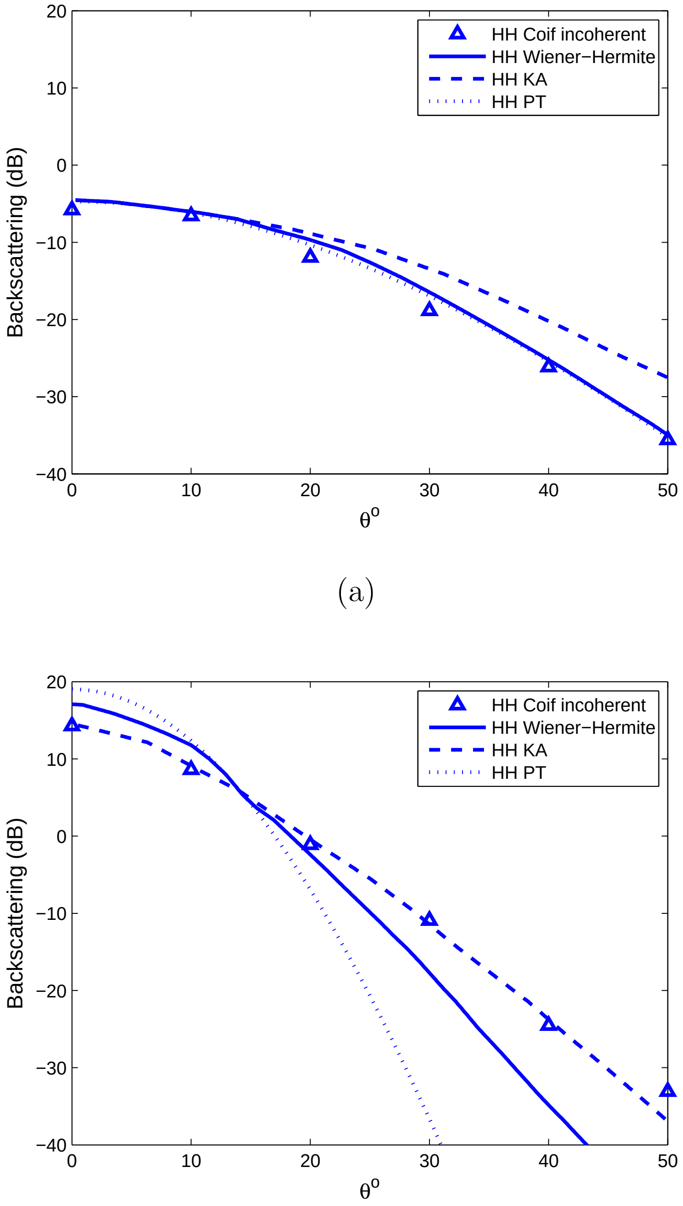

(a)

(b)

Figure 4.11: Average Backscattering RCS Comparisons among Methods of Coiflet, PT, KA and First Order Wiener-Hermite, for 20 Realizations of $16\lambda \times 16\lambda$ Conducting Gaussian Surfaces ($\varepsilon_{r2} = 1 - 2000j$): (a) $kh = 0.1$ and $kl = 3.0$; (b) $kh = 0.66$ and $kl = 7.0$. Only the Incoherent Components of Co-Polarization Are Considered.

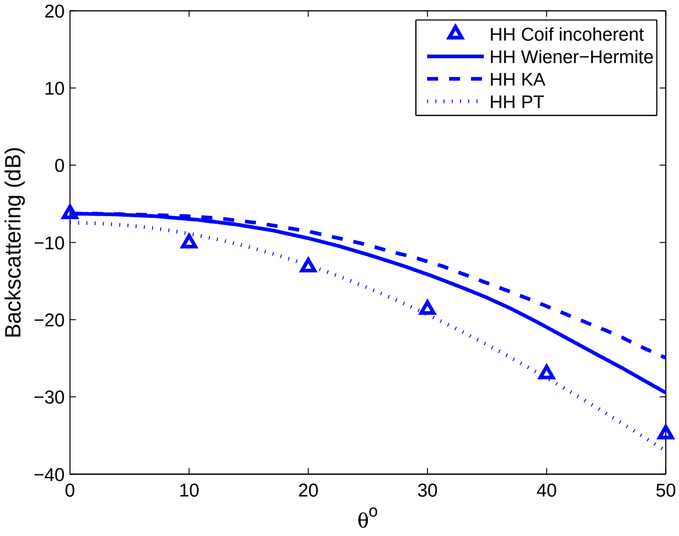

(a)

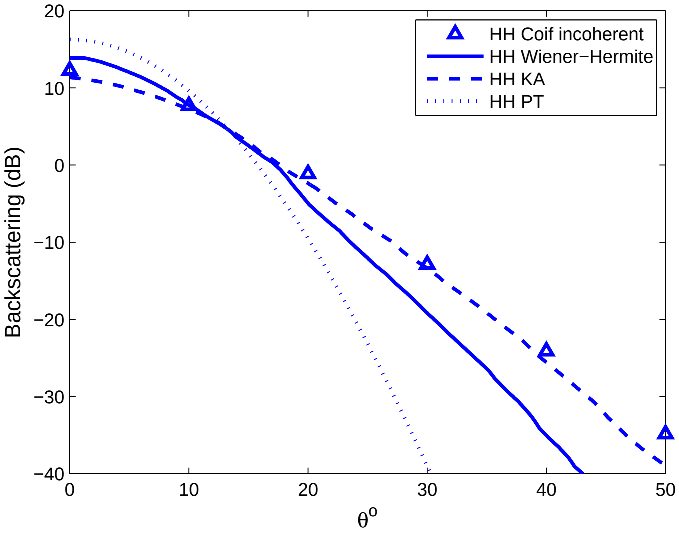

(b)

Figure 4.12: Average Backscattering RCS Comparisons among Methods of Coiflet, PT, KA and First Order Wiener-Hermite, for 20 Realizations of $16\lambda \times 16\lambda$ Dielectric Gaussian Surfaces ($\varepsilon_{r2} = 20 - 20j$): (a) $kh = 0.1$ and $kl = 3.0$; (b) $kh = 0.66$ and $kl = 7.0$. Only the Incoherent Components of Co-Polarization Are Considered.

In Fig. 4.15, the average bistatic co-polarized scattering coefficients of 300 realizations are compared with results of SMCG method (Pak *et al.*, 1997), with good agreement (except the backscattering enhancement). Both coherent and incoherent components are included in the comparison above. Fig. 4.16 separates coherent and incoherent components for bistatic co-polarized and cross-polarized RCS, respectively.

The mismatching can be improved by the utilization of $16\lambda \times 16\lambda$ rough surfaces in Fig. 4.17, while the rest initial parameters are kept identical to $8\lambda \times 8\lambda$ case. Separated coherent and incoherent components are shown in Fig. 4.18. For a certain single surface realization, total matrix fill time takes 85762 seconds, since the number of unknowns ($N = (16 \times 8)^2 \times 6 = 98304$) is as 4 times as the one in $8\lambda \times 8\lambda$ case. Meanwhile, the off-diagonal entries consume 894 seconds (1.042%), corresponding to the increase of approximately 16 times in off-diagonal matrix elements. Matrix solving time is still stable with 159 seconds (21 iterations). The convergence criterion (1×10^{-3}) can be generally reached within 25 iterations during matrix solving procedure for each realization.

Very Rough Surface

The benchmark structures for the dielectric surfaces were fabricated accurately by a computer-numerical-controlled (CNC) milling machine (Ailes-Sengers *et al.*, 1995; Phu *et al.*, 1994, 1993; Ishimaru *et al.*, 1996). At the experimental frequencies from 75GHz to 100GHz, the relative permittivity of the structure material is $7-13j$, which is very lossy. We selected the surfaces with a Gaussian probability density function of $h = \lambda$ and Gaussian correlation function of $l_x = l_y = 2\lambda$. The truncated $16\lambda \times 16\lambda$ surface is illuminated by a horizontal tapered wave at $\theta_i = -20^\circ$ and $\phi = 90^\circ$. Eight Coiflets per wavelength are still maintained for this extremely rough surface. The numerical results are the average of 300 realizations, and the convergence criterion

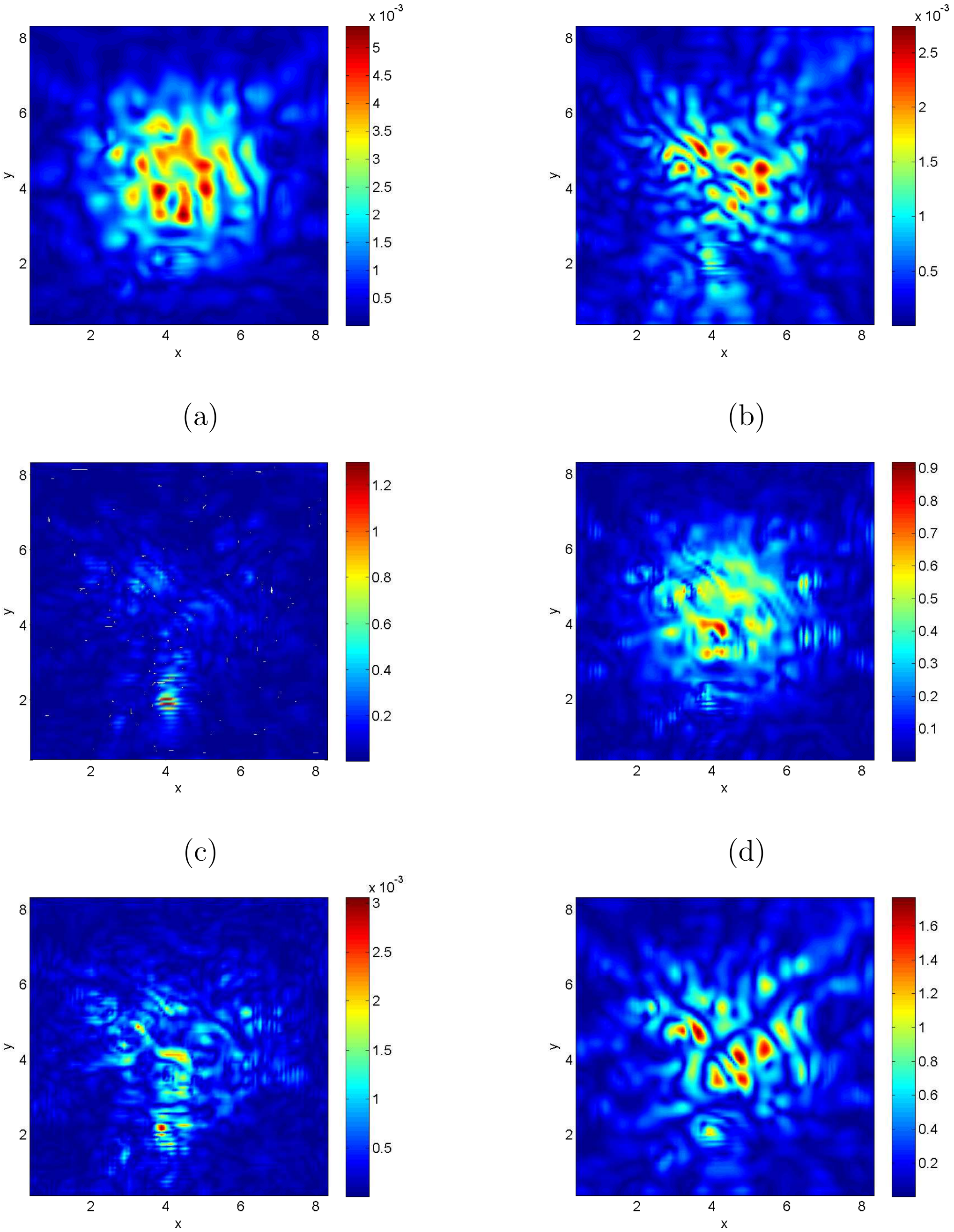

(a) (b)

(c) (d)

(e) (f)

Figure 4.13: The Magnitude of Surface Currents and Field Normal Components for a Single $8\lambda \times 8\lambda$ Gaussian Surface ($h = 0.2\lambda, l_x = l_y = 0.6\lambda, \varepsilon_{r2} = 6.5 - 1.0j$) : (a) J_x; (b) J_y; (c) M_x; (d) M_y; (e) H_n; (f) E_n. (Horizontal Incidence with $\theta_i = -10°$ and $\phi_i = 90°$)

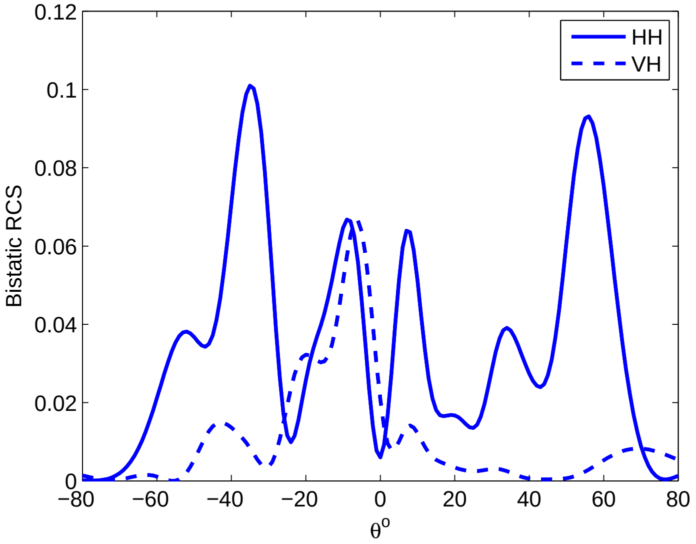

Figure 4.14: The Bistatic RCS from a Single $8\lambda \times 8\lambda$ Surface Realization with $h = 0.2\lambda$, $l_x = l_y = 0.6\lambda$ and $\varepsilon_{r2} = 6.5 - 1.0j$ (Horizontal Incidence with $\theta_i = -10°$ and $\phi_i = 90°$).

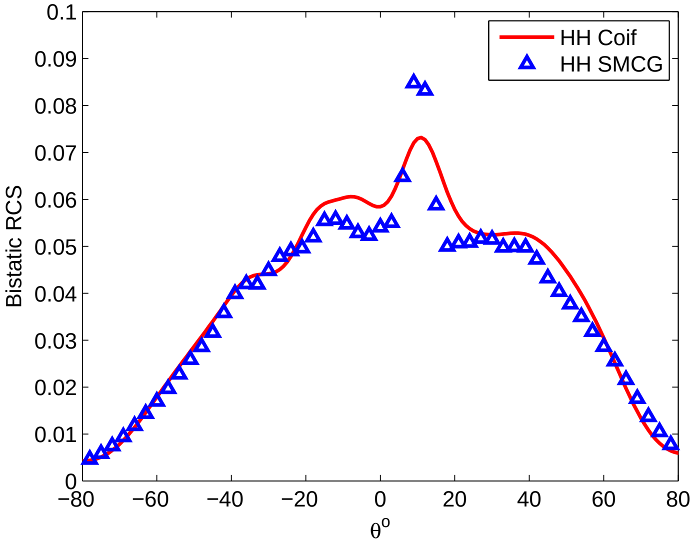

Figure 4.15: Average Bistatic Co-Polarized RCS Compared with SMCG Method over 300 Realizations of $8\lambda \times 8\lambda$ Random Gaussian Surfaces ($h = 0.2\lambda$, $l_x = l_y = 0.6\lambda$, $\varepsilon_{r2} = 6.5 - 1.0j$). Both Coherent and Incoherent Components Are Included.

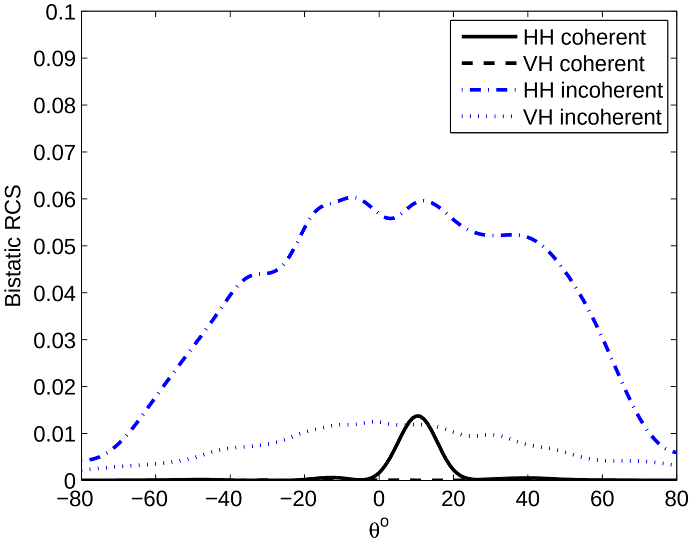

Figure 4.16: Average Bistatic Co-Polarized and Cross-Polarized RCS with Coherent and Incoherent Components Respectively ($8\lambda \times 8\lambda$ Surfaces).

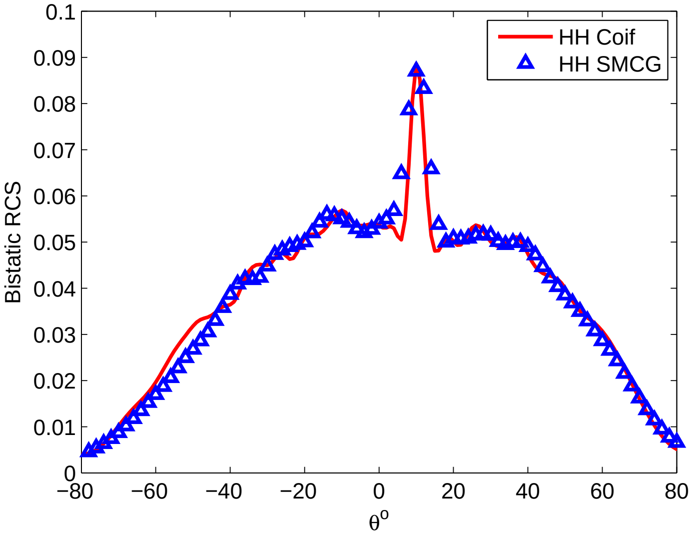

Figure 4.17: Average Bistatic Co-Polarized RCS Compared with SMCG Method over 300 Realizations of $16\lambda \times 16\lambda$ Random Gaussian Surfaces ($h = 0.2\lambda$, $l_x = l_y = 0.6\lambda$, $\varepsilon_{r2} = 6.5 - 1.0j$). Both Coherent and Incoherent Components Are Included.

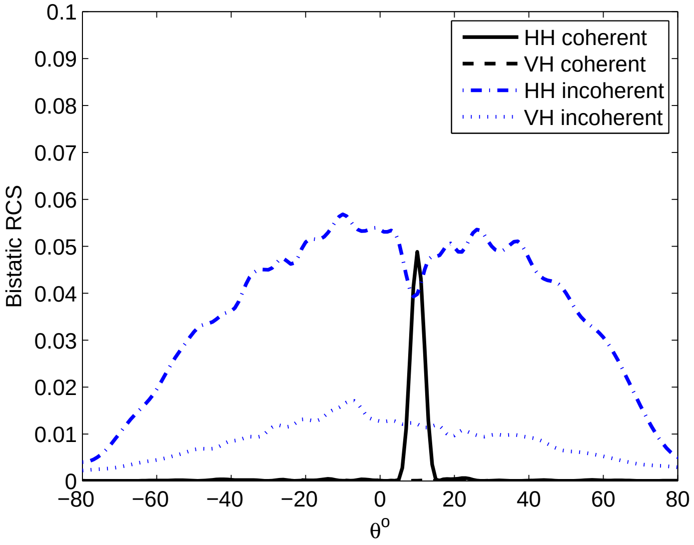

Figure 4.18: Average Bistatic Co-Polarized and Cross-Polarized RCS with Coherent and Incoherent Components Respectively ($16\lambda \times 16\lambda$).

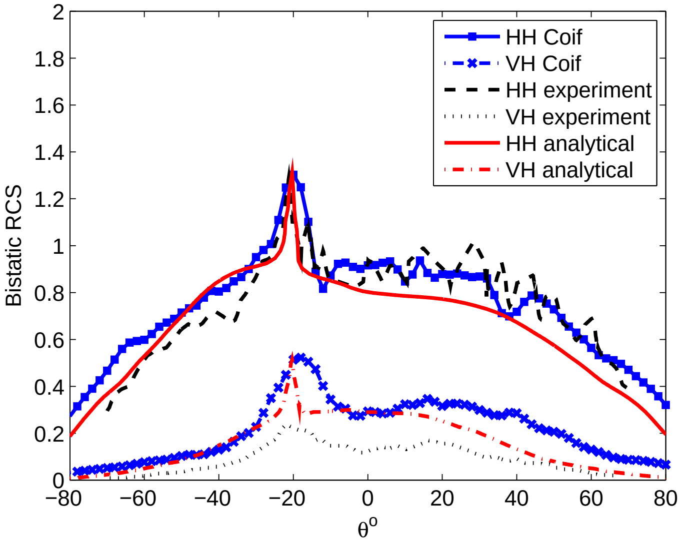

Figure 4.19: Average Bistatic Co-Polarized and Cross-Polarized RCS Compared with Experiment over 300 Realizations of $16\lambda \times 16\lambda$ Random Gaussian Surfaces ($h = 1\lambda$, $l_x = l_y = 2\lambda$, $\varepsilon_{r2} = 7 - 13j$).

(1×10^{-3}) can be reached within 13 iterations during matrix solving procedure for each realization.

Fig. 4.19 demonstrates that the Coiflets based numerical results have fairly good agreement with experimental data and analytical solutions (Ailes-Sengers *et al.*, 1995). The computed cross-polarization scattering coefficients, like the analytical solution in the same publication, are higher than experimental data, but the curves all follow similar trend. This is mainly due to the fact that the truncated surface is not large enough and the resulting edge diffraction affects the sensitive cross-polarization. The cross-polarization setup of the experiment might also contribute to the discrepancy. Here the coherent components almost vanish and only incoherent components exist. Clear backscattering enhancement can be observed in both co- and cross-polarization.

Chapter 5

CONCLUSION

We present fast numerical scattering algorithms for 3-D PEC and dielectric random rough surface in microwave remote sensing. The compactly supported Coifman wavelets are employed to discretize the surface integral equations. The Coiflets are continuous, smooth and orthogonal, which permit great reduction of the sampling rate and dramatic compression of the matrix size. In addition, a Dirac-δ like property of Coiflets allows fast calculation of the most off-diagonal entries in the impedance matrix, which slashes the computational efforts for matrix filling from $O(N^2)$ to $O(N)$.

The MFIE method is applied to solve scattering problems from PEC rough surfaces, and the complexity of the algorithm is numerically determined to be in between $O(N)$ and $O(N \log N)$. The resulting impedance matrix is further compressed by SFWT. The solution accuracy and matrix sparsity can be well balanced by proper selection of the coarsest level of the total transformation matrix. Numerical examples are conducted for undulating and sharp surfaces and the results exhibit good agreement with the RWG-FLFMA based commercial software FEKO. The proposed algorithm can be easily implemented for parallel computing.

The unified algorithm for dielectric rough surfaces can reduce to the PEC case when loss tangent grows very large. The Monte Carlo simulations are conducted for a wide range of material parameters from low-loss dielectrics to PEC cases, and the results are stable and fast converged. In terms of geometric shapes and statistical specifications, the algorithm is also robust. Comparing to the published literature and laboratory measurement, good agreement has been observed.

REFERENCES

Ailes-Sengers, L., A. Ishimaru and Y. Kuga, “Analytical and experimental studies of electromagnetic waves scattered by two-dimensional, dielectric very rough surfaces”, in “Proceedings of the International Geoscience and Remote Sensing Symposium”, pp. 1349–1351 (Firenze, 1995).

Beylkin, G., “Wavelets and fast numerical algorithms”, Proc. Symp. Appl. Math. **47**, 89–117 (1993).

Beylkin, G., R. Coifman and V. Rokhlin, “Fast wavelet transforms and numerical algorithms I”, Commun. Pure Appl. Math. **44**, 2, 141–183 (1991).

Bleszynski, E., M. Bleszynski and T. Jaroszewicz, “Surface integral equations for electromagnetic scattering from impenetrable and penetrable sheets”, IEEE Antennas Propagat. Mag. **35**, 5, 14–25 (1993).

Bleszynski, E., M. Bleszynski and T. Jaroszewicz, “AIM: Adaptive integral method for solving large scale electromagnetic scattering and radiation problems”, Raddio Sci. **31**, 5, 1225–1251 (1996).

Braunisch, H., Y. Zhang, C. Ao, Y. Yang, K. Ding, J. A. Kong and L. Tsang, “Tapered wave with dominant polarization state for all angles of incidence”, IEEE Trans. Antennas Propag. **48**, 7, 1086–1096 (2000).

Brennan, C., T. X. Dung, M. Mullen, P. Bradley and M. Condon, “Improved forward backward method with spectral acceleration for scattering from randomly rough lossy surfaces”, IEEE Trans. Antennas Propag. **61**, 7, 3922–3926 (2013).

Chew, W. C., C. P. Davis, K. F. Warnick, Z. P. Nie, J. Hu, S. Yan and L. Gurel, “Efie and mfie, why the difference?”, in “Proceedings of Antennas and Propagation Society International Symposium”, pp. 1–2 (San Diego, CA, 2008).

Cools, K., F. P. Andriulli, D. D. Zutter and E. Michielssen, “Accurate and conforming mixed discretization of the mfie”, IEEE Antennas Wireless Propag. Lett. **10**, 528–531 (2011).

Daubechies, I., *Ten Lectures on Wavelets* (SIAM, Philadelphia, PA, 1992).

Duff, I. S., E. M. Erisman and J. K. Reid, *Direct methods for Sparse Matrices* (Oxford Science Publication, 1986).

Eftimiu, C., “First-order wiener-hermite expansion in the electromagnetic scattering by conducting rough surfaces”, Radio Sci. **23**, 5, 769–779 (1988).

Eftimiu, C., “Modified wiener-hermite expansion in rough-surface scattering”, J. Opt. Soc. Am. **6**, 10, 1584–1594 (1989).

Eftimiu, C. and G. Pan, “First-order wiener-hermite expansion in the electromagnetic scattering by dielectric rough interfaces”, Radio Sci. **25**, 1, 1–8 (1990).

FEKO, URL `http:www.feko.info` (2015).

Fung, A. K., *Microwave Scattering and Emission Models and their Applications* (Artech House, Norwood, MA, 1994).

Fung, A. K., Z. Li and K. S. Chen, "Backscattering from a randomly rough dielectric surface", IEEE Trans. Geosci. Remote. Sens. **30**, 2, 356–369 (1992).

Fung, A. K. and G. Pan, "A scattering model for perfectly conducting random surfaces I. Model development", Int. J. Remote Sens. **8**, 11, 1579–1593 (1987).

Guan, N., K. Yashiro and S. Ohkawa, "Wavelet transform approach on boundary element method for solving electromagnetic scattering problems", in "Proceedings of Antennas and Propagation Society International Symposium", pp. 1834–1837 (Salt Lake City, UT, 2000).

Gurel, L. and O. Ergul, "Singularity of the magnetic-field integral equation and its extraction", IEEE Antennas Wireless Propag. Lett. **4**, 229–232 (2005).

Harrington, R. F., *Time-harmonic electromagnetic fields* (Wiley-IEEE Press, 2001).

Hesham, M. and M. Hassanein, "On the use of discrete wavelet transform for solving integral equations of acoustic scattering", Acoust. Phys. **56**, 4, 560–567 (2010).

Holliday, D., L. L. DeRaad and G. J. St-Cyr, "Forward-backward: a new method for computing low-grazing angle scattering", IEEE Trans. Antennas Propag. **44**, 5, 722–729 (1996).

Hsieh, C. Y. and A. K. Fung, "Bistatic multiple scattering from randomly rough surfaces", IEE Proc. Microw. Antennas Propag. **150**, 4, 214–218 (2003).

Huang, H., G. D. Yang and Y. Du, "Performance of preconditioned nonstationary methods for electromagnetic scattering from one dimensional dielectric rough surfaces", IEEE Trans. Antennas Propag. **62**, 10, 5362–5365 (2014).

Huang, S. W. and L. Tsang, "Electromagnetic scattering of randomly rough soil surfaces based on numerical solutions of maxwell equations in three-dimensional simulations using a hybrid UV/PBTG/SMCG method", IEEE Trans. Antennas Propag. **50**, 10, 4025–4035 (2012).

Huang, S. W., G. H. Zhang, M. Y. Xia and C. H. Chan, "Numerical analysis of scattering by dielectric random rough surfaces using modified SMCG scheme and curvilinear RWG basis functions", IEEE Trans. Antennas Propag. **57**, 10, 3392–3397 (2009).

Iodice, A., "Forward-backward method for scattering from dielectric rough surfaces", IEEE Trans. Antennas Propag. **50**, 7, 901–911 (2002).

Ishimaru, A., C. Le, Y. Kuga, L. A. Sengers and T. K. Chan, "Polarimetric scattering theory for high slope rough surfaces", Prog. Electromagn. Res. **14**, 1–36 (1996).

Jeffrey, A. and D. Zwillinger, *Table of integrals, series, and products* (Academic Press, 2007), 7th edn.

Jin, M., M. Bai, L. Zhang, G. Pan and J. Miao, "On the coiflet-tds solution for scattering by sharp coated cones and its application to emissivity determination", IEEE Trans. Geoscience and Remote Sensing **54**, 3, 1399–1409 (2016).

Kong, J. A., *Electromagnetic Wave Theory* (Wiley, 1986).

Li, S., J. O. Nyagilo, D. P. Dave and J. X. Gao, "Continuous wavelet transform based partial least squares regression for quantitative analysis of raman spectrum", IEEE Trans. Nanobiosci. **12**, 3, 214–221 (2013).

Li, Z. and A. K. Fung, "A reformulation of the surface field integral equation", Electromagnet. Wave **5**, 2, 195–203 (1991).

Liu, B., Z. Y. Li and Y. Du, "A fast numerical method for electromagnetic scattering from dielectric rough surfaces", IEEE Trans. Antennas Propag. **59**, 1, 180–188 (2011).

Mallat, S. G., "A theory of multiresolution signal decomposition: The wavelet representation", IEEE Trans. Pattern Anal. Machine Intell. **11**, 674–693 (1989).

Ogurtsov, S. and G. Pan, "An updated review of general dispersion relation for conditionally and unconditionally stable fdtd algorithms", IEEE Trans. Antennas Propag. **56**, 8, 2572–2583 (2008).

Pak, K., L. Tsang and J. Johnson, "Numerical simulations and backscattering enhancement of electromagnetic waves from two-dimensional dielectric random rough surfaces with the sparse-matrix canonical grid method", Opt. Soc. Am. **14**, 7, 1515–1529 (1997).

Pan, G., *Wavelet in Electromagnetics and Device Modeling* (Wiley, Hoboken, NJ, 2003).

Pan, G., M. Jin, L. Zhang, M. Bai and J. Miao, "An efficient scattering algorithm for smooth and sharp surfaces: coiflet based scalar MFIE", IEEE Trans. Antennas Propag. **62**, 8, 4241–4250 (2014).

Pan, G., M. Toupikov and B. Gilbert, "On the use of coifman intervallic wavelets in the method of moments for fast construction of wavelet sparsified matrices", IEEE Trans. Antennas Propag. **47**, 7, 1189–1200 (1999).

Pan, G., K. Wang and D. Cochran, "Coifman wavelets in 3-D scattering from very rough random surfaces", IEEE Trans. Antennas Propag. **52**, 11, 3096–3103 (2004).

Phu, P., A. Ishimaru and Y. Kuga, "Controlled millimeter-wave experiments and numerical simulationson the enhanced backscattering from one-dimensional very rough surfaces", Radio Sci. **28**, 4, 533–548 (1993).

Phu, P., A. Ishimaru and Y. Kuga, "Copolarized and cross-polarized enhanced backscattering from two-dimensional very rough surfaces at millimeter wave frequencies", Radio Sci. **29**, 5, 1275–1291 (1994).

Poggio, A. and E. Miller, "Integral equation solutions of three-dimensional scattering problems", in "Computer Techniques for Electromagnetics", chap. 4 (Pergamon Press, New York, 1973).

Sarkar, T. K. and K. Kim, "Solution of large dense complex matrix equations utilizing wavelet-like transforms", IEEE Trans. Antennas Propag. **47**, 10, 1628–1632 (1999).

Tang, Y. Y., Y. Lu and H. Yuan, "Hyperspectral image classification based on three-dimensional scattering wavelet transform", IEEE Trans. Geosci. Remote Sens. **53**, 5, 2467–2480 (2015).

Tong, M. S., G. C. Wan and L. Chen, "Intervallic-wavelet analysis for electromagnetic scattering by thin-wire structures", in "Proceedings of Antennas and Propagation Society International Symposium", pp. 1585–1588 (Spokane, WA, 2011).

Torrungrueng, D., H. T. Chou and J. T. Johnson, "A novel acceleration algorithm for the computation of scattering from rough surfaces with the forwardsbackward method", Radio Sci. **33**, 5, 1277–1287 (1998).

Tretiakov, Y., G. Lei, G. Pan and B. Gilbert, "Numerical study of random surface scattering using Coifman wavelets", IEE Proc. Microw. Antennas Propag. **151**, 4, 331–337 (2004).

Tsang, L. and J. A. Kong, *Scattering of Electromagnetic Waves, Vol. 3: Advanced Topics* (Wiley, 2001).

Ubeda, E. and J. M. Rius, "Mfie mom-formulation with curl-conforming basis functions and accurate kernel integration in the analysis of perfectly conducting sharp-edged objects", Microw. Opt. Technol. Lett. **44**, 4, 354–348 (2005).

Ubeda, E. and J. M. Rius, "Novel monopolar mfie mom-discretization for the scattering analysis of small objects", IEEE Trans. Antennas Propag. **54**, 1, 50–57 (2006).

Ulaby, F. T., R. K. Moore and A. K. Fung, *Microwave Remote Sensing: Active and Passive, Vol. II – Radar Remote Sensing and Surface Scattering and Emission Theory* (Addison-Wesley, Reading, MA, 1982).

Vipianaa, F., F. P. Andriullia and G. Vecchi, "Two-tier non-simplex grid hierarchic basis for general 3d meshes", Wave Random Media **19**, 1, 126–146 (2009).

Vorst, H. V. D., "Bi-CGSTAB: a fast and smoothly converging variant of Bi-CG for the solution of non-symmetric liner systems", SIAM J. Sci. Stat. Comput. **13**, 2, 631–644 (1992).

Wang, L. and G. Pan, "Coifman wavelets in 3-d scattering from a calibration target consisting of doubly periodic sharp metal cones", IEEE Trans. Antennas Propag. **61**, 9, 4665–4674 (2013).

Warnick, K. F. and W. C. Chew, “Numerical simulation methods for rough surface scattering”, Waves Random Media **11**, 1, R1–R30 (2001).

Warnick, K. F. and A. F. Peterson, “3d mfie accuracy improvement using regularization”, in “Proceedings of Antennas and Propagation Society International Symposium”, pp. 4857–4860 (Honolulu, HI, 2007).

Woo, A. C., H. T. G. Wang, M. J. Schuh and M. L. Sanders, “Em programmer’s notebook-benchmark radar targets for the validation of computational electromagnetics programs”, IEEE Antennas Propag. Mag. **35**, 1, 84–89 (93).

Yl-Oijala, P., S. P. Kiminki, K. Cools, F. P. Andriulli and S. Jrvenp, “Mixed discretization schemes for electromagnetic surface integral equations”, Int. J. Numer. Model. **25**, 525–540 (2012).

Zhao, K., M. Vouvakis and J. Lee, “The adaptive cross approximation algorithm for accelerated method of moments computations of EMC problems”, IEEE Trans. Antennas Propag. **47**, 4, 763–773 (2005).

APPENDIX A

ITERATIVE SOLUTION OF TAPERED INCIDENT POWER

Equation (4.36) can be expressed as

$$
\begin{aligned}
P_{inc} &= \frac{\pi\tau^2}{4\eta}\frac{\alpha}{e^{\beta^2/\alpha}}\int_0^1 I_0\left(2\beta\sqrt{u}\right)e^{-\alpha u}\sqrt{1-u}du \\
&= \frac{\pi\tau^2}{4\eta}\frac{\alpha}{e^{\beta^2/\alpha}}\int_0^1 duI_0\left(2\beta\sqrt{u}\right)e^{-\alpha u}\left\{1+\sum_{n=1}^{\infty}(-1)^n\frac{\frac{1}{2}\left(\frac{1}{2}-1\right)\cdots\left(\frac{1}{2}-n+1\right)}{n!}u^n\right\}
\end{aligned}
\tag{A.1}
$$

where $\beta = (k\tau)^2\sin\theta_i/2, \alpha = (k\tau)^2/2$ and $u = \rho^2$.

Expanding (A.1) into series forms (Jeffrey and Zwillinger, 2007), we can approximately get

$$
\begin{aligned}
P_{inc} &= \frac{\pi\tau^2}{4\eta}\frac{\alpha}{e^{\beta^2/\alpha}}\int_0^1 duI_0\left(2\beta\sqrt{u}\right)e^{-\alpha u}\sum_n\{C_n u^n\} \\
&= \frac{\pi\tau^2}{4\eta}\frac{\alpha}{e^{\beta^2/\alpha}}\sum_n C_n\frac{\Gamma(n+1)}{\Gamma(1)}\alpha^{-(n+1)}\sum_{m=0}^{\infty}\frac{(n+1)^{(m)}\left(\frac{\beta^2}{\alpha}\right)^m}{1^{(m)}m!} \\
&= \frac{\pi\tau^2}{4\eta}\frac{\alpha}{e^{\beta^2/\alpha}}\sum_n C_n\alpha^{-(n+1)}\sum_{m=0}^{\infty}\frac{(n+m)\cdots(m+1)\left(\frac{\beta^2}{\alpha}\right)^m}{m!} \\
&= \frac{\pi\tau^2}{4\eta}\sum_n\frac{C_n}{\alpha^n}\sum_{m=0}^{\infty}\frac{(n+m)\cdots(m+1)\left(\frac{\beta^2}{\alpha}\right)^m}{m!e^{\beta^2/\alpha}}
\end{aligned}
\tag{A.2}
$$

where

$$
C_n = \begin{cases} 1, & (n=0) \\ (-1)^n\frac{\frac{1}{2}\left(\frac{1}{2}-1\right)\cdots\left(\frac{1}{2}-n+1\right)}{n!}, & (n\geq 1) \end{cases}
\tag{A.3}
$$

For easy implementation, (A.2) can be transferred to

$$
P_{inc} = \frac{\pi\tau^2}{4\eta}\left\{\sum_n\frac{C_n}{\alpha^n}F_n\right\}
\tag{A.4}
$$

where

$$
\begin{aligned}
F_n &= \sum_{m=0}^{\infty}\frac{(n+m)\cdots(m+1)x^m}{m!} = e^x f_n \\
x &= \frac{\beta^2}{\alpha}
\end{aligned}
\tag{A.5}
$$

Then we can get several F elements in front.

$$\begin{aligned}
&F_0 = e^x \\
&F_1 = e^x(1+x) = e^x f_1 \\
&F_2 = (F_1'x)' = e^x(x^2+4x+2) = e^x f_2 \\
&F_3 = (F_2'x)' = e^x(x^3+9x^2+18x+6) = e^x f_3 \\
&\cdots
\end{aligned} \tag{A.6}$$

The iterative relationship of f is found as

$$\begin{aligned}
&f_0 = 1 \\
&f_1 = 1+x = f_0(x+1) + f_0'(2x+1) + f_0''x \\
&f_2 = x^2+4x+2 = f_1(x+1) + f_1'(2x+1) + f_1''x \\
&f_3 = x^3+9x^2+18x+6 = f_2(x+1) + f_2'(2x+1) + f_2''x \\
&\cdots \\
&f_{n+1} = f_n(x+1) + f_n'(2x+1) + f_n''x
\end{aligned} \tag{A.7}$$

Define

$$f_n = a_n x^n + a_{n-1}x^{n-1} + \cdots + a_1 x + a_0 \tag{A.8}$$

where $a_0, a_1, \cdots, a_n$ are real number coefficients.

Similarly,

$$\begin{aligned}
&f_n' = a_n \cdot n x^{n-1} + a_{n-1} \cdot (n-1)x^{n-2} + \cdots + a_1 \\
&f_n'' = a_n \cdot n(n-1)x^{n-2} + a_{n-1} \cdot (n-1)(n-2)x^{n-3} + \cdots + a_2
\end{aligned} \tag{A.9}$$

Table A.1: Incident power of the tapered wave ($\tau = 2.4\lambda$)

θ_i°	Numerical data	Iterative data	Error/%
0	0.01187180	0.01194671	0.630
30	0.01025520	0.01032108	0.642
60	0.00562885	0.00565867	0.530
80	0.00213183	0.00217099	1.837

Then,

$$
\begin{aligned}
f_{n+1} &= b_{n+1}x^{n+1} + b_n x^n + \cdots + b_1 x + b_0 \\
&= f_n(x+1) + f_n'(2x+1) + f_n'' x \\
&= x^{n+1}\left\{a_n\right\} + x^n\left\{a_n(2n+1) + a_{n-1}\right\} \\
&\quad + x^{n-1}\left\{a_n n^2 + a_{n-1}[2(n-1)+1] + a_{n-2}\right\} \\
&\quad + x^{n-2}\left\{a_{n-1}(n-1)^2 + a_{n-2}[2(n-2)+1] + a_{n-3}\right\} \\
&\quad + x^{n-3}\left\{a_{n-2}(n-2)^2 + a_{n-3}[2(n-3)+1] + a_{n-4}\right\} \\
&\quad \cdots \\
&\quad + x^m\left\{a_{m+1}(m+1)^2 + a_m[2m+1] + a_{m-1}\right\} \\
&\quad \cdots
\end{aligned}
\tag{A.10}
$$

where

$$
\begin{aligned}
&m = n+1, n, n-1, \cdots \\
&a_{m+1} = 0 \ (m+1 > n) \\
&a_{m-1} = 0 \ (m-1 < 0)
\end{aligned}
\tag{A.11}
$$

Combined (A.7) and (A.10), the coefficients of $\forall f$ can be solved iteratively. Accordingly, the incident power has been analytically reformulated into the binomial expression. Table A.1 compares the iterative solutions of the tapered incident power with numerical data collected from a 8×8 plate, under multiple incidents ($\phi_i = 90\circ$ and $\tau = 2.4\lambda$).

APPENDIX B

GENERATION OF RANDOM SURFACES BY SPECTRAL DOMAIN METHOD

In order to perform numerical simulations, a realization has to be generated in a random rough surface with prescribed surface distribution and autocorrelation functions. The spectral method for the generation of a random surface profile has been found more convenient especially for surface derivatives.

The 2-D rough surface is described by $z = f(x, y)$, which is a random function of position (x, y). Various two-dimensional spectra and autocorrelations, which are basically extensions of the one-dimensional case, can be used to generate the 2-D rough surface. For reasons of practicality in surface manufacturing, only surfaces with Gaussian roughness and Gaussian spectrum are considered. The correlation function $R(\tau_x, \tau_y)$ that describes the coherence between different points on the surface separated by the distance $d = \sqrt{\tau_x^2 + \tau_y^2}$ and is given by

$$R(\tau_x, \tau_y) = \sigma^2 exp\left(-\frac{\tau_x^2}{2l_x^2} - \frac{\tau_y^2}{2l_y^2}\right) \tag{B.1}$$

where τ_x and τ_y describe the separation between any two points along the x and y directions.

The coherence length of the surface profiles is given by l_x and l_y. The power spectral density function of the surface $W(k_x, k_y)$ is related to the correlation function via a two-dimensional Fourier transform. For a Gaussian correlation function given by (B.1) we have

$$W(k_x, k_y) = \frac{l_x l_y \sigma^2}{4\pi} exp\left(-\frac{k_x^2 l_x^2}{4} - \frac{k_y^2 l_y^2}{4}\right) \tag{B.2}$$

It is important to note that in (B.2), there are two distinct correlation lengths, l_x and l_y. The surface is isotropic when $l_x = l_y$, and anisotropic if $l_x \neq l_y$. If one of the correlation lengths is much greater than the other, the 2-D surface becomes essentially a 1-D surface for the purpose of the experiments and numerical calculations. The corresponding rms slopes are defined respectively by $\rho_x = \sqrt{2}\sigma/l_x$ and $\rho_y = \sqrt{2}\sigma/l_y$.

The rough surface profile $z = f(x, y)$ is related to the 2-D DFT of the power spectrum as

$$f(x, y) = \frac{1}{L_x L_y} \sum_{m=-\frac{N_x}{2}}^{\frac{N_x}{2}-1} \sum_{n=-\frac{N_y}{2}}^{\frac{N_y}{2}-1} F(K_{xm}, K_{yn}) exp(iK_{xm}x + iK_{yn}y) \tag{B.3}$$

where

$$F(K_{xm}, K_{yn}) = 2\pi\sqrt{L_x L_y W(K_{xm}, K_{yn})} \begin{cases} \frac{N(0,1)+iN(0,1)}{\sqrt{2}}, \; m \neq 0, \frac{N_x}{2}, \; n \neq 0, \frac{N_y}{2} \\ N(0,1), \; m = 0, \frac{N_x}{2} \; or \; n = 0, \frac{N_y}{2} \end{cases}$$

and

$$K_{xm} = \frac{2\pi m}{L_x}, \; K_{yn} = \frac{2\pi n}{L_y}, \; i = \sqrt{-1} \tag{B.4}$$

In the above expressions, K_{xm} and K_{yn} are the discrete set of spatial frequencies, L_x and L_y are surface profile lengths in x and y directions, respectively. To generate a real sequence, the requirement for $F(K_{xm}, K_{yn})$ is as follows

$$\begin{aligned} F(K_{xm}, K_{yn}) &= F^*(-K_{xm}, -K_{yn}) \\ F(K_{xm}, -K_{yn}) &= F^*(-K_{xm}, K_{yn}) \end{aligned} \tag{B.5}$$

Under the above two conditions, the 2D sequence is "conjugate symmetrical" about the origin. This means that the reflection of any point about the origin is its complex conjugate. By using the Fourier coefficients (B.4) we can also find the corresponding Fourier coefficients for the surface derivatives in the x and y directions

$$\begin{aligned} F_{\partial x}(K_{xm}, K_{ny}) &:= F(K_{xm}, K_{ny}) \times iK_{xm} \\ F_{\partial y}(K_{xm}, K_{ny}) &:= F(K_{xm}, K_{ny}) \times iK_{yn} \end{aligned} \tag{B.6}$$

By taking the inverse 2-D DFT with the Fourier coefficients given in (B.6) we can also obtain at each sampling point the first derivatives of a random surface profile in both the x and y directions. Fig. 4.1 is generated from the 2-D spectral method discussed above.